Title
New Twin Screw Compressor Design by Deviation Function Method

Author
Huang, Chih-Yung

Publication Date
2015

Peer reviewed|Thesis/dissertation

UNIVERSITY OF CALIFORNIA

Los Angeles

New Twin Screw Compressor Design by Deviation Function Method

A dissertation submitted in partial satisfaction of the
requirement for the degree of Doctor of Philosophy
in Mechanical Engineering

by

Chih-Yung Huang

2015

ABSTRACT OF THE DISSERTATION

New Twin Screw Compressor Designs by Deviation Function Method

by

Chih-Yung Huang

Doctor of Philosophy in Mechanical Engineering

University of California, Los Angeles, 2015

Professor Daniel C. Yang, Chair

The rotor profiles of twin screw compressors have a significant influence on the compressor performance. Three different rotor profile design methods are derived mathematically and their limitations are addressed. This dissertation presents the complete theory and algorithm of the deviation function (DF) method for the twin screw compressor design. This method is based on conjugate pair design and generates new twin screw compressor profiles from generating curves derived by the deviation functions. The deviation functions used in this research are composed of the Bezier curves. The partially overlapped three-segment third-order Bezier curve-based deviation function is proposed to achieve the goal of minimizing the blowhole area along with shorter interlobe sealing line length. The complication of combining curves as the generating

curves and determining values of parameters of those curves are problems for the rotor profile designs of twin screw compressors in industry. Thanks to the adoption of Bezier curves for the deviation functions, these problems can be avoided when the rotor profiles of twin screw compressors are designed in this study. In addition, it helps discover a more diverse range of designs and thus leads to the more universal optimal results. Those advantages are emphasized by showing a variety of design examples and the improvement for the industry applications. Moreover, the effects of the lead non-uniformity of the twin screw compressor are investigated and the results are compared to the twin screw compressor with constant lead in this research. It is found that the twin screw compressor with increasing lead tends to reduce the leakage, and thus, the volumetric efficiency of this kind is improved, especially in the practical operating conditions when the working gas has a significant tendency to leak out of the compression chamber of the compressor.

This dissertation of Chih-Yung Huang is approved.

Stanley B. Dong

Nasr M. Ghoniem

Tsu-Chin Tsao

Daniel C. Yang, Committee Chair

University of California, Los Angeles

2015

To my beloved parents and family

Contents

Abstract of the dissertation ..... **ii**

List of Figures ..... **ix**

List of Tables ..... **xiv**

Acknowledgements ..... **xvi**

Vita…… ..... **xvii**

Chapter 1 Introduction **1**

1.1 Outline and Operation Cycle 3

1.2 Literature Survey 6

1.3 Motivations and Objectives 12

1.4 Organization of the Dissertation 13

Chapter 2 Geometry Analysis of the Twin Screw Compressor **15**

2.1 Geometric Parameters of the Twin Screw Rotor 15

2.2 Conventional Methods for Rotor Profile Generation 17

2.2.1 Generating-Profile method 20

2.2.2 Rack-Profile method 24

2.2.3 Contact-Path method 28

2.3 Three-Dimensional Rotor Surface 32

2.4 Interlobe Sealing Curve 34
2.5 Chamber Volume 36
2.6 Blowhole 37
2.7 Conclusions 41

Chapter 3 Development of Bezier Curve-Based Deviation-Function Method for Twin Screw Compressor Design 43

3.1 Introduction 43
3.2 Deviation Function Method 44
3.3 Bezier Curve 47
3.4 Screw Compressor Cross-Sectional Profile Design via Bezier Curve-Based Deviation Functions 49
3.5 Design Examples 55

Chapter 4 New Bezier Curve-Based Screw Compressor Profiles with Minimized Blowholes 65

4.1 Introduction 66
4.2 Designs by Using One-Segment Third-Order Bezier Curve-Based Deviation Functions 67
4.3 Designs by Using Two-Segment Third-Order Bezier Curve-Based Deviation Functions 71
4.4 Designs by Using Partially Overlapped Three-Segment Third-Order Bezier Curve-Based Deviation Functions 76
4.4.1 Partially overlapped three-segment deviation function 76
4.4.2 Optimization for Existing Profiles 82

4.5 Conclusions 90

Chapter 5 Twin Screw Compressor with Non-Constant Lead 94

5.1 Variation of Lead 96

5.2 Effects of Non-Constant Lead on Variation of Chamber Volume and Pressure Rise 97

5.3 Leakage Reduction of Twin Screw Compressors with Non-Constant Lead 98

5.3.1 Leakage Model 99

5.3.2 Interlobe sealing line and blowhole area as the lead is varying 100

5.3.3 Effects on leakage reduction as the lead is non-constant 102

5.4 Results for Volumetric Efficiency of Screw Compressors with Non-Constant Lead 103

5.5 Conclusions 114

Chapter 6 Conclusions and Future Work 116

6.1 Conclusions 116

6.2 Future Work 117

Bibliography 119

List of Figures

Figure 1.1: A twin screw compressor. 1

Figure 1.2: Two types of compressors with the same size rotors. 2

Figure 1.3: Volumetric changes inside the working chamber. 4

Figure 1.4: Side view of the male rotor. 5

Figure 2.1: A pair of spur gears and their pitch circles. 19

Figure 2.2: Pitch circles and coordinate systems. 21

Figure 2.3: Coordinate system for Rack-Profile method to generate male rotor. 24

Figure 2.4: Coordinate system for Rack-Profile method to generate female rotor. 27

Figure 2.5: Coordinate system for Contact-Path method. 29

Figure 2.6: Coordinate systems to generate rotor surfaces. 32

Figure 2.7: Projections of the Interlobe sealing line (a) on a rotor (b) on *xy*-plane. 35

Figure 2.8: Blowhole 38

Figure 2.9: End view of the blowhole 39

Figure 2.10: Calculation of the blowhole area. 39

Figure 3.1: Pitch curves and generated conjugate pairs. 45

Figure 3.2: A generated profile. 47

Figure 3.3: Pitch circles and coordinate systems. 50

Figure 3.4: Designed rotor profiles of screw compressor with 2/3 configuration. 57

Figure 3.5: Designed rotor profiles of screw compressor with 3/4 configuration. 59

Figure 3.6: Designed rotor profiles of screw compressor with 4/6 configuration. 61

Figure 3.7: Designed rotor profiles of screw compressor with 5/6 configuration. 63

Figure 4.1: Parameters for determining the control points of the one-segment 3rd order Bezier curve-based deviation function 67

Figure 4.2: Design examples by using the one-segment third-order Bezier curve-based deviation functions. 70

Figure 4.3: Parameters for determining the control points of the two-segment third-order Bezier curve-based deviation function. 71

Figure 4.4: Design examples by using the two-segment third-order Bezier curve-based deviation functions with different θ_M 73

Figure 4.5: A design result with shorter heigth of blowhole by using the two-segment third-order Bezier curve-based deviation function. 74

Figure 4.6: A design example with higher conformity. 74

Figure 4.7: Bound of the line of action. 75

Figure 4.8: Parameters for determining the control points of the partially overlapped three-segment third-order Bezier curve-based deviation function. 77

Figure 4.9: A design example with a 5/6 configuration by using a partially overlapped three-segment third-order Bezier curve-based deviation function. 78

Figure 4.10: Break through the boundary. 78

Figure 4.11: Hitachi profile. 79

Figure 4.12: GHH profile. 80

Figure 4.13: Fu Sheng profile. 81

Figure 4.14: Minimized blowhole area for Hitachi profile. 84
Figure 4.15: Minimized blowhole area for GHH profile 85
Figure 4.16: Minimized blowhole area for Fu Sheng profile. 86
Figure 4.17: Minimized blowhole area ($\Delta l_s \leq 10\%$) for Hitachi profile. 87
Figure 4.18: Minimized blowhole area ($\Delta l_s \leq 3\%$) for GHH profile 88
Figure 4.19: Minimized blowhole area ($\Delta l_s \leq 1\%$) for Fu Sheng profile 89
Figure 4.20: Minimized blowhole area ($\Delta l_s \leq -1\%$) for Hitachi profile. 91
Figure 4.21: Minimized blowhole area ($\Delta l_s \leq -1\%$) for GHH profile. 92
Figure 4.22: Minimized blowhole area ($\Delta l_s \leq -1\%$) for Fu Sheng profile 93
Figure 5.1: Rotors of twin screw compressors with non-constant lead. 95
Figure 5.2: Relationship between axial translation and twist angle for rotors with different types of leads. 95
Figure 5.3: Volumetric displacement and pressure rise during compression process. .. 97
Figure 5.4: Leakage flowrate. 100
Figure 5.5: Evolution of interlobe sealing line length and blowhole area. 101
Figure 5.6: Variation of leakage flowrate through the interlobe sealing and blowhole. 103
Figure 5.7 Variants of lead curve 104
Figure 5.8: Influence of pressure ratio and rotational speed on volumetric efficiency at fixed interlobe clearance with air for the compressor with constant lead. 106
Figure 5.9: Influence of pressure ratio and rotational speed on volumetric efficiency at fixed interlobe clearance with nitrogen for the compressor with constant lead. 106

Figure 5.10: Influence of pressure ratio and rotational speed on volumetric efficiency at fixed interlobe clearance with helium for the compressor with constant lead. 107
Figure 5.11: Variation of volumetric efficiency with pressure ratio at fixed interlobe clearance and at fixed rotational speed of male rotor with different gases for the compressor with constant lead. 107
Figure 5.12: Variation of volumetric efficiency with different working gases at different rotational speed at a fixed interlobe clearance for for the compressor with constant lead. 108
Figure 5.13: Variation of volumetric efficiency with pressure ratio at the same rotational speed at different interlobe clearance with air for compressors with different leads. 109
Figure 5.14: Variation of volumetric efficiency with pressure ratio at the same interlobe clearance at different rotational speed with air for compressors with different leads. 110
Figure 5.15: Variation of volumetric efficiency with pressure ratio at the same rotational speed at different interlobe clearance with nitrogen for compressors with different leads. 111
Figure 5.16: Variation of volumetric efficiency with pressure ratio at the same interlobe clearance at different rotational speed with nitrogen for compressors with different leads. 112

Figure 5.17: Variation of volumetric efficiency with pressure ratio at the same rotational speed at different interlobe clearance with helium for compressors with different leads. 113
Figure 5.18: Variation of volumetric efficiency with pressure ratio at the same interlobe clearance at different rotational speed with helium for compressors with different leads. 114

List of Tables

Table 3.1: Control points for Figure 3.4 56

Table 3.2: Control points for Figure 3.5 56

Table 3.3: Control points for Figure 3.6 56

Table 3.4: Control points for Figure 3.7 56

Table 4.1: Parameters for Figure 4.2 69

Table 4.2: Parameters for Figure 4.4 72

Table 4.3: Parameters for Figure 4.5 and Figure 4.6 74

Table 4.4: Parameters for Figure 4.9 78

Table 4.5: Combination of curves of Hitachi profile 79

Table 4.6: Combination of curves of GHH profile. 80

Table 4.7: Combination of curves of Fu Sheng profile 81

Table 4.8: Parameters for DFM-H1 84

Table 4.9: Results for Figure 4.14 84

Table 4.10: Parameters for DFM-G1 85

Table 4.11: Results for Figure 4.15 85

Table 4.12: Parameters for DFM-F1 86

Table 4.13: Results for Figure 4.16 86

Table 4.14: Parameters for DFM-H2 87

Table 4.15: Results for Figure 4.17 87

Table 4.16: Parameters for DFM-G2 88

Table 4.17: Results for Figure 4.18 88

Table 4.18: Parameters for DFM-F2..... 89

Table 4.19: Results for Figure 4.19 89

Table 4.20: Parameters for DFM-H3 91

Table 4.21: Results for Figure 4.20 91

Table 4.22: Parameters for DFM-G3 92

Table 4.23: Results for Figure 4.21 92

Table 4.24: Parameters for DFM-F3..... 93

Table 4.25: Results for Figure 4.22 93

Table 5.1: Formulation of different screw parameter functions for non-constant lead..... 104

ACKNOWLEDGEMENTS

First of all, I would like to express my deepest gratitude to my parents and family for their profound love, endless support, earnest encouragement, and selfless sacrifices. My parents have been giving me all their best since I was born. Thank my wife for always being with me and thank my son for bringing me so much joy to my life. This dissertation would not have been completed without their love and support.

I am grateful to my academic advisor, Professor Daniel C. H. Yang. Thank him for the invaluable guidance, support, and patience. Without his help, I could not have been here and accomplished the degree.

I am thankful to the other committee members of my doctoral committee, Professor Stanley B. Dong, Professor Nasr M. Ghoniem, and Professor Tsu-Chin Tsao, for their instructive comments and suggestions on this dissertation.

Finally, special thanks to my lab mates, Seung Ryong Han and Sarah Warren Rose for their kind assistance, empathy, and perspective. I will miss the old time when we were in CAD Lab.

VITA

2004	B.S. in Mechanical Engineering National Cheng Kung University, Tainan City, TAIWAN
2006	M.S. in Mechanical Engineering National Cheng Kung University, Tainan City, TAIWAN
2008 - 2009	Teaching Assistant National Cheng Kung University, Tainan City, TAIWAN
2009 - 2010	UCLA Fellowship University of California, Los Angeles, CA
2010 - 2013	Teaching Assistant/Associate/Fellow University of California, Los Angeles, CA
2013 - 2014	CAD Lab Manager University of California, Los Angeles, CA

Chapter 1

Introduction

The twin screw compressor, as shown in Figure 1.1, is a rotary positive displacement compressor[1] and is one of the most commonly used gas compressor. Besides gases, this type of compressor is capable of compressing vapors and refrigerants. Twin screw compressors supply the compressed gas in a variety of industries, such as building and architecture, food, chemical process, pharmaceutical, and metallurgical industries. They are also used for refrigeration, air conditioning applications, and vehicle superchargers. Twin screw compressors currently comprise a major percentage of the positive displacement compressor market. The main reasons for success are high rotational speed, compactness, ability to maintain high efficiency over a wide range of operating conditions, long service life, and excellent reliability.

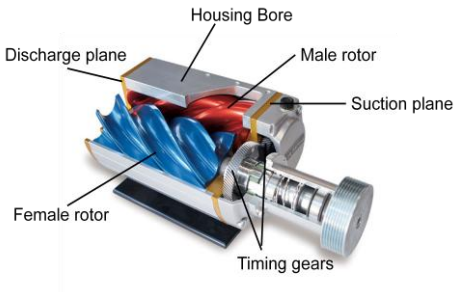

Figure 1.1: A twin screw compressor.

[1] A positive displacement compressor transmits gas from the low pressure reservoir to the high pressure reservoir by enclosing the gas in a chamber and then positively reducing the gas volume. The volume reduction leads to the rise of gas pressure.

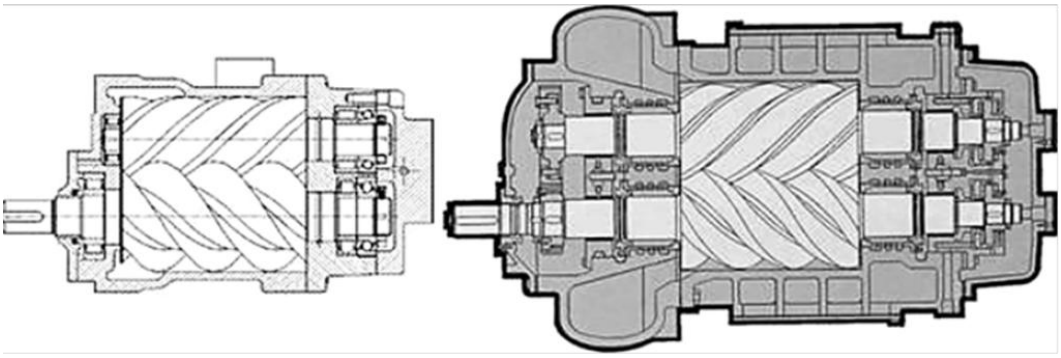

Figure 1.2: Two types of compressors with the same size rotors.

Twin screw compressors can be divided into two categories: oil-injected compressors and oil-free compressors. Two types of compressors with the same size rotors are shown in Figure 1.2 [1]. In the former design, a significant amount of oil is mixed with the working fluid and injected into the chambers for lubrication, sealing, and temperature reduction during operation. The oil lubricant helps absorb the heat during compression and makes the direct contact between rotors possible. It also protects the parts from corrosion of gases. Absorbing the heat enables increasing the pressure ratio in a single stage. The male rotor is able to drive the female rotor with the oil lubricant film at the intermeshing between rotors, and thus the timing gears are not required for the oil injected machines. Because of the lack of internal sealing devices, this design is not as mechanically sophisticated, is less expensive to manufacture, and it has higher efficiency. If a compatible lubricant is available, oil-injected compressors can satisfy the requirements for a variety of volume flows and the high pressure ratio for different gases. As a result, it can be used in industry as a source of compressed air and refrigeration. On the other hand, for the oil-free compressors, the working fluid is not blended with oil and therefore direct contact between the rotors and the rotor and housing is prevented

by timing gears driving the rotors. These meshing gears are positioned outside the chamber and lubricated externally. Because the external lubricant must be isolated outside of the chamber, sealing is needed on the shaft between the chambers and bearings. This sealing problem continues to be under the scrutiny of process gas compressor manufacturers. The internal sealing problem is the reason why the oil-free machines are more expensive to fabricate than the oil-injected. In contrast to oil-injected machines, oil-free compressors are applied to systems where the volume flow is constant and the pressure ratio of the working fluid is low. Therefore, when oil contamination is undesirable, the oil-free compressor is the suitable choice.

Compared to other types of positive displacement compressors, the twin screw compressors have fewer moving parts, no reciprocating mass, no eccentrically revolving parts, no intake/outlet valves, and no clearance volume. It also has the advantages of providing high pressure ratios and tolerance to working fluid carryover. On the other hand, the disadvantages are the fixed built-in volume ratio and inevitable internal leakage.

1.1 Outline and Operation Cycle

The so-called twin screw compressor has two helical rotors rotating on two parallel axes separated by a certain distance. The two conjugate rotors are male and female rotors which mesh with each other. They provide not only the function as a gas compression mechanism but also as a gear pair under the appropriate lubrication conditions. The rotors are placed in a cylindrical housing bore and bound laterally at two ends by the suction and discharge planes. There are adequate suction and discharge ports on the suc-

tion and discharge planes, respectively. The rotors are similar to helical gears. The teeth of the male rotor are referred to as lobes and those of the female rotor are flutes. As the rotors are situated in such order, i.e. male to the left and female to the right, and viewed from the discharge end in Figure 1.3 where one single helical chamber highlighted, the male rotor rotates clockwise while the female turns or is driven in the counter-clockwise direction. While the rotors rotate accordingly, the helical chambers evolve gradually and provide the mechanism for gas accommodation, transmission, and compression. There are two helical sections, each belonging to a respective rotor, in each chamber. The chamber is surrounded by the helical surfaces of the rotors, the housing surface, and the suction and/or discharge plane and bounded by the tips of lobes and flutes and the interlobe sealing curve. The volume of the compression cavity increases gradually from zero to the maximum value during suction process and then decreases to zero during compression and discharge processes.

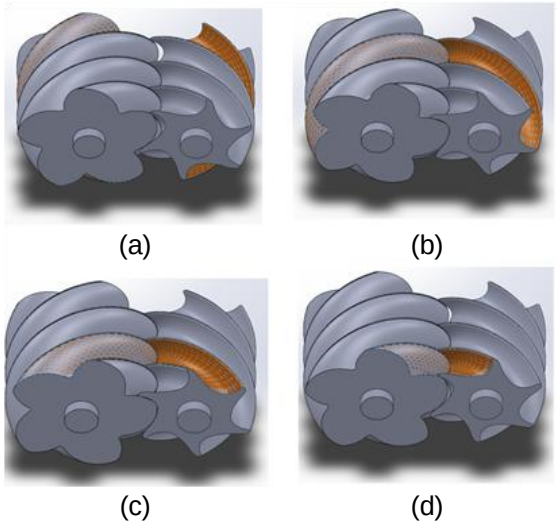

Figure 1.3: Volumetric changes inside the working chamber.

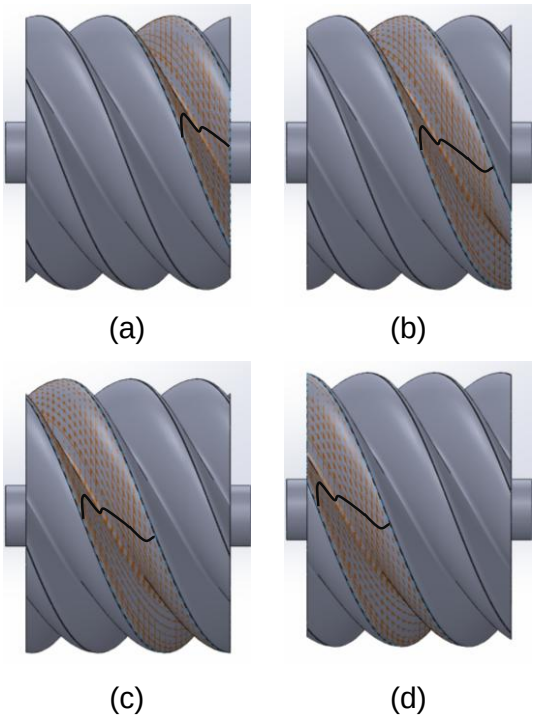

Figure 1.4: Side view of the male rotor.

The operation cycle, which comprises suction, compression, and discharge sequentially, repeats periodically. Intuitively it can be seen that there are multiple chambers existing inside the entire screw compressor. In Figure 1.4, the female rotor is hidden and the male rotor is viewed from the side. One chamber is emphasized at a time for clarity. During the suction process, the rotors' teeth starting meshing to form the interlobe sealing curve, and the chamber begins to form at the bottom of the rotor. The volume of the chamber grows as the interlobe sealing curve evolves and propagates from the suction plane along the longitudinal axis toward the discharge plane. During the suction process, the chamber keeps connecting to the low pressure vessel through the suction porting and thus at a low pressure. Suction is completed as the end of the interlobe sealing curve reaches the discharge plane. The gas chamber at this moment is the length of the

rotor. As the suction is in progress, the compression process occurs simultaneously at the top of the rotor. Since the interlobe sealing curve translates from the suction end to the discharge end, the volume of the gas chamber decreases, and thus, the gas is compressed. After a certain amount of time, the chamber is exposed to the discharge porting and then the condensed gas is discharged. Subsequently, the cycle restarts.

The rotor geometry of the twin screw compressor is completely defined by the two dimensional profile, which is the cross-section outline perpendicular to the rotor's longitudinal axis, the number of rotor teeth, the length of the screw, and the wrap angle. The profile has great influence on the operation performance of the machine since it determines the shape of the interlobe sealing curve, internal leakage paths, flow rate, torque transmission, and so forth. Among those parameters required to describe the geometry of the rotor, the rotor's cross-section profile plays a significant role in the design of an efficient twin screw compressor. The early efforts by engineers were focused on manufacturing and production technology without investigating how to improve the profiles. Designers and researchers have not begun to analytically study the basic profiles and refine the design of twin screw compressors until recent two decades.

1.2 Literature Survey

The idea of screw compressors began more than a century ago. In 1878, Heinrich Grigar [2] patented the first twin screw compressor in Germany. But the manufacturing techniques at that time were not precise enough, so this type of compressor was not prevalent and its development was limited until the 1930s. Then a Swedish engineer, Professor Alf Lysholm [3], modified Grigar's rotor profiles and described the machining

method specifically in the patent. His original design is an oil-free compressor and is driven by a pair of timing gears. Although Lysholm's company, Svenska Rotor Maskiner AB (SRM), owned the patent, they did not manufacture the compressor. Instead, they licensed the usage of this technology to manufacturers. Initially, the competition was between licensees to produce appropriate compressors for suitable markets and to be up-to-date as soon as new designs were revealed. Developing analytical models for screw compressors and improving the basic designs had not drawn much attention until recently.

The introduction of the slide valve and oil injection broadened the application range of the screw compressors in the 1950s. The slide valve changes the geometry of the radial porting area and redirects part of the condensed gas back to the suction end. With this technology, the pressure ratio was no longer fixed and became variable. At the same time, the oil-injected compressors helped increase the volumetric efficiency by diminishing the leakage because of the oil sealing feature. The injected oil is a lubricant between the teeth of rotors and also a source for cooling compressed gas; as a result, the timing gears are unnecessary and the discharge temperature decreases. The oil-injected compressors are unlike the oil-free compressors which need to be enclosed by pressure container to control the leakage [4]. Hence, the overall size of the oil-injected compressors is smaller. Howden [5] tested the first oil-injected compressor in 1955, and the oil-injected compressor was first used by Atlas Copco [3].

Although the idea of the twin screw compressor is simple and has been known for a long time, the screw compressor was not popular until about thirty years ago. Two of the main reasons are that the efficiency of a screw compressor was worse than that of other

kinds of compressors, and manufacturing the screw compressor was costlier and more difficult. Since the issues have been studied for decades, breakthroughs have been made by dedicated engineers. As far as the efficiency is concerned, asymmetric rotor profiles was adopted in 1969. Asymmetric profiles help reduce the major internal leakage through a critical area, called the leakage triangle or blow-hole area, as compared to the symmetric profile machines, and thus, the efficiency was improved. A majority of modern screw compressors utilize the asymmetric profiles. In terms of manufacturing, the invention and utilization of high precision carbide cutting tools and machining centers facilitate the production of rotors with higher tolerance and higher accuracy [3]. Fabricating complex surfaces like the screw compressor is no longer as costly and difficult as it once was.

Screw compressors have replaced the reciprocating piston compressors and other rotary type compressors in the industries. The advantages of the screw compressors over other competing compressors are as follows [2, 3, 5 - 8]:

1. Under a given volumetric flow rate, the screw compressor can operate at the higher speed with a more compact design.
2. Since the screw compressor rotates without unbalancing masses, it produces small vibrations and is very quiet. This also facilitates high speed operation.
3. It has fewer moving parts and hence, it is more reliable and needs less maintenance.
4. The screw compressor with a slide valve is more efficient and reduces power in most cases.
5. They can be made into small-sized, light-weight, portable compressors

6. The clearance between meshing teeth of the rotors make them tolerant of impact and suitable for transporting multiple-phased fluid mixtures.

These advantages lead to the usage of the screw compressors in a variety of industry applications. Klein [9] described the application of the screw compressor for heat pumps. The potential of the screw compressors in the automobile industry were discussed by Fukazawa and Ozawa [10]. Price [11] emphasized the advantages of the screw compressors in the gas and chemical processing industries. The theoretical analysis and experiments were performed by Lundberg [12] to compare efficiency of the twin screw compressor with that of the star type rotary compressor and concluded that the twin screw compressor was more effective.

The rotor geometry is a significant aspect of the design and performance of a screw compressor. It can be completely defined by specifying the cross-section profiles, numbers of teeth, rotor length, and wrap angle. Among those geometric parameters, the shape of the cross-section profile is the most significant but difficult to synthesize. It has direct relevance to the interlobe sealing curve, the blow hole area and the leakage paths. The overall efficiency is directly affected by those geometric parameters. Tang, Sjoholm, and Singh [13 - 15] investigated the influence of compressor geometric properties on the performance. Vinogradov [16] presented the ranges for values of parameter, such as outer radii, number of lobes, helix angle and rotor length, which are applicable to compressor design. A comprehensive computer aided approach was proposed by Singh and Onuschak [17]. By using this approach, the rough generating profile was able to be refined and the conjugate profile was created. In addition, computer programs are used to evaluate the leakage path, sealing curve length, blow hole area, and etc. Singh

and Patel [18] developed the computer code to analyze the performance of the screw compressor. In addition, Zhang and Hamilton [19, 20] studied the effects of rotor geometry, such as compression volume curve, sealing line length, flute area, wrap angle, and leakage triangular area. Tang and Fleming [13] studied how the blowhole area and contact line length affect the performance and then proposed methods for geometrical parameter optimization. Singh and Bowman [21] revealed that the sealing line length between rotors increases with the number of lobes and shared that the larger sealing line is detrimental to the performance at low male rotor speed and high pressure ratio.

Simulation models of the screw compressors have been developed to predict the performance and assure the quality of the compressors. Given the rotor geometry, this can be done without manufacturing the physical machines. Basic techniques for modeling and simulating the positive displacement compressors were provided by Soedel [22] and Hamilton [23]. A method to predict the performance of the oil-free type screw compressor was presented by Fujiwara et al. [24, 25]. The authors developed a computer program and obtained results for an air compressor with circular symmetric profiles. Firnhaber and Szarkowicz [26] simulated the compression process of the screw compressors by assuming the process is polytropic and the model did not have internal leakage paths to individual chambers and coolant injection. Brablik [27] presented an analytical model for the oil free compressor which was applied to an SRM compressor for investigating the pressure and temperature, flow rates, and efficiency. Sangfors [28, 29] developed a model for both oil-free and oil-injected screw compressors and compared the results of simulation with the experimental data from SRM.

Referring to the rotor profile generation methodologies, there are basically three categories: the Generating-Profile (GP) method [30, 31], the Rack-Profile (RP) method [32 - 34], and the Contact-Path (CP) method [35, 36]. All of these methods are based on the fundamental theory of gearing and theory of conjugate kinematic pairs. The GP method is to select a curve as the primary profile, which is used to generate the corresponding secondary profile. The drawbacks of this method are that it's difficult to choose the primary profile and the generated secondary profile is unpredictable. The concept of the RP method is to choose a rack profile to create a pair of conjugate profiles. It can be applied to design new profiles as well as to modify and improve the existing profiles. For the CP method, a contact path is depicted based on a pair of pitch curves, and then a pair of rotor profiles is generated by applying the kinematic relationship between the paired pitch curves. All three methods have a common disadvantage which is a lack of intuitiveness in the design. To address this, Yang et al. [37] developed a new method, called the Deviation-Function (DF) method, for conjugate pair generation. It uses the so-called deviation function which takes the form of a family of circles to reshape the pitch curves. This method makes the design of conjugate pairs more intuitive, and the incorporation of mechanical and/or geometrical properties into generated curves becomes possible. With these attributes, the desired result can be incorporated in the very beginning of design process. Currently, this method can be applied to generate symmetric, identical rotor profiles from circular or non-circular pitch curves.

With the variety of applications, the issue of screw compressor optimization is increasingly important. Researchers and engineers have been working on designing and manufacturing tailor-made screw compressors for specific operation conditions. Xing et

al. [38] designed an innovative screw compressor for refrigeration purposes. Its rotor profiles and geometric parameter optimization are achieved by using a software package named SCCAD. Stosic et al. [39 - 42] designed a series of oil-flooded twin screw air compressors with high efficiency by utilizing the RP method. The thermal efficiency calculation and geometry simulation and modeling were done as well.

The compression process of the twin screw compressor is modeled by applying the continuity equation, momentum equation, and energy equation. Sauls [43] proposed a thermodynamic modeling system for refrigeration compressors and suggested the combination of analytical and experimental methods. Ignatiev [44] studied the interaction between the gas under compression and the rotors. The geometric and physical properties, the working process, thermodynamic properties of the fluid, and thermal distortion of the rotors are considered in his modeling system. Stosic et al. [45 - 47] investigated the numerical model of thermodynamic and fluid flow processes which can be used for compressors and expanders. They considered the fluid leakage, oil injection, heat transfer, and real fluid properties in the control volume.

1.3 Motivations and Objectives

This research is motivated mainly by the necessity to design rotor profiles of screw compressors for better performance. Upon investigating the current design methods, it was found that each method has unique limitations and disadvantages. An innovative design methodology should be developed to overcome these problems and broaden the applications and possibilities for designing screw compressor rotor profiles as well as the ability to synthesize the profile intuitively. To this end, the theory of the deviation-

function method is adopted; however, in order to generate asymmetric, non-identical rotor profiles for modern screw compressors, modifications and extensions have to be made. In terms of increasing the design variety, Bezier curves are used to create the deviation functions instead of the curve functions described in the literature. In addition, since all of the existing screw compressors in the industries have constant lead, the three dimensional surface properties between the screw compressors are quite similar. To obtain the rotors of the twin screw compressors with distinctly different surface properties, the idea of changing the uniformity of screw lead is adopted and the performance of this type of twin screw compressors has to be evaluated.

1.4 Organization of the Dissertation

The contents of this dissertation have been organized into six chapters as follows:

The general introduction of the twin screw compressor is given and the review of the relevant literature is presented in Chapter 1 (this chapter).

Chapter 2 deals with the related dimension and geometry parameters of the screw compressor and the mathematical models of three different methods to generate rotor profiles for the twin screw compressors. Then, the helical rotor surface of the screw compressor is generated by simultaneously turning the cross-section profile about the rotor axis and moving the profile along the same rotor axis.

In Chapter 3, the deviation-function method to generate conjugate profiles with identical and symmetric shape is illustrated. In order to obtain conjugate shapes for the modern screw compressors, the deviation-function method is modified to generate non-identical and asymmetric profiles. The Bezier curves are adopted and help create suitable devia-

tion functions for the screw compressors. Examples are shown to reveal the design capability of this approach.

The optimal design results from the deviation-function method are compared to the existing industrial designs in Chapter 4. The optimization is performed by mainly considering the size of internal leakage paths, the blowhole area and interlobe sealing line length.

Chapter 5 introduces an alternative approach to modifying the three dimensional surface characteristics of the helical rotors. By making the screw lead a non-constant value, the effects on the screw compressor performance are discussed.

Concluding remarks and significant contributions are summarized in Chapter 6 and recommendations for further research are outlined as well.

Chapter 2

Geometry Analysis of the Twin Screw Compressor

The twin screw compressor geometry parameters and characteristics are a part of the input data to the simulation model. The geometry of the twin screw compressors is more complicated than that of most other types of compressors. A separate geometry analysis procedure is always necessary to acquire the input data to the simulation model. In this chapter, the essential geometry parameters are outlined first and then the principles of three conventional methods of rotor profile generation are explained in detail. The major geometrical properties, such as the compressor cavity volume, interlobe sealing line, and the blowhole area, are also derived since they are needed for simulation model input data. These parameters and properties are expressed as functions of rotation angle of the male rotor for the purpose of convenience.

2.1 Geometric Parameters of the Twin Screw Rotor

Prior to the design of the rotor profiles, several essential parameters should be specified in order to decide the size of twin screw compressor. The size of a single rotor, male or female, is defined by its outer diameter, wrap angle, and rotor length. The size of a pair

of twin screw rotors is determined by the center distance between rotor axes and numbers of lobes of each rotor, as well as those geometric parameters used to define the size of a single rotor. Considering the gearing relationship for constant speed ratio, the complete set of geometric parameters needed to describe the size of a twin screw compressor includes the center-to-center distance between axes of rotors, D_{cc}, outer radii of male and female rotors, r_{o1} and r_{o2}, numbers of teeth of male and female rotors, N_1 and N_2, wrap angle of the male rotor, τ_{w1}, and the rotor length, L_w. With those predefined parameters, some dimensions can be evaluated as follows:

$$r_{p1} = \left(\frac{N_1}{N_1 + N_2} \right) D_{cc} \tag{2.1}$$

$$r_{p2} = 1 - r_{p1} = \left(\frac{N_2}{N_1 + N_2} \right) D_{cc} \tag{2.2}$$

$$a_1 = r_{o1} - r_{p1} \tag{2.3}$$

$$a_2 = r_{o2} - r_{p2} \tag{2.4}$$

$$\lambda = \tan^{-1}\left(\frac{L_{d1}}{2\pi r_{p1}}\right) = \tan^{-1}\left(\frac{L_w}{\tau_{w1} r_{p1}}\right) \tag{2.5}$$

$$\beta = \frac{\pi}{2} - \lambda \tag{2.6}$$

where r_{p1} and r_{p2} are the pitch circle radii of the male and female rotors, a_1 and a_2 are the addendums of the male and female rotors, L_{d1} is the lead of the male rotor, and λ

and β are the lead angle and helix angle of the rotor respectively. Some remaining parameters of the female rotor are defined based on the constant speed ratio, m_{12}, between the male and female rotors, as follows

$$m_{12} = \left|\frac{\omega_1}{\omega_2}\right| = \left|\frac{\phi_1'}{\phi_2'}\right| = \frac{N_2}{N_1} \tag{2.7}$$

where ω_1 and ω_2 are the angular velocities of the male and female rotors. Then

$$L_{d2} = m_{12} L_{d1} \tag{2.8}$$

$$\tau_{w2} = \frac{\tau_{21}}{m_{12}} \tag{2.9}$$

$$p_1 = \frac{L_{d1}}{2\pi} = \frac{L_w}{\tau_{w1}} = r_{p1}\tan(\lambda) = \frac{r_{p2}}{m_{12}}\tan(\lambda) = \frac{p_2}{m_{12}} \tag{2.10}$$

where L_{d2} is the lead of the female rotor, τ_{w2} is the wrap angle of the female rotor, and p_1 and p_2 are the screw parameters of the male rotor and female rotor. The screw parameter describes the translated distance as the screw rotor rotates by a unit angle.

2.2 Conventional Methods for Rotor Profile Generation

The design of rotor profiles of screw compressors is based on generation of conjugate pairs. After the rotor profiles are generated, the helical surfaces of the rotors are formed

with a set of specific geometric parameters of the rotors. A pair of conjugate curves has their common contact normal at all contact points passing through a point on the line of this pair's fixed centers of rotation. The relative motion between the conjugate pair is rolling with slipping. The motion of the two bodies in which the conjugate pair is embedded is predefined by its paired pitch curves. Actually this pair of pitch curves is a special case of a conjugate pair whose contact points are always on the line between their fixed centers of rotation. As a result, the pitch curves are centrodes, meaning the loci of the contact points on the respective curves. The relative motion of the contact point between the pitch curves is pure rolling without slipping. Take the paired spur gears, shown in Figure 2.1, as an example. Their pitches curves are paired circles. The two circles roll on each other without slipping and maintain a constant rotational speed ratio. The tooth profiles, which are the conjugate curves attached to the bodies of the circles, have their common normal at the contact points passing through the point where the pitch circles are in contact. This way it is guaranteed that relative motion at the contact points between the contact teeth is perpendicular to the common normal. Thus, the slipping occurs. The spur gears have the same speed ratio as that of their pitches. Another example of variant speed ratio can be shown by noncircular gears with noncircular pitch curves [48].

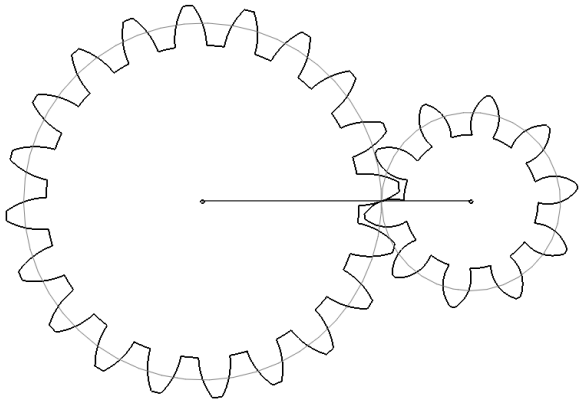

Figure 2.1: A pair of spur gears and their pitch circles.

The mathematical models of three different rotor profile generation methods are discussed in this chapter. The prevailing method of generating the screw compressor rotor profile is by applying a primary curve on one of the two rotors, and then using the motion of conjugates to generate the corresponding curve on the other rotor. As mentioned in the literature review, the three conventional approaches to generation of conjugate pairs on parallel axes are referred to as the Generating-Profile (GP) method [30, 31], the Rack-Profile (RP) method [32 - 34], and the Contact-Path (CP) method [35, 36]. The Generating-Profile method for conjugate pair generation begins by designating a generating profile to a given pitch pair. From meshing kinematics, the generating curve will create its conjugate generated curve. When solving for the generated curve, a high order nonlinear equation is necessary. Thus, numerical methods are required for the solution, and accordingly the result is unpredictable in the beginning stage of design. In addition, this method is appropriate only for the design of non-identical conjugate pairs. The basic idea of the Rack-Profile method is to assign an imaginary rack to a pair of pitch curves. From the Camus theory [31], the pair of profiles generated by the rack will be conjugate to each other and to the rack as well. Implicit functions should be consid-

ered in this method unless the pitch profiles are circular. Additionally, this method is for identical pitch curves only. As far as the Contact-Path method is concerned, a contact path of the resultant generated conjugate curves is assigned to a given pitch pair at the beginning. This contact path usually has a figure 8 shape. According to this contact path, the corresponding conjugate pair can be found. Just like the Generating-Profile method, numerical methods are required to solve for the result. The Contact-Path method is limited to non-identical pitch pairs.

2.2.1 Generating-Profile method

The Generating-Profile method, as known as the popular generation method, is to designate a profile to one of the matched rotors, and then from the envelope theory, the conjugate profile of the other rotor is the envelope of the family of the designated profile. The relative motion of rotation between the paired rotors can be illustrated in Figure 2.2. The body-attached coordinate system, S_1 and S_2, are rigidly affixed to the male and female rotors. S_o is the frame of the fixed coordinate system. The rotors contact each other externally and rotate in different directions by angles, ϕ_1 and ϕ_2, respectively. Based on the constant angular velocity ratio between rotors, the relation between these two angles is

$$\phi_2 = \frac{\phi_1}{m_{12}} \tag{2.11}$$

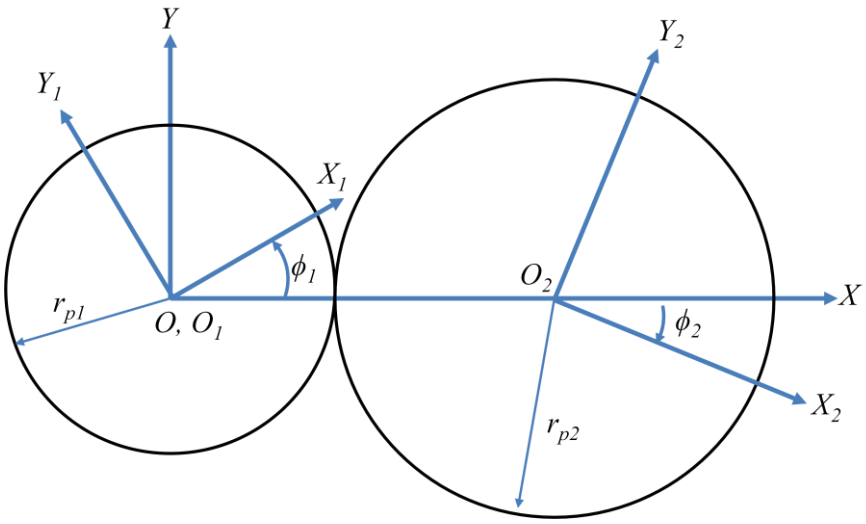

Figure 2.2: Pitch circles and coordinate systems.

Provided that the profile of the male rotor is denoted by the position vector in the coordinate system of S_1 as

$$\mathbf{r}_1(t) = [x_1(t) \;\; y_1(t) \;\; 1]^T \tag{2.12}$$

where t is the curve parameter of the male rotor profile, the unit normal vector of the profile can be derived from the position vector of the profile and expressed in the coordinate system of S_1 as

$$\mathbf{n}_1(t) = [n_{x1}(t) \;\; n_{y1}(t)]^T . \tag{2.13}$$

The envelope theory is then applied to find the profile of the female rotor. The male rotor profile is transformed onto the coordinate system of S_2 by the transformation matrix

$$\mathbf{M}_{21} = \mathbf{M}_{2o} \cdot \mathbf{M}_{o1} = \begin{bmatrix} \cos\phi_2 & -\sin\phi_2 & 0 \\ \sin\phi_2 & \cos\phi_2 & 0 \\ 0 & 0 & 1 \end{bmatrix} \begin{bmatrix} \cos\phi_1 & \sin\phi_1 & C \\ -\sin\phi_1 & \cos\phi_1 & 0 \\ 0 & 0 & 1 \end{bmatrix} . \tag{2.14}$$

The locus of the male rotor profile, which is a family of curves, is obtained

$$\mathbf{r}_2(\phi_1, t) = \mathbf{M}_{21}(\phi_1) \cdot \mathbf{r}_1(t) = [x_2(\phi_1, t) \;\; y_2(\phi_1, t) \;\; 1]^T \tag{2.15}$$

and the unit normal vector becomes

$$\mathbf{n}_2(\phi_1, t) = \mathbf{L}_{21}(\phi_1) \cdot \mathbf{n}_1(t) = [n_{x2}(\phi_1, t) \;\; n_{y2}(\phi_1, t)]^T \tag{2.16}$$

where

$$\mathbf{L}_{21} = \mathbf{L}_{2o} \cdot \mathbf{L}_{o1} = \begin{bmatrix} \cos\phi_2 & -\sin\phi_2 \\ \sin\phi_2 & \cos\phi_2 \end{bmatrix} \begin{bmatrix} \cos\phi_1 & \sin\phi_1 \\ -\sin\phi_1 & \cos\phi_1 \end{bmatrix} \tag{2.17}$$

is a sub-matrix of the matrix $\mathbf{M}_{21}$.

The profile of the female is the envelope of the family of transformed male rotor profiles and the meshing condition requires that the common normal vector must be perpendicular to the direction of the relative velocity of the contact point. Thus, the equation of meshing of the female rotor is acquired as

$$f_2(\phi_1, t) = [n_{x2}(\phi_1, t) \;\; n_{y2}(\phi_1, t)] \cdot [\frac{\partial}{\partial \phi_1}(x_2(\phi_1, t)) \;\; \frac{\partial}{\partial \phi_1}(y_2(\phi_1, t))] = 0$$

$$\Rightarrow \quad \frac{1}{m_{12}}\{[(1 + m_{12})(n_{y1} \cdot x_1 - n_{x1} \cdot y_1)] - D_{cc}[n_{y1}\cos\phi_1 + n_{x1}\sin\phi_1]\} = 0\,. \tag{2.18}$$

The conjugate profile can be found by solving angle ϕ_1 from the equation of meshing and substituting it back into Eq. (2.15).

Similarly, if the female rotor profile is given first, the male rotor profile is generated in the manner represented in the following steps. Assuming that the female rotor profile is expressed as a position vector in the coordinate system S_2

$$\mathbf{r}_2(t) = [x_2(t) \;\; y_2(t) \;\; 1]^T , \tag{2.19}$$

the unit normal vector of the profile can be derived from the position vector of the female profile and presented in the coordinate system of S_2 as

$$\mathbf{n}_2(t) = [n_{x2}(t) \;\; n_{y2}(t)]^T . \tag{2.20}$$

The locus of the female rotor profile, which is a family of curves, and the unit normal vector are expressed in the coordinate system S_1 as

$$\mathbf{r}_1(\phi_1, t) = \mathbf{M}_{12}(\phi_1) \cdot \mathbf{r}_2(t) = [x_1(\phi_1, t) \;\; y_1(\phi_1, t) \;\; 1]^T \tag{2.21}$$

and

$$\mathbf{n}_1(\phi_1, t) = \mathbf{L}_{12}(\phi_1) \cdot \mathbf{n}_2(t) = [n_{x1}(\phi_1, t) \;\; n_{y1}(\phi_1, t)]^T \tag{2.22}$$

where $\mathbf{M}_{12} = \mathbf{M}_{21}^{-1}$ and $\mathbf{L}_{12} = \mathbf{L}_{21}^{-1}$. Apply the envelope theory and the equation of meshing of the male rotor is obtained as follows:

$$f_1(\phi_1, t) = [n_{x1}(\phi_1, t) \;\; n_{y1}(\phi_1, t)] \cdot [\frac{\partial}{\partial \phi_1}(x_1(\phi_1, t)) \;\; \frac{\partial}{\partial \phi_1}(y_1(\phi_1, t))] = 0$$

$$\Rightarrow \quad -\frac{1}{m_{12}}[(1 + m_{12})(n_{y2} \cdot x_2 - n_{x2} \cdot y_2)] - D_{cc}[n_{y2} \cos(\frac{\phi_1}{m_{12}}) - n_{x2} \sin(\frac{\phi_1}{m_{12}})] = 0 . \tag{2.23}$$

Thus the male rotor profile can be obtained by solving Eq. (2.23) for the rotating angle ϕ_1 and substituting it into Eq. (2.21).

2.2.2 Rack-Profile method

The concept of the Rack-Profile method is that the paired profiles generated by a designated rack profile are conjugate to each other. As shown is Figure 2.3, a male rotor profile is cut by the concave side of the rack, and the coordinate systems, S_1 and S_r, are rigidly attached to the male rotor and the rack respectively. The pitch curve of the rack is a straight line, and hence, the male rotor rotates by an angle of ϕ_1 when the rack translates a distance, d_r, along the direction of the pitch line. With the pure rolling condition on those paired pitch curves,

$$d_r = r_{p1}\phi_1 . \tag{2.24}$$

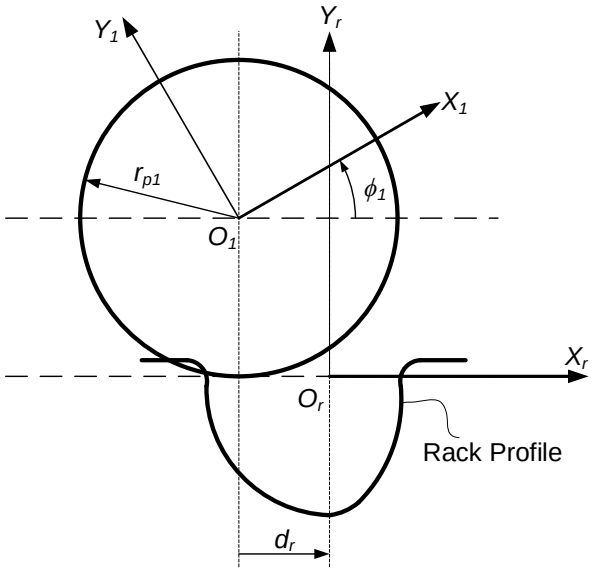

Figure 2.3: Coordinate system for Rack-Profile method to generate male rotor.

Given that the rack profile is expressed in the coordinate system, S_r, as the position vector

$$\mathbf{r}_r(t) = [x_r(t) \;\; y_r(t) \;\; 1]^T , \tag{2.25}$$

where t is the curve parameter of the rack, the unit normal vector of the profile can be derived from the position vector of the rack and represented in the coordinate system of S_r as

$$\mathbf{n}_r(t) = [n_{xr}(t) \;\; n_{yr}(t)]^T . \tag{2.26}$$

The envelope theory is used to find the profile of the male rotor. The rack profile is transformed onto the coordinate system of S_1 by the transformation matrix, $\mathbf{M}_{1r}$ and the locus of the male rotor profile, which is a family of curves, is obtain as

$$\mathbf{r}_1(\phi_1, t) = \mathbf{M}_{1r}(\phi_1) \cdot \mathbf{r}_r(t) = [x_1(\phi_1, t) \;\; y_1(\phi_1, t) \;\; 1]^T \tag{2.27}$$

and the unit normal vector becomes

$$\mathbf{n}_1(\phi_1, t) = \mathbf{L}_{1r}(\phi_1) \cdot \mathbf{n}_r(t) = [n_{x1}(\phi_1, t) \;\; n_{y1}(\phi_1, t)]^T \tag{2.28}$$

where $\mathbf{L}_{1r}$ is a sub-matrix of the matrix $\mathbf{M}_{1r}$. According to the meshing condition that the common normal vector at the contact point between the rack and the male rotor profile must be perpendicular to the direction of the relative velocity of the contact point, the equation of meshing is derived by solving the relationship between the curve parameter, t, and the angle of rotation of the male rotor, ϕ_1, as follows:

$$f_{\phi_1}(\phi_1, t) = [n_{x1}(\phi_1, t) \;\; n_{y1}(\phi_1, t)] \cdot [\frac{\partial}{\partial \phi_1}(x_1(\phi_1, t)) \;\; \frac{\partial}{\partial \phi_1}(y_1(\phi_1, t))] = 0$$

$$\Rightarrow \quad n_{yr}\, r_{p1}\, \phi_1 - n_{yr}\, x_r + n_{xr}\, y_r = 0\,. \tag{2.29}$$

The male rotor profile can be found by solving for angle ϕ_1 from the equation of meshing and substituting it back into Eq. (2.27).

After the male rotor profile is formed, the female rotor profile can be generated by applying previous procedure similarly. Here, the convex side of the rack is used to cut the groove shape of the female rotor. In Figure 2.4: Coordinate system for Rack-Profile method to generate female rotor, S_2 and S_r are rigidly attached to the male rotor and the rack respectively. The female rotor rotates by an angle of ϕ_2 when the rack translates a distance, d_r, along the direction of the pitch line. With the pure rolling condition on those paired pitch curves, the translation distance of the rack can be rewritten as

$$d_r = r_{p2}\, \phi_2 \tag{2.30}$$

The rack profile is transformed onto the coordinate system of S_2 by the transformation matrix, $\mathbf{M}_{2r}$ and the locus of the male rotor profile, which is a family of curves, is obtain as

$$\mathbf{r}_2(\phi_2, t) = \mathbf{M}_{2r}(\phi_2) \cdot \mathbf{r}_r(t) = [x_2(\phi_2, t) \;\; y_2(\phi_2, t) \;\; 1]^T \tag{2.31}$$

and the unit normal vector becomes

$$\mathbf{n}_2(\phi_2, t) = \mathbf{L}_{2r}(\phi_2) \cdot \mathbf{n}_r(t) = [n_{x2}(\phi_2, t) \;\; n_{y2}(\phi_2, t)]^T \tag{2.32}$$

where $\mathbf{L}_{2r}$ is a sub-matrix of the matrix $\mathbf{M}_{2r}$. According to the meshing condition, the common normal vector at the contact point between the rack and the male rotor profile must be perpendicular to the direction of the relative velocity of the contact point. The equation of meshing is derived for solving the relationship between the curve parameter, t, and the angle of rotation of the male rotor, ϕ_2, as follows:

$$f_{\phi_2}(\phi_2, t) = [n_{x2}(\phi_2, t) \;\; n_{y2}(\phi_2, t)] \cdot [\frac{\partial}{\partial \phi_2}(x_2(\phi_2, t)) \;\; \frac{\partial}{\partial \phi_2}(y_2(\phi_2, t))] = 0$$

$$\Rightarrow \quad n_{yr}\, r_{p2}\phi_2 - n_{yr}\, x_r + n_{xr}\, y_r = 0\,. \tag{2.33}$$

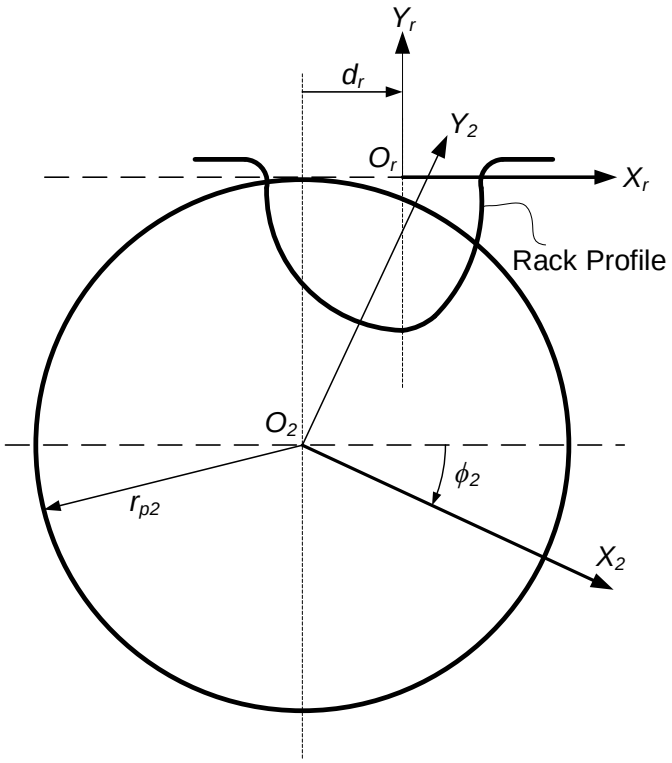

Figure 2.4: Coordinate system for Rack-Profile method to generate female rotor.

This meshing equation for the female rotor profile, $f_{\phi_2}(\phi_2, t) = 0$, is the same as the previous meshing equation, $f_{\phi_1}(\phi_1, t) = 0$, for the male rotor profile since $r_{p1}\phi_1 = r_{p2}\phi_2$. The female rotor profile can be found by solving for angle ϕ_2 from the equation of meshing and substituting it back into Eq. (2.31).

2.2.3 Contact-Path method

The mathematical model to design a pair of conjugate cross-section profiles for a twin screw compressor by using an arbitrary contact path of a figure-8 shape is discussed in this section. The contact path between the rotor cross-section profiles is the projection of the sealing line between the rotors of the compressor on the transverse plane. The term, line of action, which is used in gear terminology, and refers to the contact path. The contact patch is shown in Figure 2.5. S_o is the fixed frame, and S_1, and S_2 are the body-fixed coordinate systems of the male and female rotors respectively. The pitch point of the two pitch circles of the rotor profiles coincides with the intersection of contact path as well as with the origin, O, of the frame S_o.

The position vector

$$\mathbf{r}_c(t) = [x_c(t) \;\; y_c(t) \;\; 1]^T \tag{2.34}$$

depicts the contact path in the fixed frame S_o where t is the curve parameter. Referring to the gearing theory, the common normal at a contact point between two shapes must pass through the pitch point of the pitch curves. As a result, the common normal vector can be simply expressed in the fixed coordinate system as

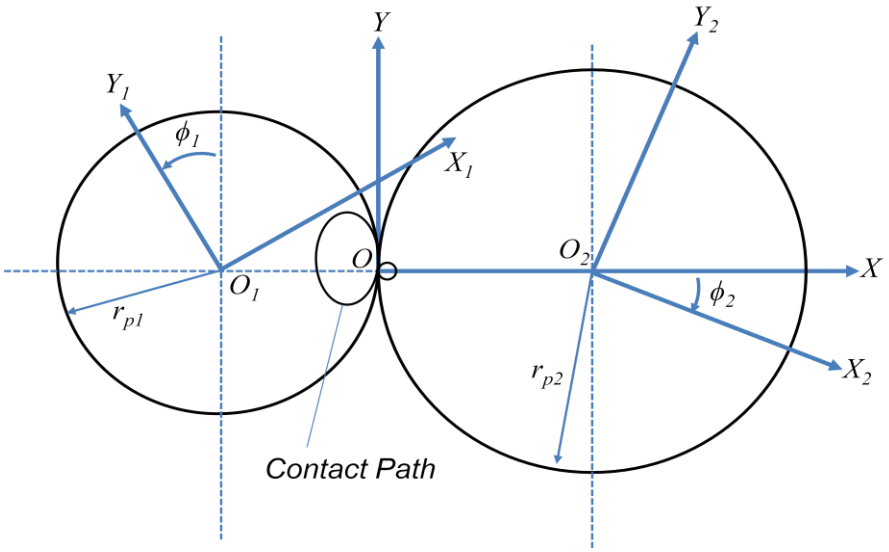

Figure 2.5: Coordinate system for Contact-Path method.

$$\mathbf{N}_c(t) = [N_{xc}(t) \;\; N_{yc}(t)]^T = [x_c(t) \;\; y_c(t)]^T . \tag{2.35}$$

The unit normal vector is denoted by

$$\mathbf{n}_c(t) = \frac{\mathbf{N}_c(t)}{\|\mathbf{N}_c(t)\|} = [n_{xc}(t) \;\; n_{yc}(t)]^T = [\frac{x_c(t)}{\sqrt{x_c^2(t)+y_c^2(t)}} \;\; \frac{y_c(t)}{\sqrt{x_c^2(t)+y_c^2(t)}}]^T . \tag{2.36}$$

The contact path can be transformed from the fixed frame S_o to the coordinate system S_1 to form a family of curves.

$$\mathbf{r}_1(\phi_1, t) = \mathbf{M}_{1o}(\phi_1) \cdot \mathbf{r}_c(t) = [x_1(\phi_1, t) \;\; y_1(\phi_1, t) \;\; 1]^T \tag{2.37}$$

where

$$\phi_1 = \phi_1(t)$$

$$\mathbf{M}_{1o} = \begin{bmatrix} -\cos\phi_1 & -\sin\phi_1 & r_{p1}\cos\phi_1 \\ \sin\phi_1 & -\cos\phi_1 & -r_{p1}\sin\phi_1 \\ 0 & 0 & 1 \end{bmatrix}$$

$$x_1(\phi_1, t) = r_{p1}\cos\phi_1 - x_c\cos\phi_1 - y_c\sin\phi_1$$

$$y_1(\phi_1, t) = -r_{p1}\sin\phi_1 + x_c\sin\phi_1 - y_c\cos\phi_1 .$$

Similarly, if the contact path is transformed from the fixed frame S_o to the coordinate system S_2, the locus is represented as

$$\mathbf{r}_2(\phi_2, t) = \mathbf{M}_{2o}(\phi_2)\cdot\mathbf{r}_c(t) = [x_2(\phi_2, t) \;\; y_2(\phi_2, t) \;\; 1]^T . \tag{2.38}$$

Since

$$\phi_2 = \frac{\phi_1(t)}{m_{12}} , \tag{2.39}$$

the locus is rewritten as

$$\mathbf{r}_2(\phi_1, t) = \mathbf{M}_{2o}(\phi_1)\cdot\mathbf{r}_c(t) = [x_c(\phi_1, t) \;\; y_c(\phi_1, t) \;\; 1]^T \tag{2.40}$$

where

$$\mathbf{M}_{2o} = \begin{bmatrix} \cos(\frac{\phi_1}{m_{12}}) & -\sin(\frac{\phi_1}{m_{12}}) & r_{p2}\cos(\frac{\phi_1}{m_{12}}) \\ \sin(\frac{\phi_1}{m_{12}}) & \cos(\frac{\phi_1}{m_{12}}) & r_{p2}\sin(\frac{\phi_1}{m_{12}}) \\ 0 & 0 & 1 \end{bmatrix}$$

$$x_2(\phi_1,t) = r_{p2}\cos(\frac{\phi_1}{m_{12}}) + x_c\cos(\frac{\phi_1}{m_{12}}) - y_c\sin(\frac{\phi_1}{m_{12}})$$

$$y_2(\phi_1,t) = r_{p2}\sin(\frac{\phi_1}{m_{12}}) + x_c\sin(\frac{\phi_1}{m_{12}}) + y_c\cos(\frac{\phi_1}{m_{12}}).$$

The unit normal vector $\mathbf{n}_c(t)$ in the fixed frame should be transformed to the coordinate system S_1 (or to the coordinate system S_2) in order to derive the meshing equation. The normal vector transformation is as follows:

$$\mathbf{n}_1(\phi_1,t) = \mathbf{L}_{1o}(\phi_1)\cdot\mathbf{n}_c(t) = [n_{x1}(\phi_1,t)\ \ n_{y1}(\phi_1,t)]^T$$

$$= [-\frac{x_c(t)\cos\phi_1}{\sqrt{x_c^2(t)+y_c^2(t)}} - \frac{y_c(t)\sin\phi_1}{\sqrt{x_c^2(t)+y_c^2(t)}} \quad \frac{x_c(t)\sin\phi_1}{\sqrt{x_c^2(t)+y_c^2(t)}} - \frac{y_c(t)\cos\phi_1}{\sqrt{x_c^2(t)+y_c^2(t)}}]^T \qquad (2.41)$$

where $\mathbf{L}_{1o}$ is a sub-matrix of matrix $\mathbf{M}_{1o}$. Consequently, the meshing equation is derived as

$$f_{\phi_1}(\phi_1,t) = [n_{x1}(\phi_1,t)\ \ n_{y1}(\phi_1,t)]\cdot[\frac{\partial}{\partial t}(x_1(\phi_1,t))\ \ \frac{\partial}{\partial t}(y_1(\phi_1,t))] = 0$$

$$\Rightarrow \quad \frac{x_c(t)\cdot x_c'(t) + y_c(t)[y_c'(t) + r_{p1}\phi_1'(t)]}{\sqrt{x_c^2(t)+y_c^2(t)}} = 0. \qquad (2.42)$$

The equation above is used to find the relationship between the angle of rotation ϕ_m and the curve parameter t by the integration

$$\phi_1(t) = -\frac{1}{r_{p1}}\int_{t_1}^{t_2}\frac{x_c(t)\cdot x_c'(t) + y_c(t)\cdot y_c'(t)}{y_c(t)}\,dt + \phi_0 \qquad (2.43)$$

where ϕ_0 is the accumulated rotation angle of the last segment. One of the numerical algorithm should be applied for the integration to find the rotational angle ϕ_1. Then, the angle of rotation ϕ_2 can be evaluated by Eq. (2.39). Finally, the profiles of the male and female rotors are obtained by substituting those angles of rotation into Eqs. (2.37) and (2.38).

2.3 Three-Dimensional Rotor Surface

The rotors of the twin screw compressor have parallel axes and constant axial leads. Once the cross-section profiles of both rotors are known, each of the three-dimensional rotor surfaces is generated by simultaneously revolving the profile about the corresponding rotor axis and translating the profile along the same axis.

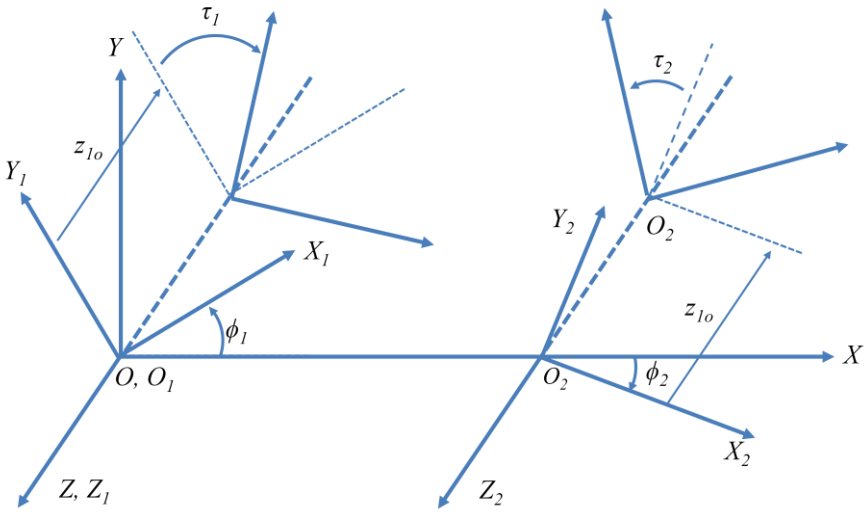

Figure 2.6: Coordinate systems to generate rotor surfaces.

Referring to Figure 2.6, the rotor profiles are expressed in their corresponding body-fixed coordinate systems S_1 and S_2 as the position vectors

$$\mathbf{r}_1(t) = [x_1(t) \;\; y_1(t) \;\; 0]^T \tag{2.44}$$

and

$$\mathbf{r}_2(t) = [x_2(t) \;\; y_2(t) \;\; 0]^T . \tag{2.45}$$

The three-dimensional rotor surfaces at a male rotational angle ϕ_1 are acquired and shown in the fixed coordinate system S_o as follows:

$$\mathbf{r}_{1o}(t, \phi_1, \tau_1) = [x_{1o}(t, \phi_1, \tau_1) \;\; y_{1o}(t, \phi_1, \tau_1) \;\; z_{1o}(t, \phi_1, \tau_1)]^T \tag{2.46}$$

and

$$\mathbf{r}_{2o}(t, \phi_1, \tau_1) = [x_{2o}(t, \phi_1, \tau_1) \;\; y_{2o}(t, \phi_1, \tau_1) \;\; z_{2o}(t, \phi_1, \tau_1)]^T \tag{2.47}$$

where

$$x_{1o}(t, \phi_1, \tau_1) = x_1(t)\cos(\phi_1 - \tau_1) + y_1(t)\sin(\phi_1 - \tau_1)$$

$$y_{1o}(t, \phi_1, \tau_1) = -x_1(t)\sin(\phi - \tau) + y_1(t)\cos(\phi - \tau)$$

$$z_{1o}(t, \phi_1, \tau_1) = z_{1o}(\tau_1) = \frac{L_w}{\tau_{w1}}\tau_1$$

$$x_{2o}(t, \phi_1, \tau_1) = D_{cc} + x_2(t)\cos[\frac{1}{m_{12}}(\phi_1 - \tau_1)] - y_2(t)\sin[\frac{1}{m_{12}}(\phi_1 - \tau_1)]$$

$$y_{2o}(t, \phi_1, \tau_1) = x_1(t)\sin[\frac{1}{m_{12}}(\phi_1 - \tau_1)] + y_2(t)\cos[\frac{1}{m_{12}}(\phi_1 - \tau_1)]$$

$$z_{2o}(t, \phi_1, \tau_1) = z_{2o}(\tau_1) = \frac{L_w}{\tau_{w1}}\tau_1$$

where L_w is the rotor length, τ_{w1} is the wrap angle, and τ_1 is the twist parameter of the male rotor. If the center-to-center distance and the rotational angle are set to be zero, the results reveal the rotor surfaces attached to the body fixed coordinate systems.

2.4 Interlobe Sealing Curve

When the two rotors of a screw compressor rotate accordingly, the contact points form the contact curve. This curve is known as the interlobe sealing curve, in Figure 2.7a. The projection of the interlobe sealing line onto the *xy*-plane is previously mentioned line of action, shown in Figure 2.7b. The interlobe sealing line is determined by solving the equation of either the male or female rotor surface equation with the modified equation of meshing in three-dimensional space. Taking the male rotor surface as an example, the curve parameter t of the two-dimensional profile and the rotational angle ϕ_1 are constrained by the equation of meshing, Eq. (2.18). In three-dimensional space, the curve parameter should be constrained to $(\phi_1 - \tau_1)$ because of the screw motion of the rotor profile. As a result, the three-dimensional sealing curve is represented as

$$x_{1o}(t, \phi_1, \tau_1) = x_1(t)\cos(\phi_1 - \tau_1) + y_1(t)\sin(\phi_1 - \tau_1) \quad (2.48a)$$

$$y_{1o}(t, \phi_1, \tau_1) = -x_1(t)\sin(\phi - \tau) + y_1(t)\cos(\phi - \tau) \quad (2.48b)$$

$$z_{1o}(t, \phi_1, \tau_1) = z_{1o}(\tau_1) = \frac{L}{\tau_{w1}}\tau_1 \tag{2.48c}$$

$$\frac{1}{m_{12}}\{[(1+m_{12})(n_{y1}\cdot x_1 - n_{x1}\cdot y_1)] - D_{cc}[n_{y1}\cos(\phi_1-\tau_1) + n_{x1}\sin(\phi_1-\tau_1)]\} = 0\,. \tag{2.48d}$$

The equation of meshing in the three dimensional space can be rearranged in the form

$$(\phi_1 - \tau_1) = f_1(t)\,. \tag{2.49}$$

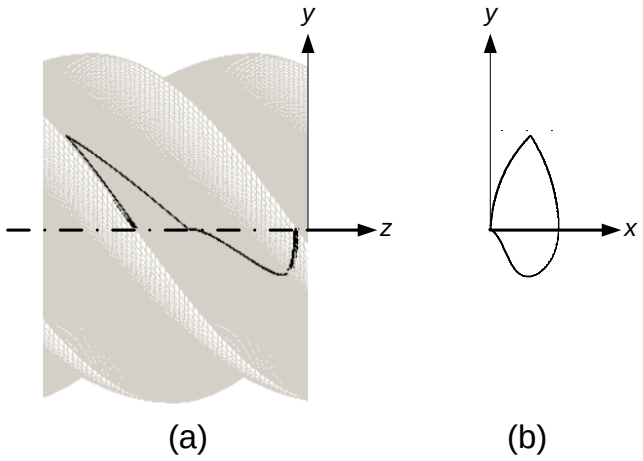

Figure 2.7: Projections of the Interlobe sealing line (a) on a rotor (b) on *xy*-plane.

The shape of the interlobe sealing line is independent to the rotation of the rotors and does not change. As the male rotor rotates, however, the interlobe sealing line translates axially along the *z*-axis. To find the shape of the sealing line, the rotational angle ϕ_1 can be set to any value and then the relationship between the value of profile parameter t and the value of twist angle τ_1 can be determined by Eq. (2.49). The coordinates of the interlobe sealing line can then be evaluated by substituting those angles into Eq. (2.48). The total length of one period of sealing line is

$$l_{SL} = \int_{t_s}^{t_f} \sqrt{[dx_{1o}(t)]^2 + [dy_{1o}(t)]^2 + [dz_{1o}(t)]^2} \tag{2.50}$$

where t_s and t_f correspond to the beginning and end points of a lobe of the profile.

2.5 Chamber Volume

When the screw compressor is under operation, its male and female rotors engage with each other and multiple chambers exist at the same time. Each chamber is surrounded by rotor surfaces, cylindrical surface of the compressor housing, and the suction and/or discharge plane. The volume of the chamber changes as the rotors rotate to achieve the compression process, so it is a function of the rotational angle. This function is called the volume curve of the compressor chamber. It is calculated by summing up the cross-section cavity area along the rotor axis. Assuming a male rotational angle ϕ_1, the cavity area is bounded by a set of curves expressed in the parametric form

$$\begin{aligned} x_i &= x_i(t_i) \\ y_i &= y_i(t_i) \end{aligned} \tag{2.51}$$

the cavity area is integrated by

$$A_z(\phi_1) = \frac{1}{2}\oint x dy - y dx$$

$$= \frac{1}{2}\sum_i \left(\int_{y_{i,\min}}^{y_{i,\max}} x_i dy_i - \int_{x_{i,\min}}^{x_{i,\max}} y_i dx_i\right)$$

$$= \frac{1}{2} \sum_i \int_{t_{i,\min}}^{t_{i,\max}} (x_i y_i' - y_i x_i') \, \mathrm{d}t_i \, . \tag{2.52}$$

The integration can be computed analytically if the curves are given in the form of analytical functions. As soon as the cavity areas are evaluated, the volume of the chamber at rotational angle ϕ_1 is

$$V(\phi_1) = \sum A_z(\phi_1) \Delta z \tag{2.53}$$

where

$$\Delta z = \frac{L}{\tau_{w1}} \Delta \tau_1 \, .$$

2.6 Blowhole

Since the interlobe sealing curve of the rotors usually does not reach the housing cusp, a small leakage opening near the cusp exists between the neighboring cavities. It is called a blowhole, which is a leakage pathway with a triangular shaped surface in the three dimensional space. The surface is bounded by two curves on the male and female rotor surfaces adjacent to each rotor tip and the straight housing cusp line. The vertices are the intersection of the male rotor tip with the housing cusp, the intersection of the female rotor tip with the housing cusp, and the contact point between rotors which is closest to the housing cusp. The contact point closest to the housing cusp is always the first contact point in a cycle. The blowhole can be approximated as a curvilinear triangle on a plane formed by the three aforementioned vertices. Then two edges of the curvilin-

ear triangle are curves formed by intersecting the plane with the male and female rotor surfaces and the third edge is still the straight housing cusp line. The area of the curvilinear triangle is called the blowhole area. The blowhole area calculation can be further simplified by assuming the defined plane is parallel to the rotor axes.

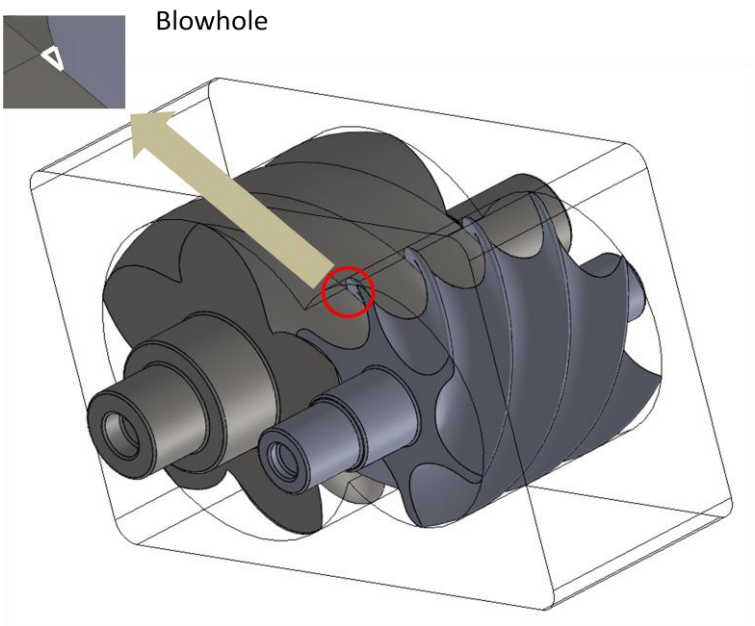

Figure 2.8: Blowhole

Quite a few methods with different complexity and accuracy have been proposed to define and evaluate the blowhole area [49, 50]. In this study the method of blowhole definition by Singh and Bowman [49] is modified for better accuracy.

Assuming that the cross-section profiles of the rotors and the meshing line are given, the blowhole area is calculated and the detailed procedure is described in the following.

First, the vertices of the blow hole are located. The blow hole is on a plane containing the housing cusp line SS and the tip of line of action, which is also known as the mesh-

ing line, and it is a line from the end view in Figure 2.9. The housing cusp line is represented as a point S and its coordinates are

$$x_S = \frac{1}{2D_{cc}}(r_{o1}^2 - r_{o2}^2 + D_{cc}^2) \tag{2.54a}$$

$$y_S = -\sqrt{r_{o1}^2 - x_S^2} \tag{2.54b}$$

where r_{o1} and r_{o1} are the outer diameters of the male and female rotors respectively and D_{cc} is the center to center distance between two rotor shafts.

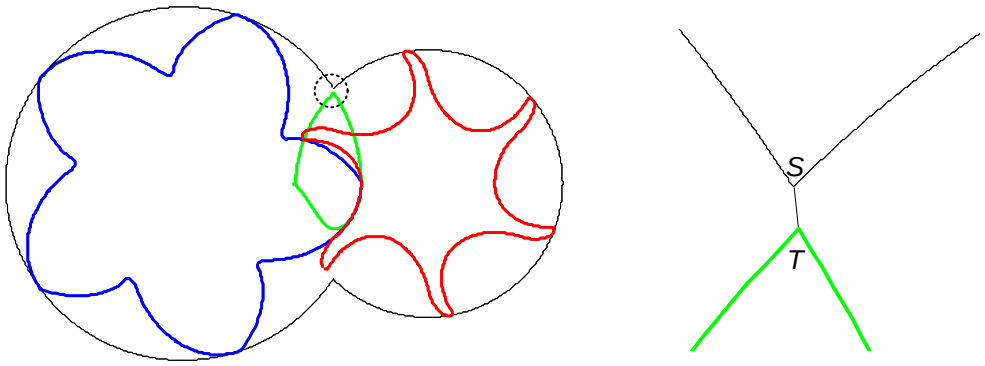

Figure 2.9: End view of the blowhole.

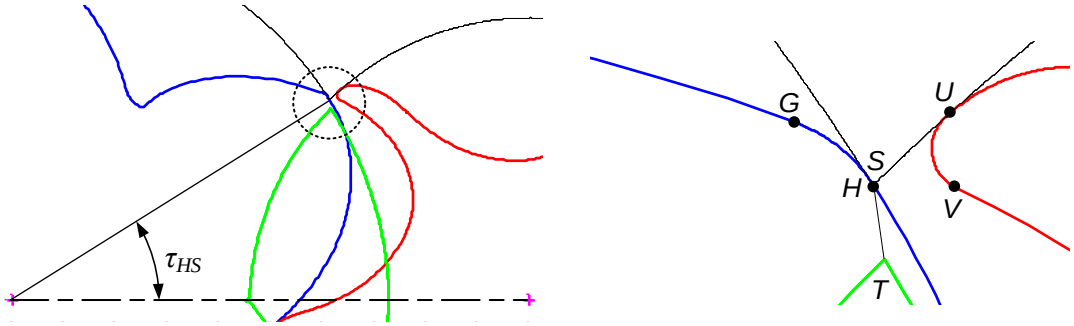

Figure 2.10: Calculation of the blowhole area.

Based on the given data of rotor profiles, the coordinates of the male rotor's tip H, meshing line tip T, and points G and V, which will come in contact with the meshing line tip T, all on the male and female rotors, can be found in Figure 2.10.

Then, the twist angle from the rotor's neutral position is computed. When the male rotor's tip is in contact with the female rotor, the rotors are said to be in neutral position. Accordingly, the angle τ_{HS} is the turning angle of the male rotor away from its neutral position when points S and H coincide and the angle τ_{GT} is the turning angle of the male rotor when the points G and T coincide. Those two angles indicate the positions when the leaking starts and ends: that is, the blow hole starts to form and evolves completely. Consequently, in the interval between angles τ_{HS} and τ_{GT}, the blow hole is found. When the blow hole is evolving, only part of the line ST is covered by the male and female rotors' profiles. The line segment on the line ST which is not covered the rotors is calculated and integrated along the axial direction to acquire the blowhole area. The equation of line ST can be represented as

$$y - y_S = m(x - x_S) \tag{2.55}$$

where

$$m = \frac{y_T - y_S}{x_T - x_S}$$

Then transform the data point coordinates of segment HG onto the fixed coordinate system and find that between data points with indices i and $(i+1)$, segment HG intersects line ST. The line connecting those two points is

$$\frac{y - y_2(i)}{x - x_2(i)} = \frac{y_2(i+1) - y_2(i)}{x_2(i+1) - x_2(i)} \tag{2.56}$$

So the intersection point N can be found by solving Eqs (2.55) and (2.56). A similar approach is utilized to find the length of segment SR covered by the female rotor. Sequentially, the length of the segment which is not covered by the male and female rotors is

$$h = ST - SR - TN$$

It is a function of angle of twist. When the male rotor profile twists by $\Delta\tau$, the point on the profile translates a distance Δz along the rotor axis.

$$\Delta z = \frac{L}{\tau_{w1}} \Delta\tau \tag{2.57}$$

Finally, the blowhole area is obtained by integrating h along the axial direction using a numerical integration method, such as the trapezoidal rule or Simpson's rule.

2.7 Conclusions

The geometry parameters and properties of the twin screw compressors are fundamental to the simulation models and should be predefined and derived as the input data to the simulation. In this chapter, the geometry parameters of the twin screw compressor are depicted and three methods for computation of twin screw compressor profile are discussed. With acquisition of the geometric parameters and the profiles of the twin screw compressors, the compressor geometric characteristics such as the cavity vol-

ume, interlobe sealing line, and the blowhole can be computed for further use. All those calculated characteristics are expressed as functions of the male rotor angular position to be further used for evaluating the performance of the compressor.

Chapter 3

Development of Bezier Curve-Based Deviation-Function Method for Twin Screw Compressor Design

3.1 Introduction

The generation of the twin screw compressor profiles is to derive conjugate pairs. Three different methods for rotor profile generation are discussed in detail in Chapter 2. Unique limitations are encountered when one of those methods is adopted. The deviation function method is a relatively new method for conjugate pair design. The theory is based on reshaping an original pitch curve by a function describing the amount of deviation between contact point on the conjugate pair and that on the corresponding pitch pair. This method has some advantages over conventional methods, such as more design possibilities can be generated; the design process is more intuitive; the mechanical properties and analysis can be incorporated during the process; and noncircular pitch curves can be utilized without solving higher order nonlinear equations [51]. This method was applied to lobe pumps with identical, external pitches [52, 53]. The trapping-free lobe pumps with better sealing rotors were designed by using the deviation function

method by Liu et al [54]. The deviation function method was also developed for generating the profiles of rotors with internal contact [55]. Yan et al. [56 - 58] developed the general deviation function algorithm specifically for internal non-circular pitch curves and applied this method to gerotor pumps. In this chapter, the Bezier curve-base deviation function method is developed for the twin screw compressor design.

3.2 Deviation Function Method

To address the limitations of existing methods, Yang et al. [37] developed an innovative method, called the Deviation-Function (DF) method, for conjugate pair generation in 1999. For external-meshing kinematic pairs, it's applied to generate identical symmetric rotors with circular or non-circular pitch curves. Once the pitch curves are constructed as either circular or non-circular, an appropriate deviation function is chosen to reshape the pitch profiles. The concept of deviation function comes from the idea that the slipping usually occurs at the contact points of a conjugate pair. The reason this happens is because the contact points on the conjugate pair deviate from those on their pitch curves. If the amount of deviation can be expressed as a function of angular displacement of the pitch curve motion, it becomes the so-called deviation function with an angular argument.

Now referring to Figure 3.1, let p_1 and p_2 be a pair of non-circular pitches, and let g_1 and g_2 be the corresponding generated conjugate curves reshaped by the deviation function. The contact point, *P*, between pitch curves is always on the line of fixed centers of rotation. The generated conjugate curves are permanently attached to the pitch

curves. However, the contact point, *G*, between generated conjugate curves is offset from the point *P* most of the time and the offset amount is the deviation denoted by e. The contact point, *P*, is a function of rotation angle, as is the contact point, *G*. Thus, the deviation function, which is the distance between points *P* and *G*, can be expressed as

$$e(\theta_1) = \left\| P(\theta_1) - G(\theta_1) \right\|, \text{ for } 0 \le \theta_1 \le \phi_1 \tag{3.1}$$

where, θ_1 is the rotational angle of pitch p_1 and ϕ_1 is the design range of lobe profile.

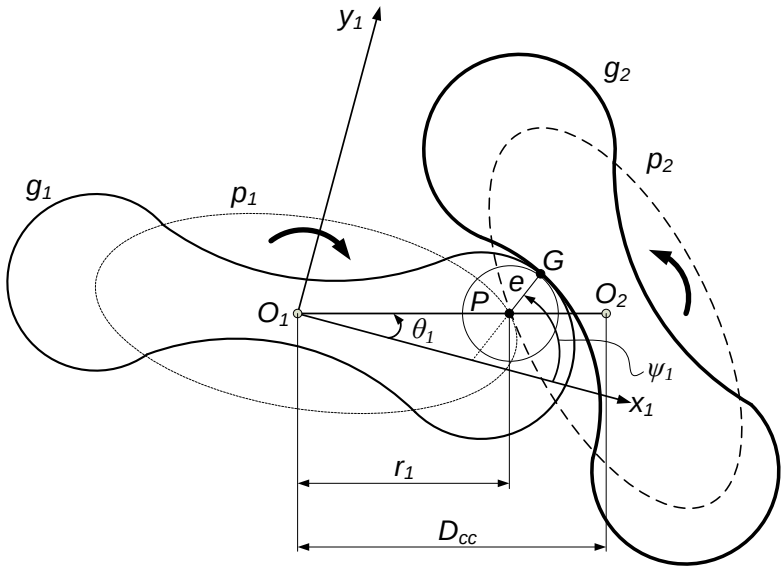

Figure 3.1: Pitch curves and generated conjugate pairs.

In Figure 3.1, point *G* can be observed as a point on a circle whose center *P* is coincident to the contact point of the pitch curves, and whose radius is deviation *e*. As point *P* moves along the pitch curve, a family of circles whose centers are pitch contact points, $P(\theta_1)$, and radii are deviation function, $e(\theta_1)$. The set of contact points, $G(\theta_1)$, of the generated conjugate curves can be found as the envelope of this family of circles. Supposed that this family of circles is depicted implicitly as

$$C(x, y, \theta_1) = (x - r_1 \cos\theta_1)^2 + (y - r_1 \sin\theta_1)^2 - e^2 = 0\,. \tag{3.2}$$

Accordingly, the envelope must satisfy the following condition

$$\frac{\partial C(x, y, \theta_1)}{\partial \theta_1} = 0\,. \tag{3.3}$$

By solving Eqs. (3.2) and (3.3) simultaneously, the expression for the envelope, which is also referred as the generated curve, is obtained as

$$\begin{aligned} g_{1x} &= r_1 \cos\theta_1 + e\cos\psi_1 \\ g_{1y} &= r_1 \sin\theta_1 + e\sin\psi_1 \end{aligned} \tag{3.4}$$

where, ψ_1 represents the angle of the common normal at *G* with respect to body-fixed coordinate frame, S_1, and is a function of θ_1 which is depicted as

$$\psi_1 = \theta_1 - \tan^{-1}\left(\frac{r_1'}{r_1}\right) + \tan^{-1}\left(\frac{e'}{\sqrt{r_1^2 + r_1'^2 - e'^2}}\right) + \pi \tag{3.5a}$$

or

$$\psi_1 = \theta_1 - \tan^{-1}\left(\frac{r_1'}{r_1}\right) - \tan^{-1}\left(\frac{e'}{\sqrt{r_1^2 + r_1'^2 - e'^2}}\right) \tag{3.5b}$$

where

$$r_1' = \frac{dr_1}{d\theta_1}$$

and

$$e' = \frac{de}{d\theta_1}.$$

When this method is applied, a deviation function $e(\theta_1)$ is needed only in the interval of $0 \le \theta_1 \le \phi_1$. C^1 continuity at $\theta_1 = \phi_1$ can be guaranteed by complying with the condition $e(\phi_1) = 0$ as the pitch curves are identical. Figure 3.2 shows a generated profile and the family of circles.

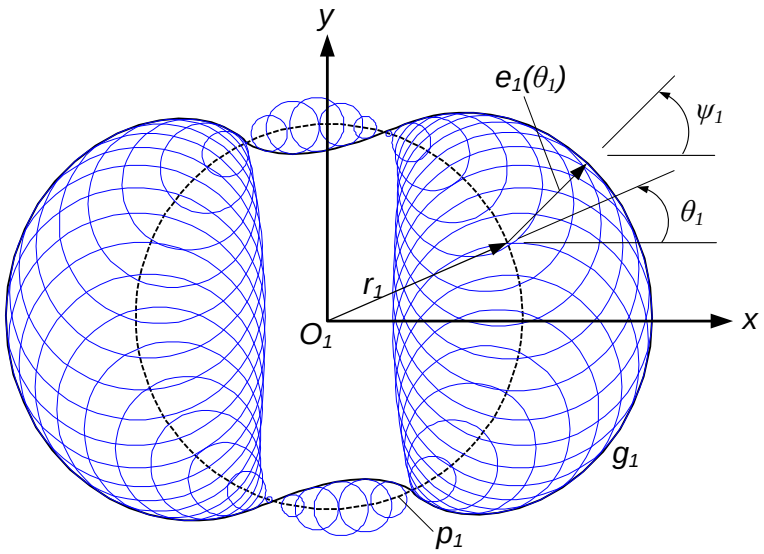

Figure 3.2: A generated profile.

3.3 Bezier Curve

The Bezier curve is one of the parametric functions and is frequently used in computer graphics and computer-aided design (CAD) systems nowaday. It was developed and named after the French engineer, Pierre Bezier, in the early 1960's and was applied to design automotive bodies at that time. The Bezier curve is the most numerically stable

among all the polynomial-based curves and thus suitable for depicting even more complex piecewise polynomial curves. It will be utilized here to define the deviation functions in this study and explained in the following section.

A Bezier curve is controlled by a set of control points, $\mathbf{P}_i$, where $i = 0 \sim n$ and n is called the order of the curve. This kind of curve always passes through the first and last control points, but not through the intermediate ones, if there are any. They are contained in the convex hull (or convex envelope) formed by the control points. A Bezier curve, $\mathbf{P}(u)$, is expressed as

$$\mathbf{P}(u) = \sum_{i=0}^{n} \mathbf{P}_i \, B_{i,n}(u), \quad u \in [0,1] \tag{3.6}$$

where u is its normalized parameter and $B_{i,n}(u)$ is called the Berstein polynomial which has the form

$$B_{i,n}(u) = C(n,i)\, u^i \, (1-u)^{n-i} \tag{3.7}$$

where

$$C(n,i) = \frac{n!}{i!(n-i)!}$$

is the binomial coefficient.

Bezier curves have the following properties:

1. The endpoint interpolation property means that the curve always begins at starting point, $\mathbf{P}_0$, and ends at final point, $\mathbf{P}_n$. That is

$\mathbf{P}(0) = \mathbf{P}_0$ and $\mathbf{P}(1) = \mathbf{P}_n$

2. The tangents of two endpoints of the curve are in line to the first and the last segments of the control polygon, respectively. Mathematically speaking,

$\overset{\circ}{\mathbf{P}}(0) = k_0(\mathbf{P}_1 - \mathbf{P}_0)$ and $\overset{\circ}{\mathbf{P}}(1) = k_1(\mathbf{P}_n - \mathbf{P}_{n-1})$

3. The higher derivatives at the two endpoints are liner combinations of the respective order of the segments of the control polygon. Take the second-order derivative as an example

$\overset{\circ\circ}{\mathbf{P}}(0) = k_{01}(\mathbf{P}_1 - \mathbf{P}_0) + k_{02}(\mathbf{P}_2 - \mathbf{P}_1)$

4. The superposition of all Berstein polynomials, $B_{i,n}(u)$, is symmetric.
5. Bezier curves have the convex hull property with respect to their control polygon.

3.4 Screw Compressor Cross-Sectional Profile Design via Bezier Curve-Based Deviation Functions

The procedure described in Section 3.2 is applicable to either circular or non-circular pitches for generating identical rotors with symmetric lobe profile. However, in order to design cross-sectional profiles for the twin screw compressors, only circular pitches are appropriate. The reason is every point on the contact path (line of action) between the male rotor and the female rotor must have the same velocity in order for the two rotational shafts to possess a unique speed ratio at each instance. The paired pitches for

male and female rotors can have different radii instead of being identical. Usually the number of lobes of a male rotor is more than that of a mated female rotor. This implies that the radius of the pitch of a male rotor is smaller than that of the corresponding female rotor. For the symmetry of the lobe profile, a non-symmetric lobe profile is preferable because it results in better performance in almost all aspects. With these concerns in mind, the procedure for generating non-identical non-symmetric rotor cross-sectional profiles of twin screw compressors is explained in the following section.

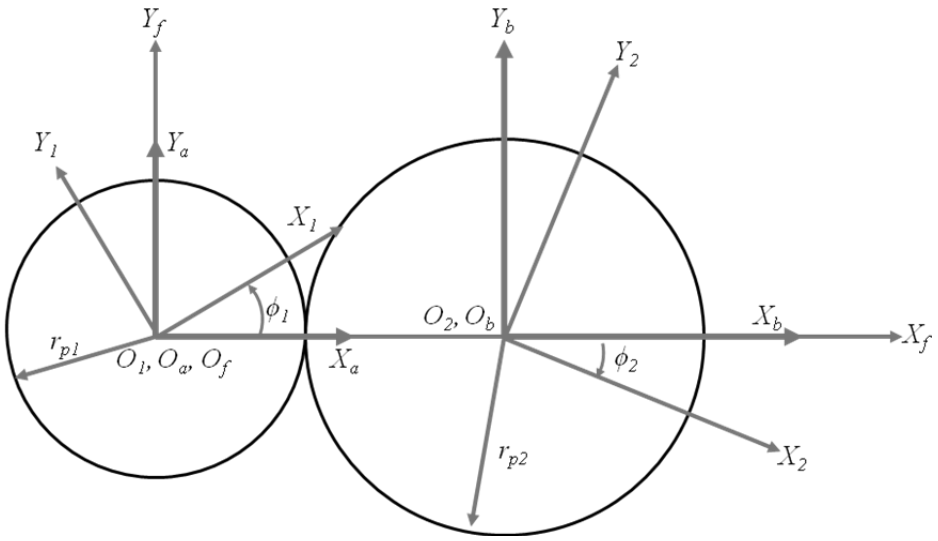

Figure 3.3: Pitch circles and coordinate systems.

Consider the relative motion of the two rotor axes, as shown in Figure 3.3. Coordinate systems S_1, and S_2 are rigidly attached to the male rotor and the female rotor, respectively and S_f is the fixed frame. The paired rotors rotate about parallel axes with a constant ratio of angular velocities, m_{12}, which can be expressed as

$$m_{12} = \frac{N_2}{N_1} = \frac{r_{p_2}}{r_{p_1}} = \left|\frac{\omega_1}{\omega_2}\right| = \left|\frac{\phi_1}{\phi_2}\right| \tag{3.8}$$

where N is the number of lobes, r_p is the radius of the pitch circle, ω is the angular velocity, ϕ is the angular displacement, and subscripts 1 and 2 represent the male and female rotors, respectively. Prior to designing the paired rotor profiles, the constant speed ratio, m_{12}, and center to center distance, D_{cc}, need to be determined. This implies that the numbers of lobes, N_1 and N_2, should be defined to satisfy this ratio and pitch radii of each rotor can be calculated as follows:

$$r_{p_1} = \frac{1}{1+m_{12}} D_{cc} \tag{3.9a}$$

$$r_{p_2} = \frac{m_{12}}{1+m_{12}} D_{cc}. \tag{3.9b}$$

After these preceding parameters are determined, rotor profile design begins by selecting a legitimate deviation function for the male rotor. By using Bezier curves, the number of design possibilities is unlimited and asymmetric profiles are easy to achieve with the compliance of boundary conditions. The Bezier curve-based deviation function has the parametric form

$$\mathbf{P}(u) = \begin{bmatrix} \theta_1(u) \\ e_1(\theta_1(u)) \end{bmatrix}, \quad u \in [0,1] \tag{3.10}$$

They should be defined in the range

$$0 \le \theta_1 \le \theta_{r,1}$$

where

$$\theta_{r,1} = \frac{2\pi}{N_1}$$

In order for the compressor to operate smoothly, it is obvious that the rotor profile must be a close curve without interruptions. Accordingly, the deviation function for a single lobe of the rotor must not have any interruptions and C^1 continuity should be established within the entire curve. In addition, due to the repetition of the lobe of the rotor, such continuity condition is supposed to be maintained at the beginning and end points of the deviation function for a single lobe of the rotor. Using Bezier curve-based deviations facilitates the fulfillment of this condition. By observing the first two properties of the Bezier curves listed in previous section, the first two control points, $\mathbf{P}_0$ and $\mathbf{P}_1$, and last two control points, $\mathbf{P}_{n-1}$ and $\mathbf{P}_n$, are selected to satisfy the following two conditions

$$e_1(\theta_1(0)) = e_1(\theta_1(1)) \tag{3.11a}$$

where $\theta_1(0) = 0$ and $\theta_1(1) = \theta_{r,1}$

$$k_0(\mathbf{P}_1 - \mathbf{P}_0) = k_1(\mathbf{P}_n - \mathbf{P}_{n-1}) \tag{3.11b}$$

The former condition specifies that at the endpoints the profile has the same deviation, and the latter condition specifies that the first and last segments of the control polygon are parallel. To meet these two conditions, at least four points should be specified, which requires that the order of the Bezier curve is at least three, i.e. $n \geq 3$.

Once the deviation function is created, the lobe profile for the male rotor can be generated as follows:

$$x_1 = r_{p_1}\cos\theta_1 + e_1\cos\psi_1$$
$$y_1 = r_{p_1}\sin\theta_1 + e_1\sin\psi_1 \tag{3.12}$$

where

$$\psi_1 = \theta_1 + \tan^{-1}\left(\frac{e_1'}{\sqrt{r_{p_1}^2 - e_1'^2}}\right) + \pi \tag{3.12a}$$

or

$$\psi_1 = \theta_1 - \tan^{-1}\left(\frac{e_1'}{\sqrt{r_{p_1}^2 - e_1'^2}}\right). \tag{3.12b}$$

Here, the derivative e_1' is the differentiation with respect to θ_1, i.e. $e_1' = de_1 / d\theta_1$. And in order for the inverse tangent function to have real result, the derivative of the deviation function is bounded by

$$-r_{p_1} \le e_1' \le r_{p_1}. \tag{3.13}$$

The female rotor profile, which is conjugate to the male one, can be generated by applying envelope theory. First, we have to find the family of curves formed by the male rotor profile. This can be expressed as

$$\mathbf{r}_2(\theta_1, \phi_1) = [x_2,\, y_2,\, 1]^T = \mathbf{M}_{21}(\phi_1)\,\mathbf{r}_1(\theta_1) \tag{3.14}$$

where $\mathbf{M}_{21}(\phi_1)$ is the transformation matrix

$$\mathbf{M}_{21} = \mathbf{M}_{2b}\mathbf{M}_{ba}\mathbf{M}_{a1}$$

$$\mathbf{M}_{a1} = \begin{bmatrix} \cos\phi_1 & \sin\phi_1 & 0 \\ -\sin\phi_1 & \cos\phi_1 & 0 \\ 0 & 0 & 1 \end{bmatrix}$$

$$\mathbf{M}_{ba} = \begin{bmatrix} 1 & 0 & -A_c \\ 0 & 1 & 0 \\ 0 & 0 & 1 \end{bmatrix}$$

$$\mathbf{M}_{2b} = \begin{bmatrix} \cos\phi_2 & \sin\phi_2 & 0 \\ -\sin\phi_2 & \cos\phi_2 & 0 \\ 0 & 0 & 1 \end{bmatrix}.$$

Apply envelope theory to the family of curves

$$\frac{\partial \mathbf{r}_2}{\partial \phi_1} \times \frac{\partial \mathbf{r}_2}{\partial \theta_1} = 0. \tag{3.15}$$

Then we have

$$\frac{1}{i_{12}} \left\{ \left[(1+i_{12})(n_{y1}x_1 - n_{x1}y_1) \right] - A_c \left[n_{y1}\cos\phi_1 + n_{x1}\sin\phi_1 \right] \right\} = 0 \tag{3.16}$$

where $\mathbf{n} = (n_{x1}, n_{y1})$ is the normal vector of the male rotor profile. Solving for kinematic variable, ϕ_1, we obtain

$$\phi_1 = \tan^{-1}\left(\frac{\eta}{\sqrt{1-\eta^2}}\right) - \tan^{-1}\left(\frac{n_{y1}}{n_{x1}}\right) \tag{3.17}$$

where

$$\eta = \frac{(1+i_{12})(n_{y1}x_1 - n_{x1}y_1)}{A_c}. \tag{3.18}$$

Then, the solved kinematic variable can be substitute into Eq. (3.14), and the lobe profile of the female rotor, $\mathbf{r}_2(\theta_1)$, can be obtained.

Rotors of the twin screw compressor have parallel axes and a constant axial lead. As soon as the cross-sectional profiles have been generated, the three-dimensional rotor surfaces can be further generated by rotation of the two-dimensional profiles about the individual rotor axis and axial translation of the profiles along the same axis simultaneously. The relation between the angular and linear motion is denoted by

$$z = \frac{L_w}{\tau_w}\tau \tag{3.19}$$

where L_w is the length or the rotor, τ_w is the wrap angle of the rotor, and τ is the twist angle of the rotor profile.

3.5 Design Examples

The capability of this proposed design approach is revealed by showing a variety of design examples in Figures 3.4 – 3.7. These designs are created by using a one-segment Bezier curve-based deviation function. The Bezier curve-based deviation functions are generated by four control points here. Bezier curves with more than four control points are also applicable to this approach and so are Bezier curves formed by more than one segment. More examples will be shown in the following chapter where the profile design

parameters and the optimization are taken into consideration. In those examples, the center to center distance, D_{cc}, is set to be the same value of 100 mm and the combinations of numbers of rotor lobes are 2/3, 3/4, 4/6, and 5/6 respectively. The control points to depict the deviation functions are tabulated and followed by the resulting figures.

Table 3.1: Control points for Figure 3.4

Figure 3.4	$\mathbf{P}_0$	$\mathbf{P}_1$	$\mathbf{P}_2$	$\mathbf{P}_3$
(a)	(0, -1)	(0.3, -10)	(2.44, 20)	(3.14, -1)
(b)	(0, -1)	(0.3, -10)	(1.84, 38)	(3.14, -1)
(c)	(0, -1)	(0.3, -10)	(1.34, 53)	(3.14, -1)
(d)	(0, -1)	(0.3, -10)	(0.94, 65)	(3.14, -1)

Table 3.2: Control points for Figure 3.5

Figure 3.5	$\mathbf{P}_0$	$\mathbf{P}_1$	$\mathbf{P}_2$	$\mathbf{P}_3$
(a)	(0, -1)	(0.3, -10)	(1.79, 8)	(2.09, -1)
(b)	(0, -1)	(0.3, -10)	(1.39, 20)	(2.09, -1)
(c)	(0, -1)	(0.3, -10)	(0.79, 38)	(2.09, -1)
(d)	(0, -1)	(0.3, -10)	(0.49, 47)	(2.09, -1)

Table 3.3: Control points for Figure 3.6

Figure 3.6	$\mathbf{P}_0$	$\mathbf{P}_1$	$\mathbf{P}_2$	$\mathbf{P}_3$
(a)	(0, -1)	(0.3, -10)	(1.27, 8)	(1.57, -1)
(b)	(0, -1)	(0.3, -10)	(0.97, 17)	(1.57, -1)
(c)	(0, -1)	(0.3, -10)	(0.57, 29)	(1.57, -1)
(d)	(0, -1)	(0.3, -10)	(0.39, 34)	(1.57, -1)

Table 3.4: Control points for Figure 3.7

Figure 3.7	$\mathbf{P}_0$	$\mathbf{P}_1$	$\mathbf{P}_2$	$\mathbf{P}_3$
(a)	(0, -1)	(0.3, -10)	(0.96, 8)	(1.25, -1)
(b)	(0, -1)	(0.3, -10)	(0.66, 17)	(1.25, -1)
(c)	(0, -1)	(0.3, -10)	(0.46, 23)	(1.25, -1)
(d)	(0, -1)	(0.3, -10)	(0.26, 29)	(1.25, -1)

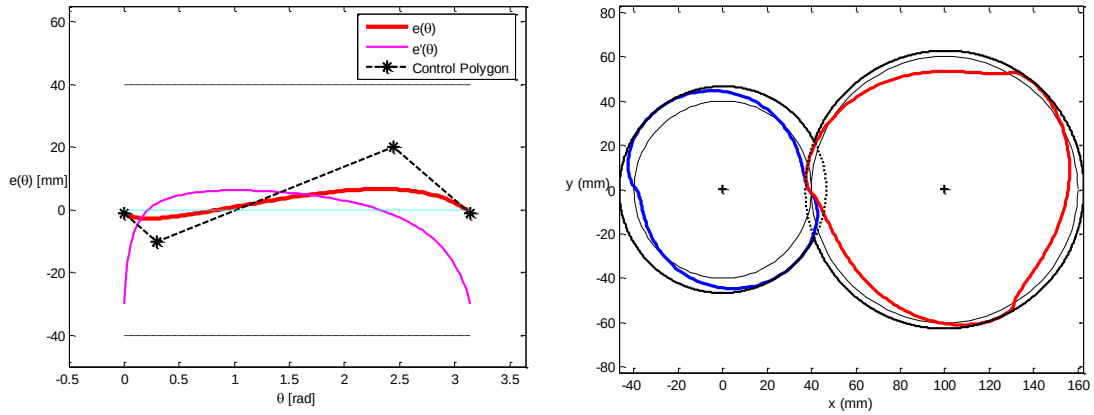

(a)

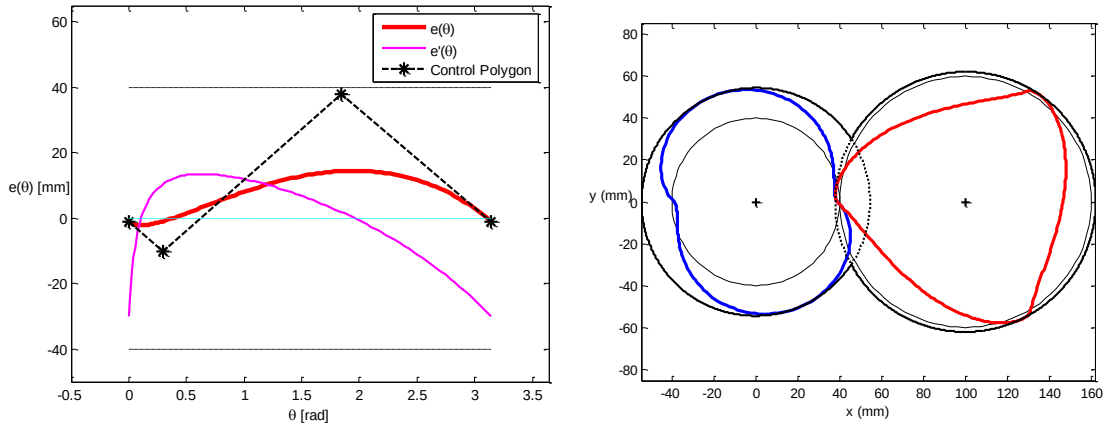

(b)

Figure 3.4: Designed rotor profiles of screw compressor with 2/3 configuration.

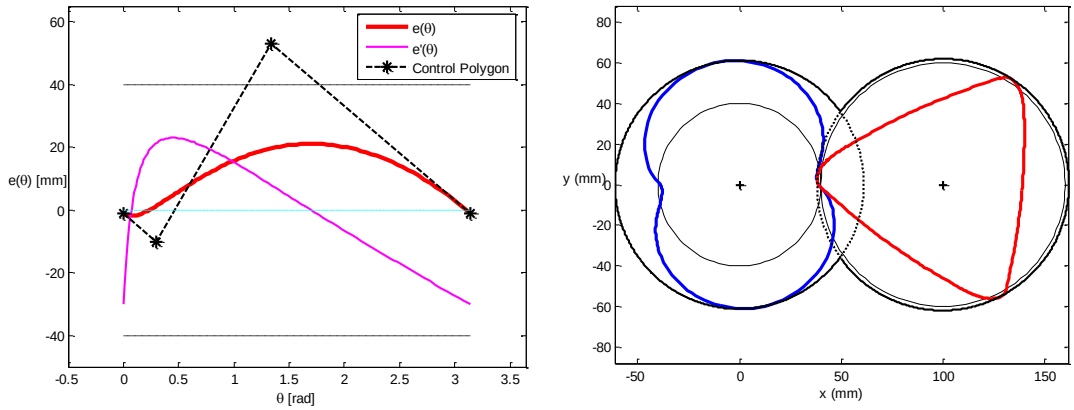

(c)

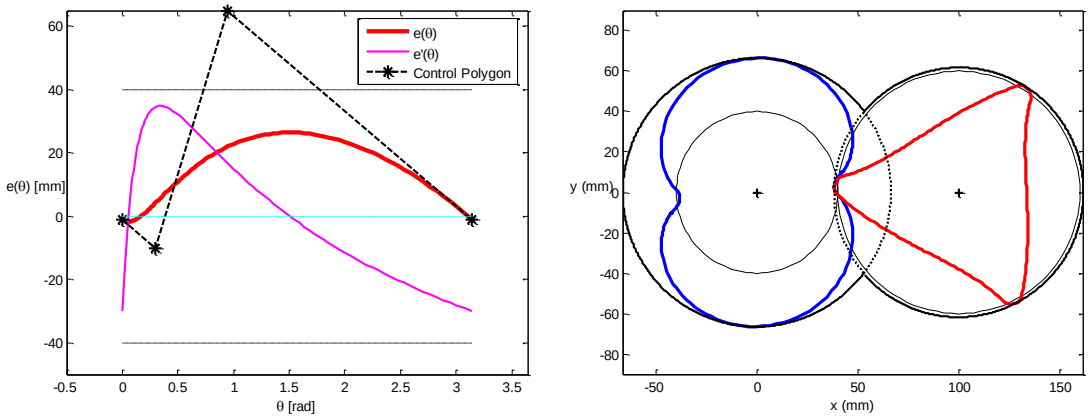

(d)

Figure 3.4: Designed rotor profiles of screw compressor with 2/3 configuration (Cont.).

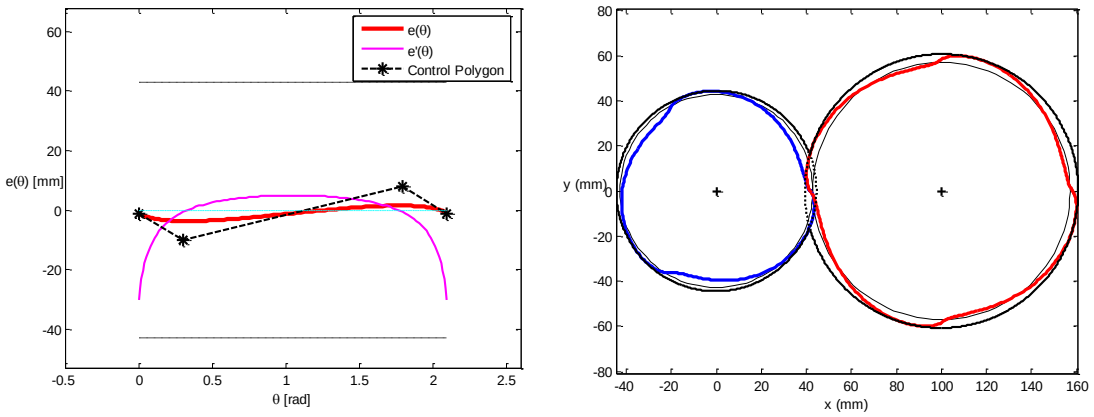

(a)

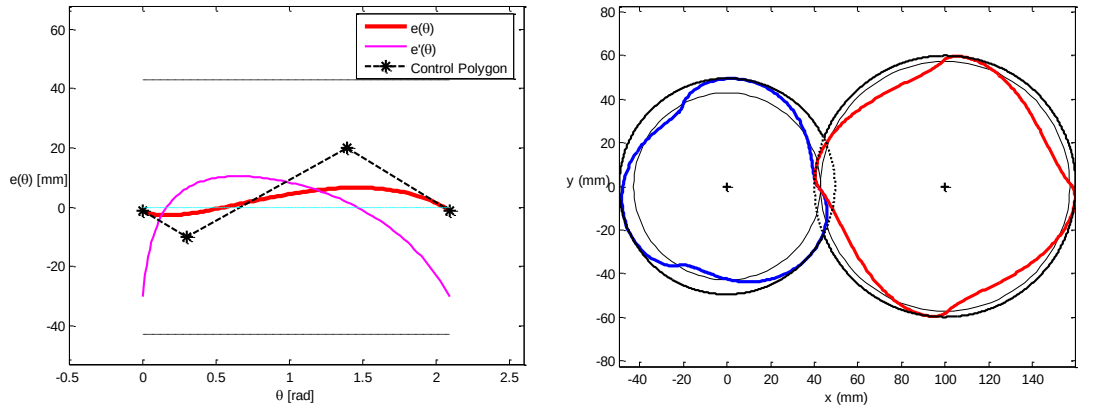

(b)

Figure 3.5: Designed rotor profiles of screw compressor with 3/4 configuration.

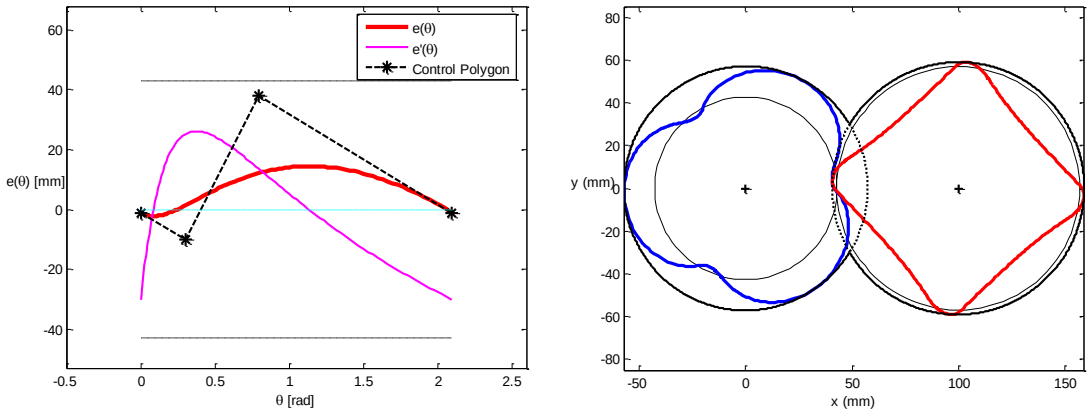

(c)

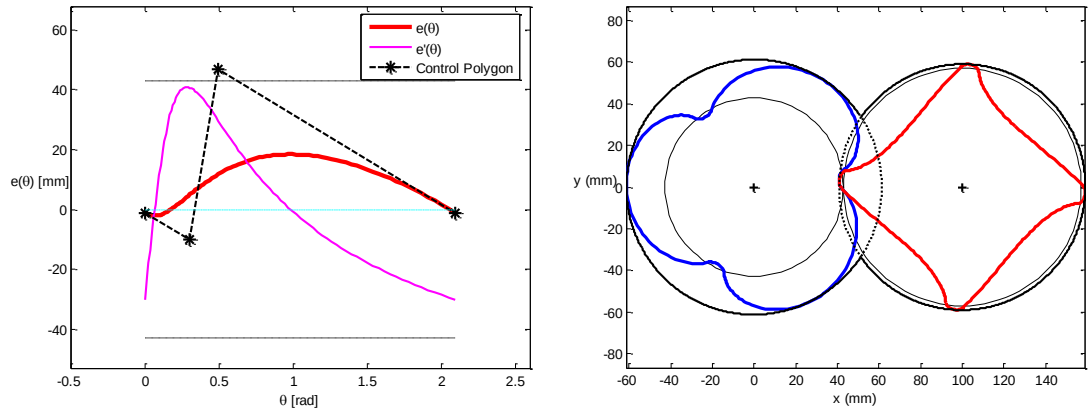

(d)

Figure 3.5: Designed rotor profiles of screw compressor with 3/4 configuration (Cont.).

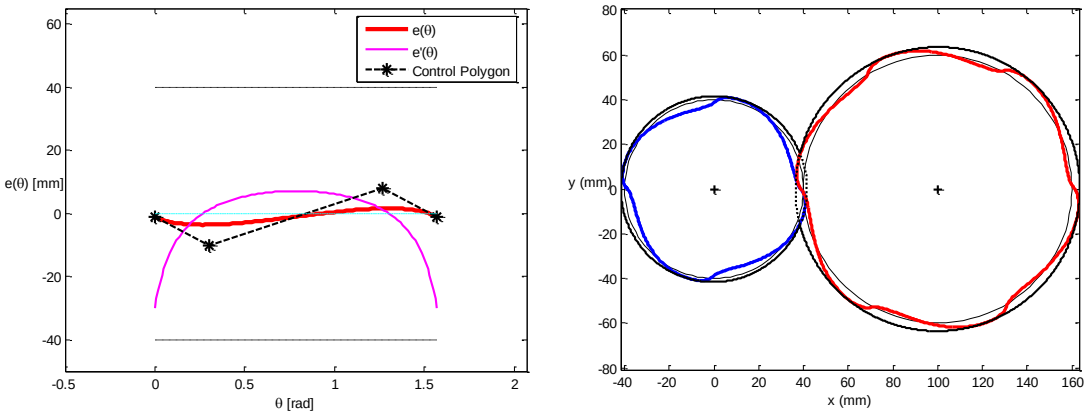

(a)

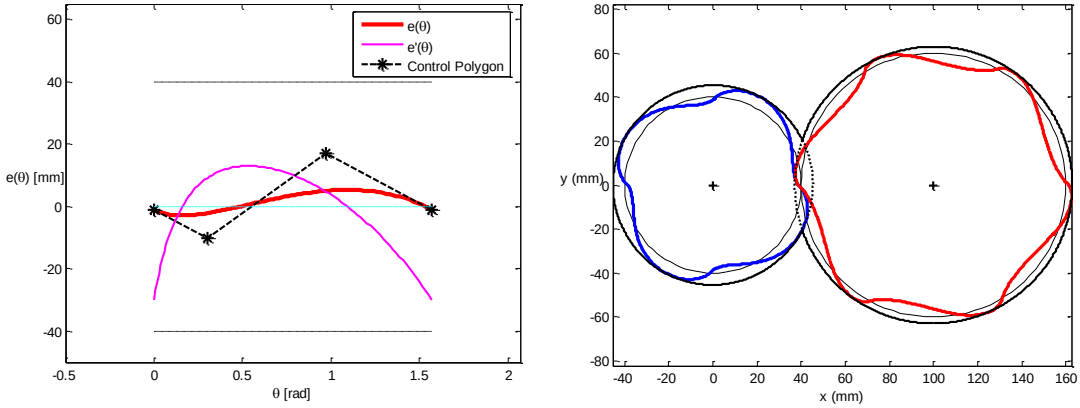

(b)

Figure 3.6: Designed rotor profiles of screw compressor with 4/6 configuration.

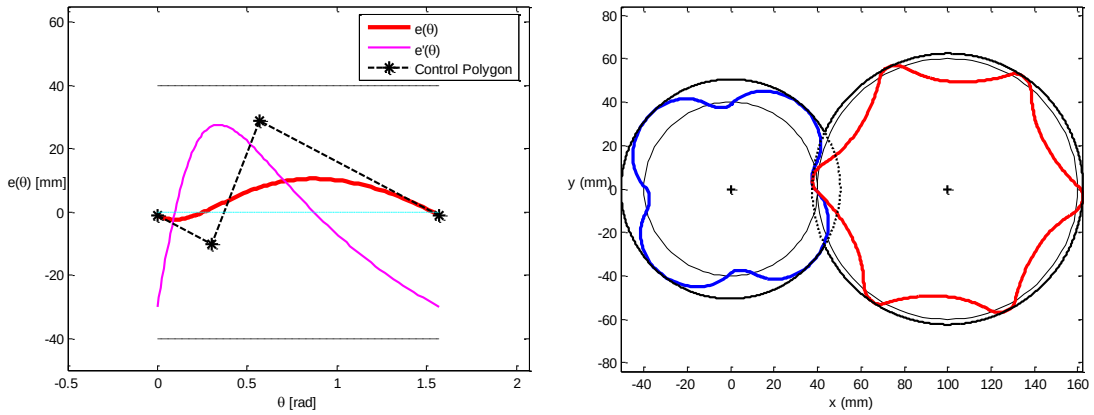

(c)

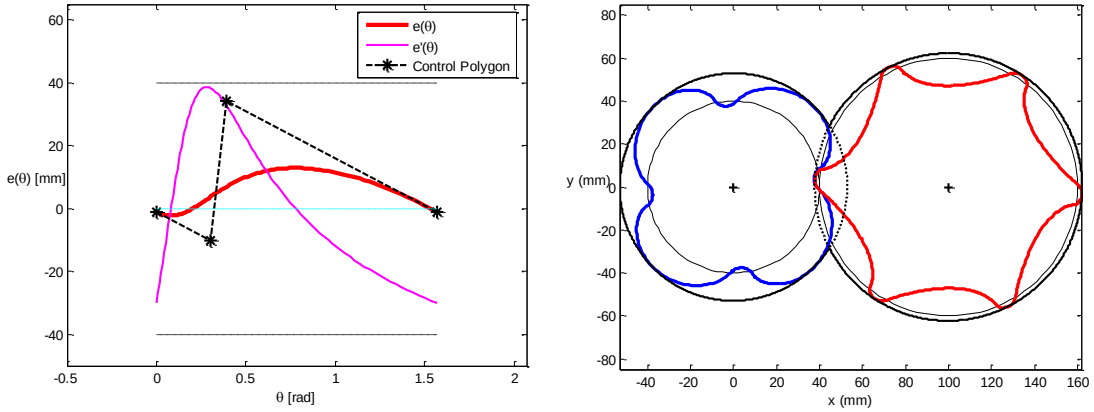

(d)

Figure 3.6: Designed rotor profiles of screw compressor with 4/6 configuration (Cont.).

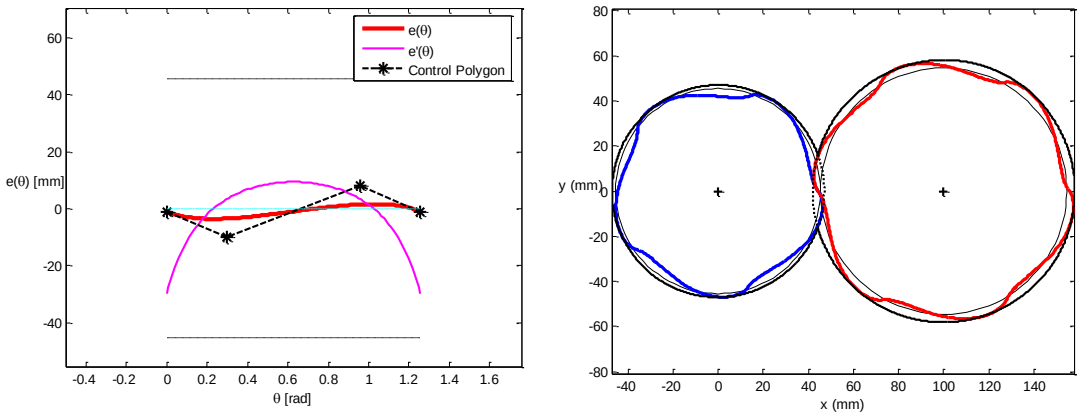

(a)

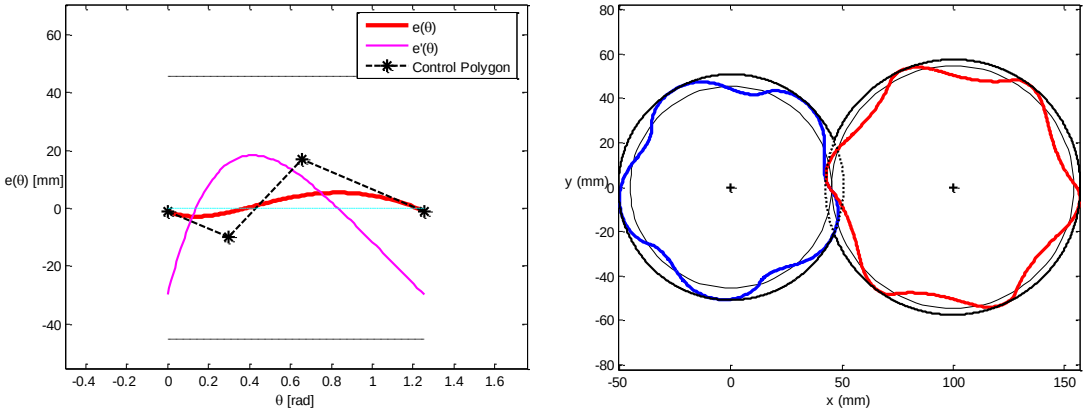

(b)

Figure 3.7: Designed rotor profiles of screw compressor with 5/6 configuration.

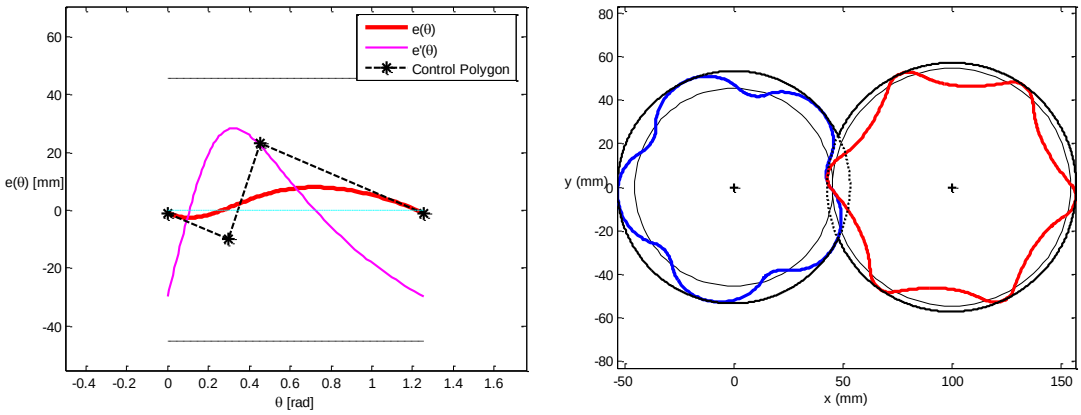

(c)

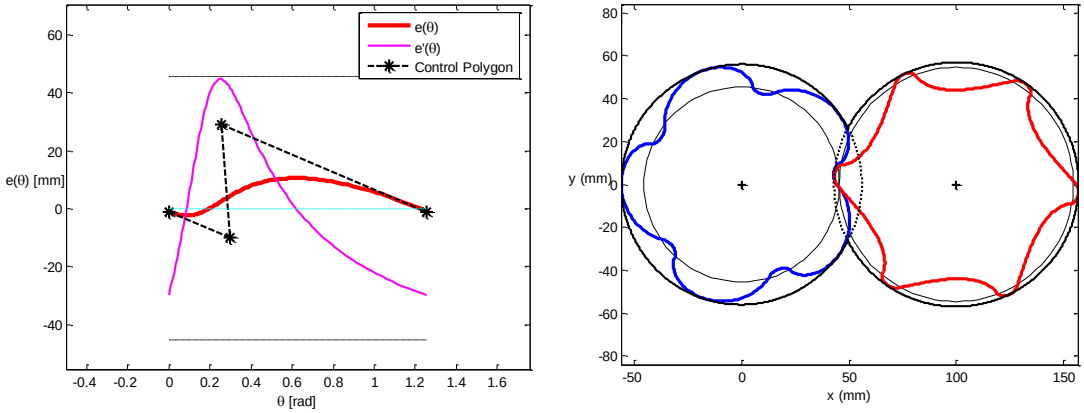

(d)

Figure 3.7: Designed rotor profiles of screw compressor with 5/6 configuration (Cont.).

Chapter 4

New Bezier Curve-Based Screw Compressor Profiles with Minimized Blow-holes

In this chapter, the design capability of the proposed design procedure is further discussed by designing more rotor profiles of screw compressor with a 2/3 configuration by using the one and two-segment third-order Bezier curves in Sections 4.2 and 4.3. This approach can be similarly applied to screw compressors with other configurations. From the results in these two sections, the partially overlapped three-segment three-order Bezier curve is proposed in Section 4.4 for designing the profiles of screw compressors with even better performance. In order to make fair comparisons between generated designs, the center distance between rotational axes is set to the same value of $D_{cc} = 100$ mm for different designs. Optimization is also performed in this chapter. The objective of optimization is mainly focused on minimizing blow-hole area. Other objectives, such as shorter sealing line length, can be added as constraints as the optimization techniques are applied. The optimal results are compared with the profiles of the twin screw compressors being utilized in the industry. From the conclusions of the com-

parison results, the method of profile design proposed in this chapter provides optimal results which is more universal than the traditional profile design methods.

4.1 Introduction

According to the literature review [59 - 71], it is found that the majority of the cross-sectional profiles of the existing twin screw compressors are comprised of multiple basic curves on the generating and generated profiles. Those generating curves are well-known curves, such as straight lines, circular arcs, parabolas, ellipses, hyperbolas, and trochoids. Although the combinations of those curves are unlimited and many screw compressors with profiles consisting of the combinations of multiple curves have served in industry successfully, the values of parameters for the original generating curves are difficult to determine and sometimes this task is accomplished by trial and error since all the generating and generated curves must be connected and in continuous tangency. In addition, when optimization needs to be performed for a profile of this kind, only its unique combination of generating curves are considered. To address this limitation, this study presents a detailed and theoretically grounded method for profile synthesis. In the process of generating the profiles for the screw compressor by using the proposed method, the Bezier curve-based deviation function is adopted to generate the profiles for male and female rotors. This makes it possible to create even more design possibilities than for different combinations of generating curves. Accordingly, the optimization results in this study are more universally applicable.

4.2 Designs by Using One-Segment Third-Order Bezier Curve-Based Deviation Functions

A one-segment third-order Bezier curve-based deviation function is a legitimate deviation function that satisfies all of the constraint equations, Eqs. 3.11a and 3.11b. Because of its order, $n=3$, it has four control points. These control points are defined by four parameters, $e_1(0), m, s_L$, and s_R, shown in Figure 4.1 and they are used to depict a Bezier-curve based deviation function compliant with the constraints. By adjusting the parameters, almost infinitely many deviation functions can be derived.

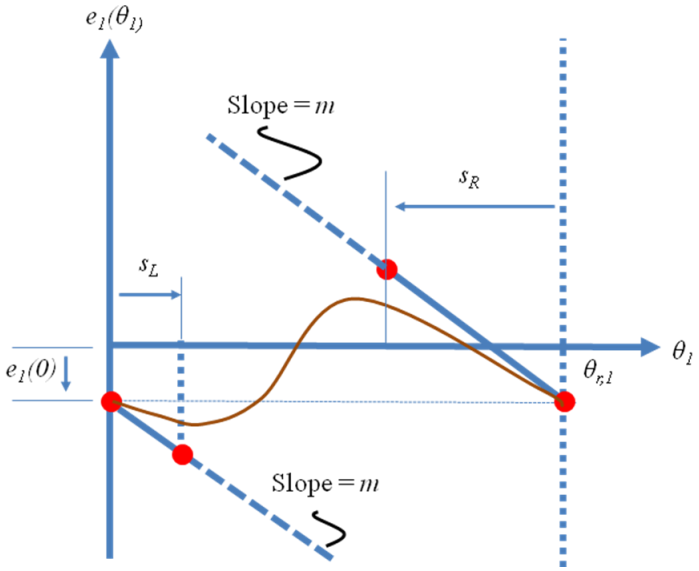

Figure 4.1: Parameters for determining the control points of the one-segment 3rd order Bezier curve-based deviation function

The whole curve changes by moving any control point, so local adjustment for this type of deviation function can't be made. By observing these deviation functions in Figure 4.2, it is found that as the maximum deviation increases, the minimum deviation increases, which means that the position of housing cusp relocates. Thus, although the lowest

point of the line of action goes down, it doesn't always result in the decrease of the distance between the line of action and the cusp of the housing. This distance is the height of the blowhole, H_{BH}, and is a factor to predict the size of blowhole without physically calculating the blowhole area [49]. It is also discovered that the larger the maximum and the minimum deviations are, the more pronounced the change of the slopes in the vicinity of the extreme values. In other words, the second derivative of the deviation function in the vicinity of the extreme value varies more dramatically. This observation is important because it is related to the curvature conformity at the rotor tip and bottom. Recall Eq. 3.12, the distance between a point on the rotor profile and the center of the rotor is

$$\begin{aligned} r_g &= x_1^2 + y_1^2 = (r_{p_1}\cos\theta_1 + e_1\cos\psi_1)^2 + (r_{p_1}\sin\theta_1 + e_1\sin\psi_1)^2 \\ &= r_{p_1}^2 + e_1^2 + 2r_{p_1}e_1\cos(\theta_1 - \psi_1) \end{aligned} \tag{4.1}$$

The extreme value of r_g occurs at $\theta_1 - \psi_1 = 0$ or $\theta_1 - \psi_1 = \pi$. From Eq. 4.1, it implies that $e_1' = 0$. As a result, the extreme values of the deviation function always generate the tip and the bottom of a rotor profile. The second derivative of the deviation function near the top and bottom affects the curvature conformity directly. If the curvature change near the top and bottom of a rotor robe is greater, the curvature conformity decreases. Through those effects, it can be seen that this type of deviation is legitimate, but lacks controllability of the design results. However, it still provides us with a valuable guideline of how the deviation function affects the design results. With the observation of the behaviors of the deviation function at the extreme points and its vicinity, it is reasonable to derive the deviation function by using a Bezier curve comprised of two segments whose

boundary values are the extreme values of the function. Bezier curve-based deviation functions which have the same maximum and the same minimum can be used to generate rotors which have the same addendum and dedendum radii, and thus to fix the size of rotors.

Table 4.1: Parameters for Figure 4.2

Figure 4.2	$e_1(0)$ (mm)	m (mm/rad)	s_L (mm)	s_R (mm)	H_{BH} (mm)
(a)	1.0	-35.0	0.3	1.3	29.25
(b)	1.0	-35.0	0.3	1.8	30.74
(c)	1.0	-35.0	0.3	2.1	29.65

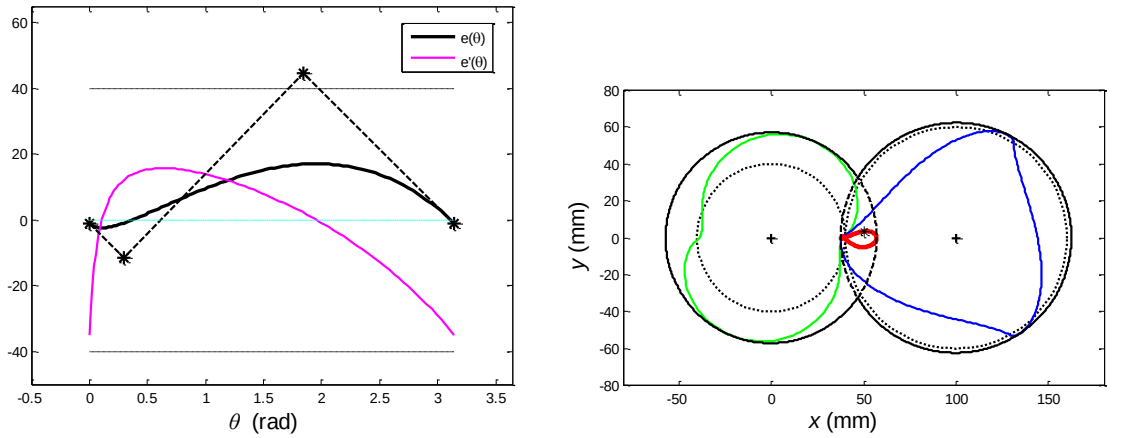

(a)

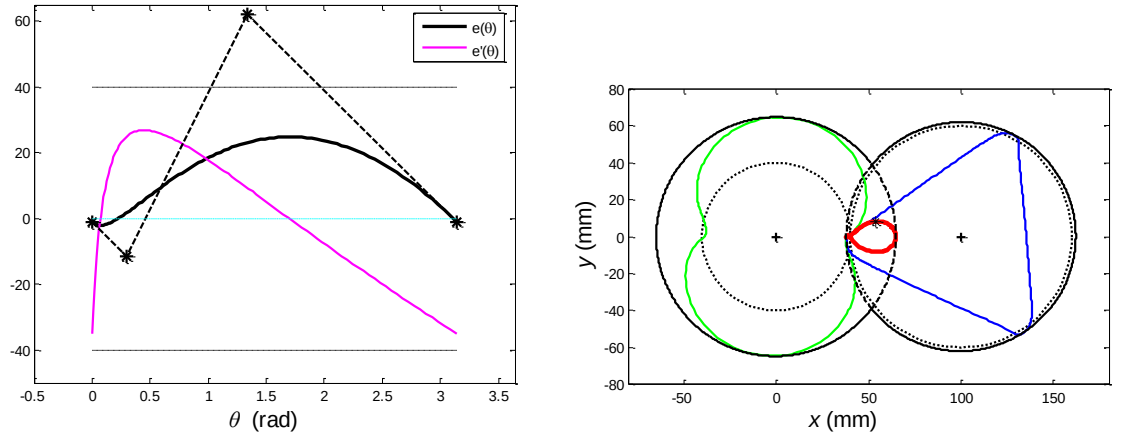

(b)

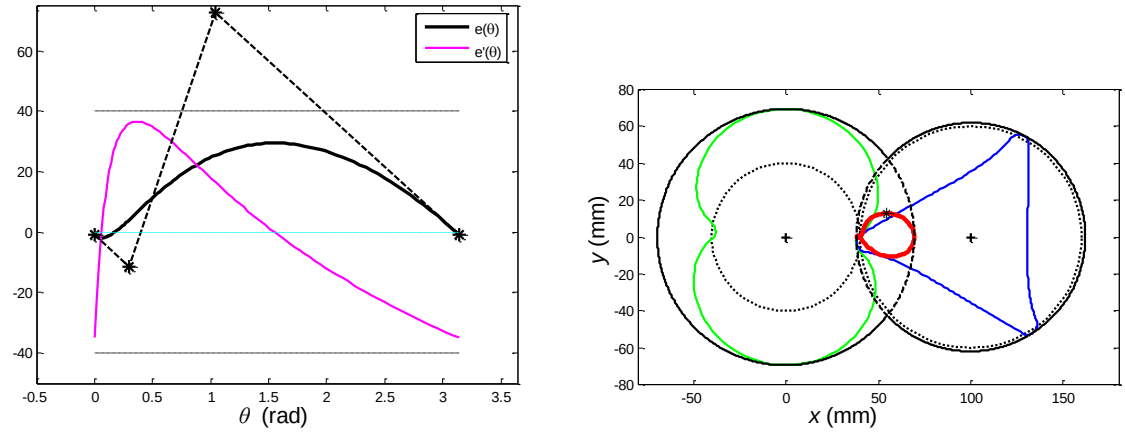

(c)

Figure 4.2: Design examples by using the one-segment third-order Bezier curve-based deviation functions.

4.3 Designs by Using Two-Segment Third-Order Bezier Curve-Based Deviation Functions

A two-segment third-order Bezier curve-based deviation function is also a legitimate deviation function which satisfies the constraint equations. It has seven control points. These control points are defined by seven parameters, shown in Figure 4.3. By adjusting the parameters, a variety of deviation functions can be acquired.

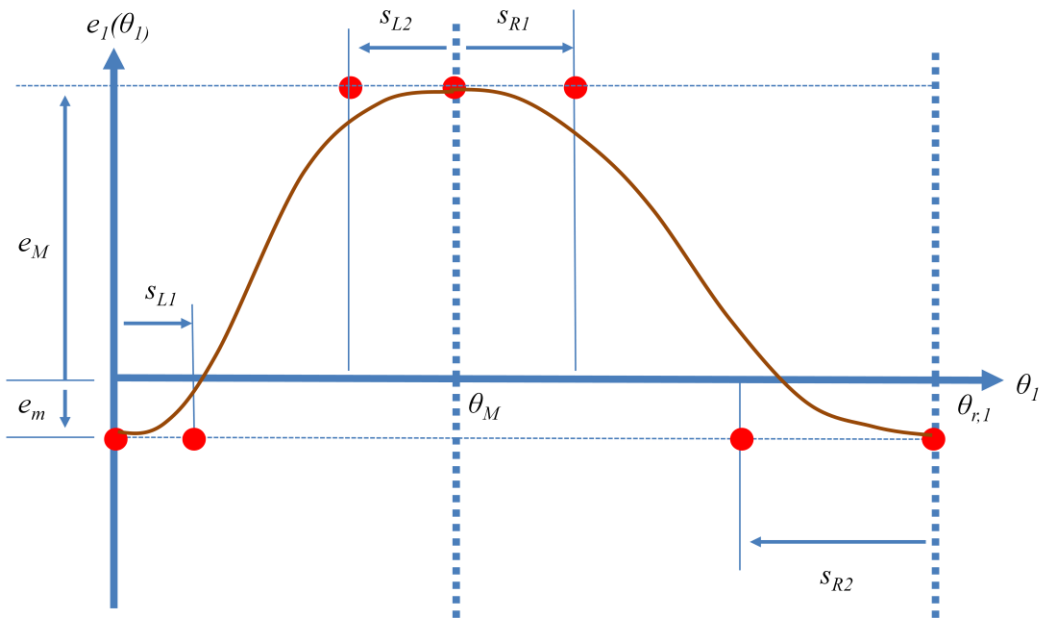

Figure 4.3: Parameters for determining the control points of the two-segment third-order Bezier curve-based deviation function.

In order to obtain rotors with the same addendum radii and the same dedendum radii for fair comparison, fixed maximum deviation, e_M , and minimum deviation, e_m should be chosen. Starting from $\theta_M = \theta_{r,1}/2 = \pi/(2N_1)$ and the same step size s_{L1} , s_{L2} , s_{R1} , and s_{R2} , a symmetric deviation function is derived, and thus a symmetric lobe profile is ob-

tained in Figure 4.4. When θ_M moves to the left, the line of action gets closer to the cusp of the housing, and hence, the height of the blowhole, H_{BH}, reduces. The step sizes, s_{L1}, and s_{L2}, affect the conformities at the tips of rotors, as do step sizes, s_{R1}, and s_{R2}. However, a larger s_{L2} reduces the height of the blowhole, but a larger s_{L1} decreases it. So it would be better to adjust s_{L1} and s_{R2} for higher conformity at the rotor bottom and less height of the blowhole. Similarly, better conformity at the tip of the rotor can be achieved by adjusting s_{R1} while keeping s_{L2} small at the same time. One of the optimal results is shown in Figure 4.5. Although higher conformity improves the sealing between the rotor tip and the housing, it has a detrimental effect on the flow rate. As seen in Figure 4.6, with higher conformity, the area accommodating the fluid is smaller because the lobe becomes wider.

Table 4.2: Parameters for Figure 4.4

Figure 4.4	e_m	e_M	θ_M	s_{L1}	s_{L2}	s_{R1}	s_{R2}	H_{BH}
(a)	1.0	30.0	1.17	0.1	0.1	0.1	0.1	29.94
(b)	1.0	30.0	1.37	0.1	0.1	0.1	0.1	27.81
(c)	1.0	30.0	1.57	0.1	0.1	0.1	0.1	24.94

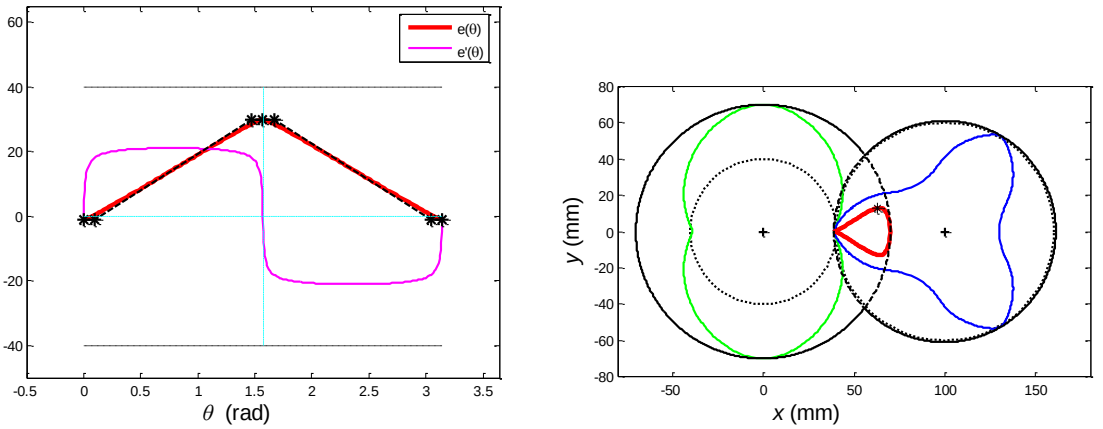

(a)

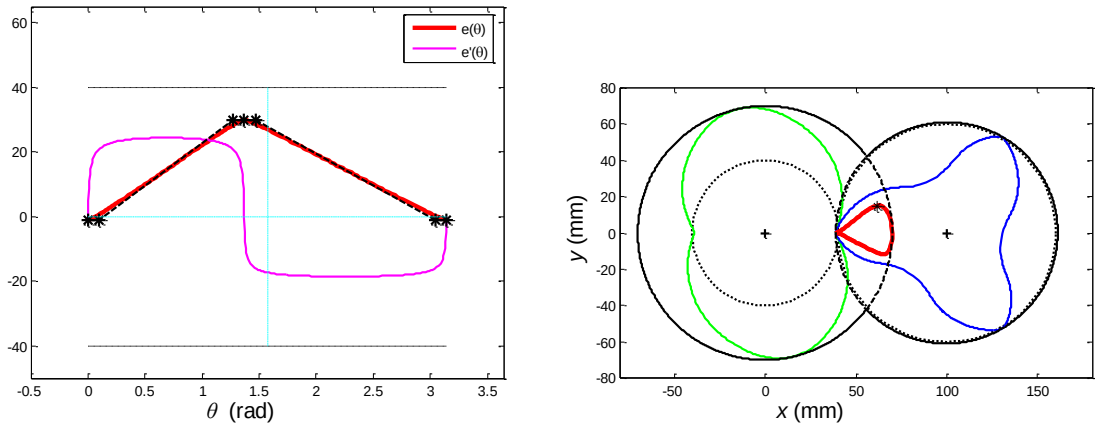

(b)

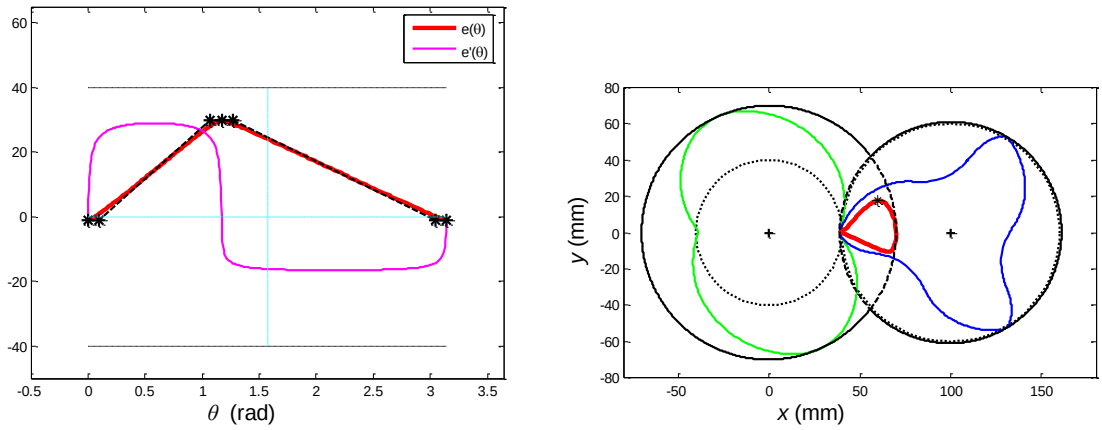

(c)

Figure 4.4: Design examples by using the two-segment third-order Bezier curve-based deviation functions with different θ_M .

Table 4.3: Parameters for Figure 4.5 and Figure 4.6

Figure No.	e_m	e_M	θ_M	s_{L1}	s_{L2}	s_{R1}	s_{R2}	H_{BH}
Figure 4.5	1.0	30.0	1.17	0.45	0.1	0.4	0.4	18.63
Figure 4.6	1.0	30.0	1.17	0.1	0.1	0.8	0.8	18.63

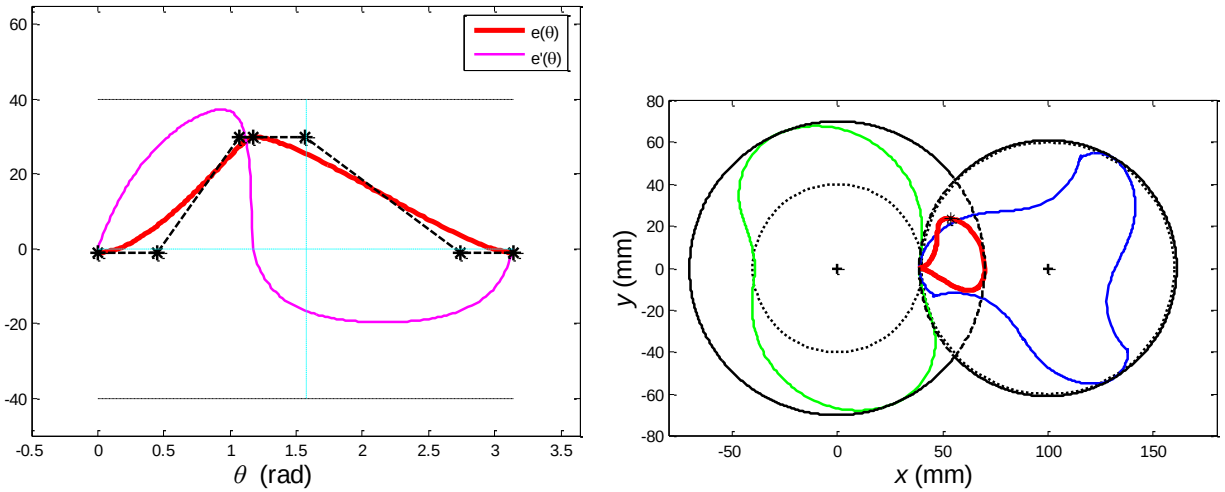

Figure 4.5: A design result with shorter heigth of blowhole by using the two-segment third-order Bezier curve-based deviation function.

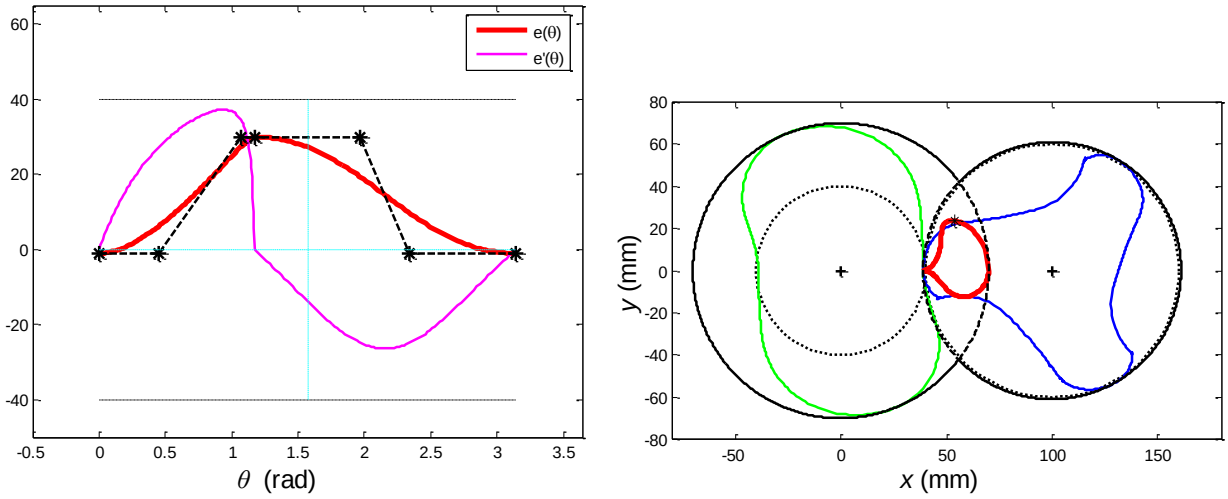

Figure 4.6: A design example with higher conformity.

The design approach discussed so far in this section provides a logical and intuitive sense to search for better rotor profiles with shorter height of the blowhole, which is an indicator of the size of blowhole area, and higher conformity. However, there are limitations for the resulting values of height of the blowhole. Although the height decreases, the point on the line of action which has the shortest distance to the housing cusp is always inside a circle centered at the pitch point with the radius of maximum deviation, as seen in Figure 4.7. This issue can be solved by using the three-segment deviation function that partially overlaps. This type of deviation function is discussed in the following section.

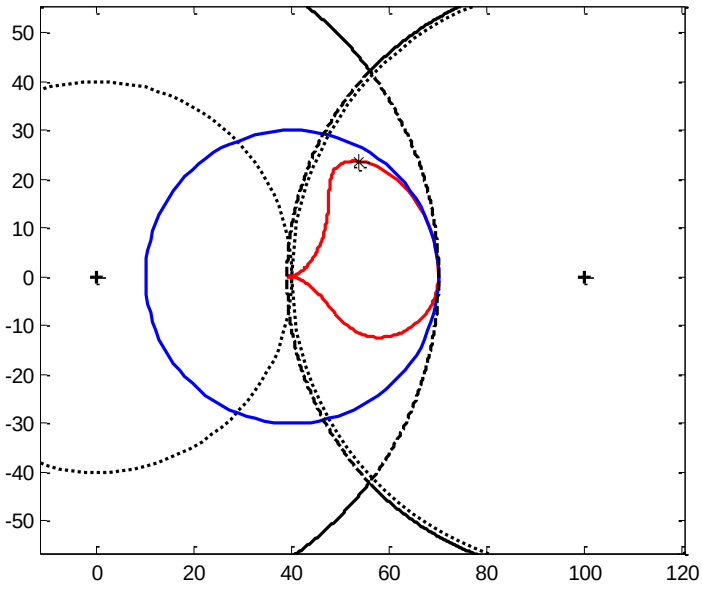

Figure 4.7: Bound of the line of action.

4.4 Designs by Using Partially Overlapped Three-Segment Third-Order Bezier Curve-Based Deviation Functions

4.4.1 Partially overlapped three-segment deviation function

In order to improve the controllability and outcome of the screw compressor profile design methodology, the three-segment deviation function is proposed and shown in Figure 4.8. Each segment has four control points and those points are determined by the parameters, e_{bot}, e_{tip}, e_M, $\theta_{r,1}$, θ_R, θ_M, θ_L, s_{R1}, s_{R2}, s_{L1}, s_{L2}, s_{M1}, s_{M2}, and m. The reasons why this type of deviation function is used are addressed as follows. The point on the line of action which is closest to the housing cusp is generated by the left segment of the deviation function. The right segment of the deviation function is utilized to size the diameters of the rotors. Thus, the author modified the left segment of the deviation function to bring the line of action closer to the housing cusp. The only way to break through the limitation discussed in the last section is to increase the deviation along this segment to a value greater than e_{tip}. However, by doing so, the only way to maintain C^1 continuity at the joints between segments of the deviation function is to make the function composed of at least three segments which are partially overlapped. One important thing should be specifically mentioned here. That is the deviation function starts from e_{bot} on the left segment and monotonically increases to e_M, and there exists no such point where it is the maximum extreme value in this segment and its first derivative

equals zero. The reason being, if it exists, the rotor profile will have another tip which is physically impossible. Since the C^1 continuity condition must hold at each coincident point between segments of deviation function, the whole three-segment deviation function that partially overlaps looks generally in the formation shown in Figure 4.8. The overlap means that in between the interval of overlap the rotors are in contact at two or three points. A design example with a 5/6 configuration is shown in Figure 4.9 and the tip of the line of action breaks through the bounding circle as shown in Figure 4.10. This design procedure can be applied to other configurations.

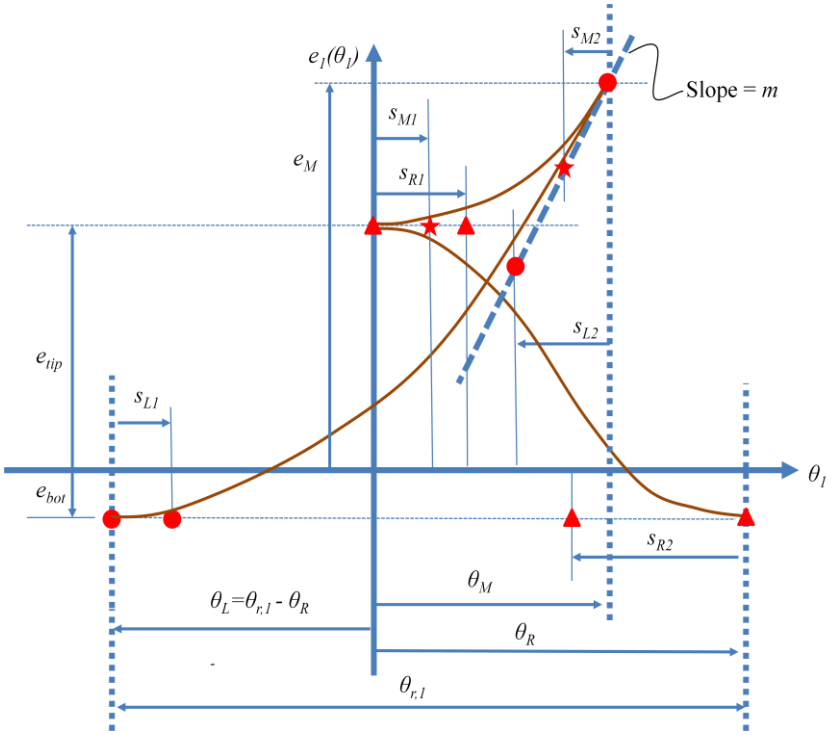

Figure 4.8: Parameters for determining the control points of the partially overlapped three-segment third-order Bezier curve-based deviation function.

Table 4.4: Parameters for Figure 4.9

e_{bot} (mm)	e_{tip} (mm)	e_M (mm)	$\theta_{r,1}$ (rad)	θ_R (rad)	θ_M (rad)	θ_L (rad)
4.55	22.73	30.54	1.26	0.75	0.30	0.50

s_{R1} (mm)	s_{R2} (mm)	s_{L1} (mm)	s_{L2} (mm)	s_{M1} (mm)	s_{M2} (mm)	m (mm/rad)	H_{BH} (mm)
0.11	0.15	0.01	0.27	0.06	0.17	41.96	16.83

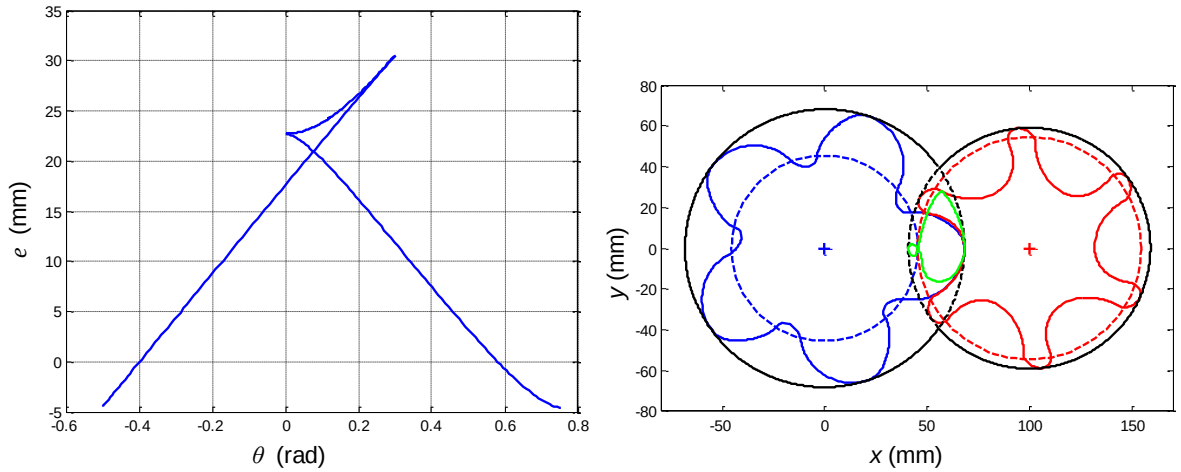

Figure 4.9: A design example with a 5/6 configuration by using a partially overlapped three-segment third-order Bezier curve-based deviation function.

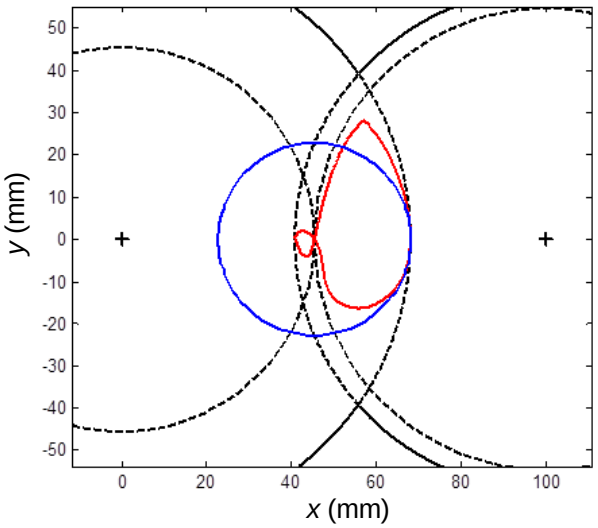

Figure 4.10: Break through the boundary.

Table 4.5: Combination of curves of Hitachi profile

Male		Female	
Segment	Curve Type	Segment	Curve Type
HI	Circle Conjugate	*AB*	Circle
IJ	Circle Conjugate	*BC*	Circle
JK	Circle	*CD*	Circle
KL	Circle	*DE*	Circle Conjugate
LM	Circle Conjugate	*EF*	Circle
MN	Circle	*FG*	Circle

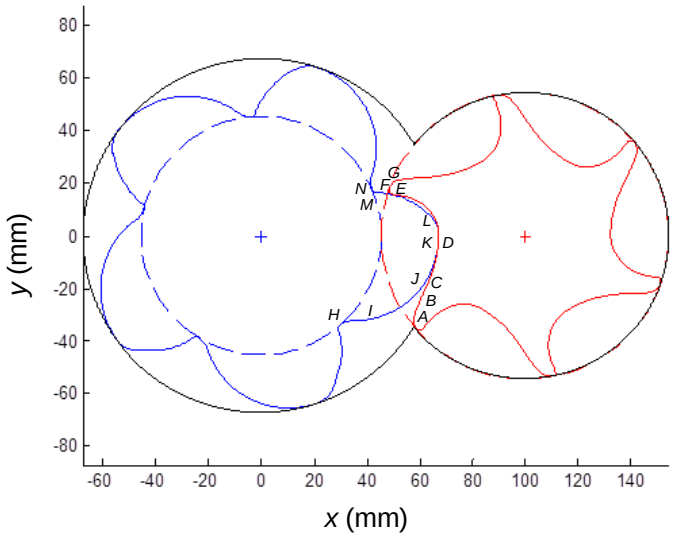

Figure 4.11: Hitachi profile.

Table 4.6: Combination of curves of GHH profile.

Male		Female	
Segment	Curve Type	Segment	Curve Type
GH	Ellipse Conjugate	*AB*	Ellipse
HJ	Circle	*BD*	Circle
J	Point	*DE*	Cycloid
JK	Cycloid	*E*	Point
KL	Circle	*EF*	Circle

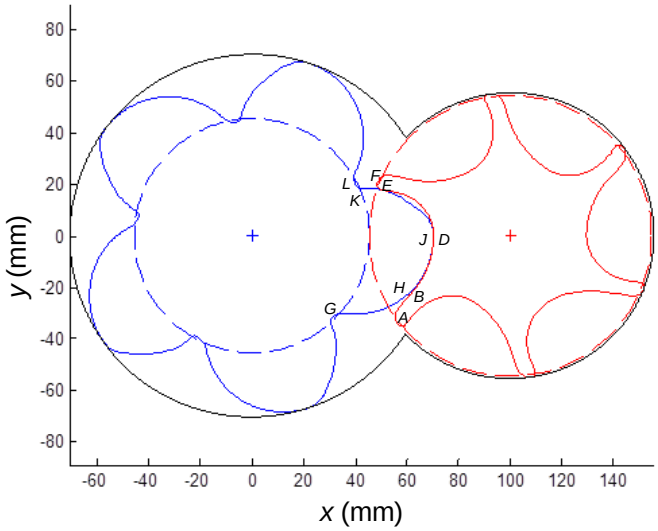

Figure 4.12: GHH profile.

Table 4.7: Combination of curves of Fu Sheng profile

Male		Female	
Segment	Curve Type	Segment	Curve Type
FG	Circle	*AB*	Circle Conjugate
GH	Ellipse	*BC*	Ellipse Conjugate
HI	Circle	*CD*	Circle Conjugate
IJ	Circle Conjugate	*DE*	Circle

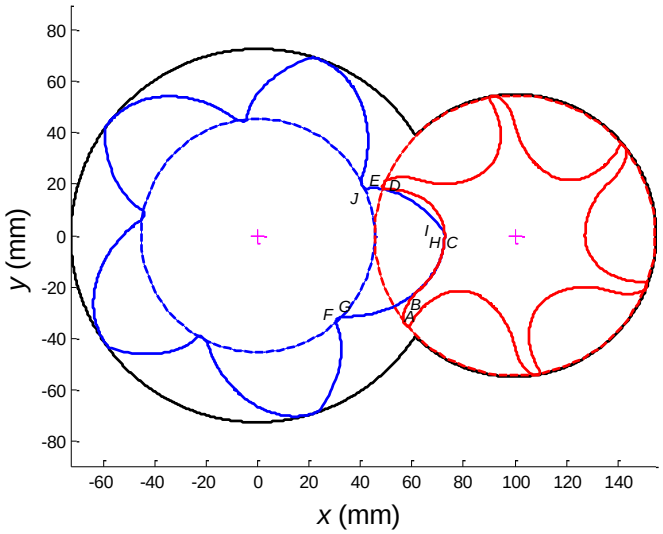

Figure 4.13: Fu Sheng profile.

4.4.2 Optimization for Existing Profiles

Three profiles of the twin screw compressors in industry including Hitachi [70], GHH [69, 72], and Fu Sheng [71] profiles are shown in Figures 4.11 - 4.13. They are chosen as the comparative examples. In order to make fair comparisons, new designs with the same rotor size are created. This can be achieved by determining e_{tip} and e_{bot} from the addendum and dedendum radii, r_{a1} and r_{d1}, of the original male rotors. The relationships are depicted by

$$e_{bot} = r_{p1} - r_{d1} \tag{4.2}$$

and

$$e_{tip} = r_{a1} - r_{p1} \tag{4.3}$$

These deviations will be applied to the new profile designs and thus the size of the new rotors will be the same as that of the original ones. $\theta_{r,1}$ is the angle span for a complete lobe of the rotor and it depends on the number of rotor lobes. $\theta_{r,1}$, θ_R , and θ_L are dependent variables and the relationship is

$$\theta_{r,1} = \theta_R + \theta_L \tag{4.4}$$

Accordingly, at the beginning of the design procedure, the adjustable parameters are e_M , θ_R (or θ_L), θ_M , s_{R1}, s_{R2}, s_{L1}, s_{L2}, s_{M1}, s_{M2}, and m. In this study the optimization technique, Augmented Lagrange Multiplier Method [73], is applied. The main goal of the optimization is to reduce the blowhole area. The objective function is formulated as follows:

$$Min.\quad f(\mathbf{X}) = A_{BH}(e_m, \theta_R, \theta_M, s_{R1}, s_{R2}, s_{L1}, s_{L2}, s_{M1}, s_{M2}, m)\,. \tag{4.5}$$

Constraints for the parameters and optimization are

$$-r_{p_1} \le e_1' \le r_{p_1} \tag{4.6a}$$

$$\theta_M \le \theta_R \le \theta_{r,1} \tag{4.6b}$$

$$\theta_R \le s_{R1}, s_{R2} \le 0 \tag{4.6c}$$

$$\theta_L \le s_{L1}, s_{L2} \le 0 \tag{4.6d}$$

$$\theta_M \le s_{M1}, s_{M2} \le 0\,. \tag{4.6e}$$

The design results are shown in comparison with the original profiles in Figures 4.14 - 4.16. The resulting blowhole areas and sealing line lengths are calculated and tabulated in Tables 4.9, 4.11, and 4.13. The new profiles are named by codes. For example, the code, DFM-H1, means the first new design for the Hitachi profile (H1) by using deviation function method (DFM). Similarly, the names for the other two new designs are DFM-G1 and DFM-F1.

Table 4.8: Parameters for DFM-H1

e_{bot} (mm)	e_{tip} (mm)	e_M (mm)	$\theta_{r,1}$ (rad)	θ_R (rad)	θ_M (rad)	θ_L (rad)
0.00	22.00	35.80	1.25	0.93	0.50	0.32

s_{R1} (mm)	s_{R2} (mm)	s_{L1} (mm)	s_{L2} (mm)	s_{M1} (mm)	s_{M2} (mm)	m (mm/rad)
0.28	0.09	0.01	0.32	0.05	0.32	42.67

Table 4.9: Results for Figure 4.14

Hitachi	Original	DFM-H1	Difference
Sealing Line Length (mm)	113.86	158.55	+39.25%
Blowhole Area (mm^2)	12.94	2.30	-82.23%

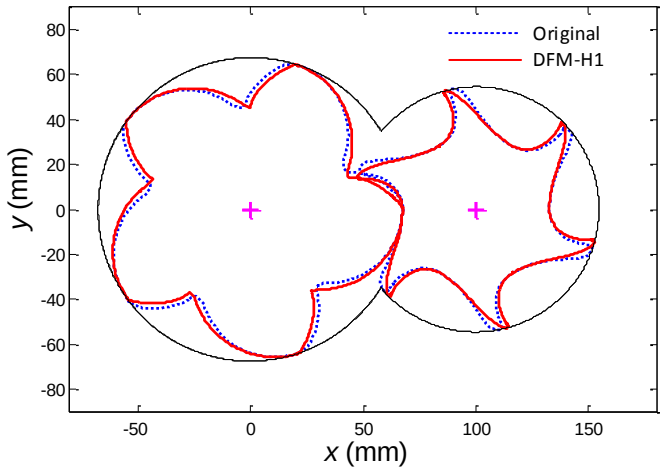

Figure 4.14: Minimized blowhole area for Hitachi profile.

Table 4.10: Parameters for DFM-G1

e_{bot} (mm)	e_{tip} (mm)	e_M (mm)	$\theta_{r,1}$ (rad)	θ_R (rad)	θ_M (rad)	θ_L (rad)
1.00	25.00	39.38	1.25	0.82	0.50	0.42

s_{R1} (mm)	s_{R2} (mm)	s_{L1} (mm)	s_{L2} (mm)	s_{M1} (mm)	s_{M2} (mm)	m (mm/rad)
0.16	0.08	0.0042	0.32	0.05	0.32	42.38

Table 4.11: Results for Figure 4.15

GHH	Original	DFM-G1	Difference
Sealing Line Length (mm)	139.47	145.96	+4.65%
Blowhole Area (mm^2)	1.39	1.15	-17.27%

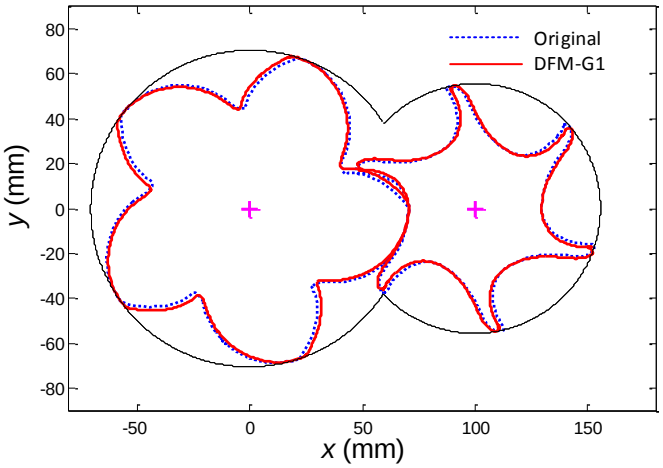

Figure 4.15: Minimized blowhole area for GHH profile

Table 4.12: Parameters for DFM-F1

e_{bot} (mm)	e_{tip} (mm)	e_M (mm)	$\theta_{r,1}$ (rad)	θ_R (rad)	θ_M (rad)	θ_L (rad)
0.48	27.25	41.12	1.25	0.84	0.53	0.41

s_{R1} (mm)	s_{R2} (mm)	s_{L1} (mm)	s_{L2} (mm)	s_{M1} (mm)	s_{M2} (mm)	m (mm/rad)
0.08	0.17	0.0011	0.28	0.16	0.22	41.84

Table 4.13: Results for Figure 4.16

Fu Sheng	Original	Optimal	DFM-F1	Difference
Sealing Line Length (mm)	139.63	146.84	150.13	+2.24%
Blowhole Area (mm^2)	6.64	2.63	1.22	-53.61%

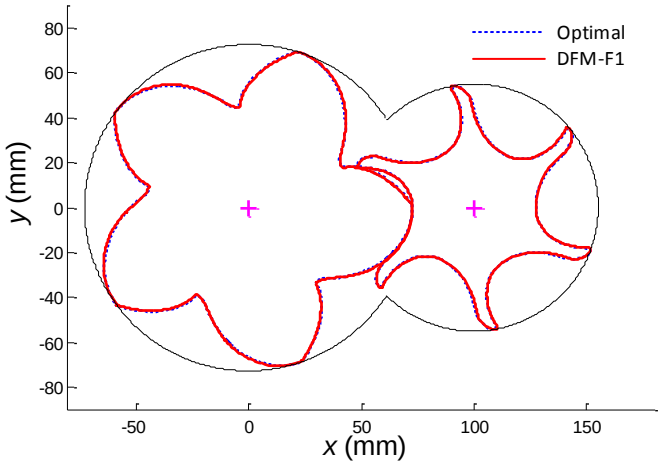

Figure 4.16: Minimized blowhole area for Fu Sheng profile.

From the results, they all imply that the interlobe sealing line length increases with the reduction of the blowhole area. In the case where the increment of interlobe sealing line length should be limited, the length increment can be bound, and this condition serves as an extra inequality constraint when the optimization is performed. Take the Hitachi profile as an example. The interlobe sealing line length is constrained to be less than

125 mm which is about 10% increment of the length of original design. This constraint is added to the optimization process and the result is shown in Figures 4.17 - 4.19. The blowhole area and sealing line length are computed and tabulated in Table 4.15. It shows that the blowhole area still decreases by 42.58%.

Table 4.14: Parameters for DFM-H2

e_{bot} (mm)	e_{tip} (mm)	e_M (mm)	$\theta_{r,1}$ (rad)	θ_R (rad)	θ_M (rad)	θ_L (rad)
0.00	22.00	32.80	1.25	0.93	0.42	0.32

s_{R1} (mm)	s_{R2} (mm)	s_{L1} (mm)	s_{L2} (mm)	s_{M1} (mm)	s_{M2} (mm)	m (mm/rad)
0.28	0.28	0.0032	0.27	0.04	0.23	42.67

Table 4.15: Results for Figure 4.17

Hitachi	Original	DFM-H2	Difference
Sealing Line Length (mm)	113.86	124.63	+9.47%
Blowhole Area (mm^2)	12.94	7.4258	-42.58%

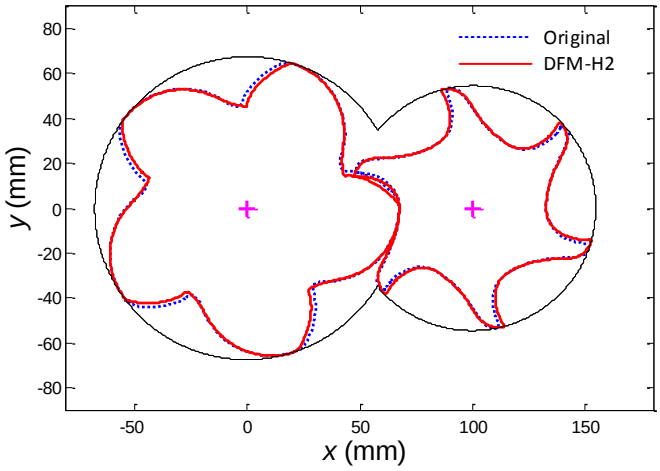

Figure 4.17: Minimized blowhole area ($\Delta l_s \leq 10\%$) for Hitachi profile.

Table 4.16: Parameters for DFM-G2

e_{bot} (mm)	e_{tip} (mm)	e_M (mm)	$\theta_{r,1}$ (rad)	θ_R (rad)	θ_M (rad)	θ_L (rad)
1.00	25.00	38.25	1.25	0.80	0.46	0.45

s_{R1} (mm)	s_{R2} (mm)	s_{L1} (mm)	s_{L2} (mm)	s_{M1} (mm)	s_{M2} (mm)	m (mm/rad)
0.29	0.08	0.0042	0.39	0.04	0.27	42.33

Table 4.17: Results for Figure 4.18

GHH	Original	DFM-G2	Difference
Sealing Line Length (mm)	139.47	143.10	+2.60%
Blowhole Area (mm^2)	1.39	1.24	-10.79%

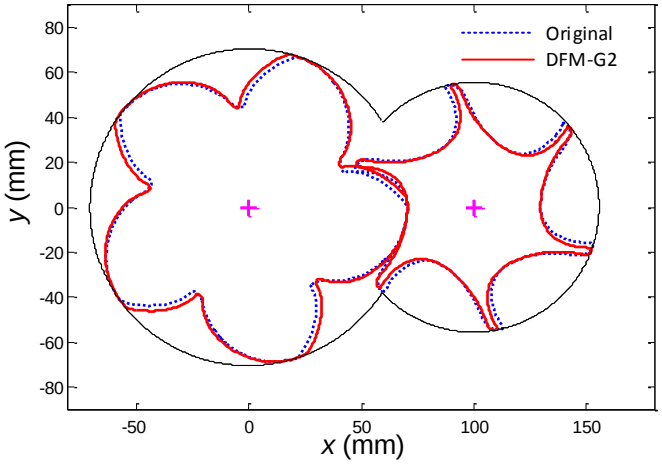

Figure 4.18: Minimized blowhole area ($\Delta l_s \leq 3\%$) for GHH profile

When this approach is applied to the GHH and Fu Sheng profiles, the length increments are set to be less than 3% and 1%, respectively. The results reveal that the physical numbers of the blowhole areas don't seem to vary significantly; however, the percent-

ages of reduction are at least 10% for both optimized profiles as can be seen in Tables 4.17 and 4.19.

Table 4.18: Parameters for DFM-F2

e_{bot} (mm)	e_{tip} (mm)	e_M (mm)	$\theta_{r,1}$ (rad)	θ_R (rad)	θ_M (rad)	θ_L (rad)
0.48675	27.255	41.07	1.25	0.86	0.50	0.39

s_{R1} (mm)	s_{R2} (mm)	s_{L1} (mm)	s_{L2} (mm)	s_{M1} (mm)	s_{M2} (mm)	m (mm/rad)
0.16	0.14	0.0023	0.31	0.17	0.19	41.87

Table 4.19: Results for Figure 4.19

Fu Sheng	Original	Optimal	DFM-F2	Difference
Sealing Line Length (mm)	139.63	146.84	148.17	+0.91%
Blowhole Area (mm^2)	6.64	2.63	1.79	-31.94%

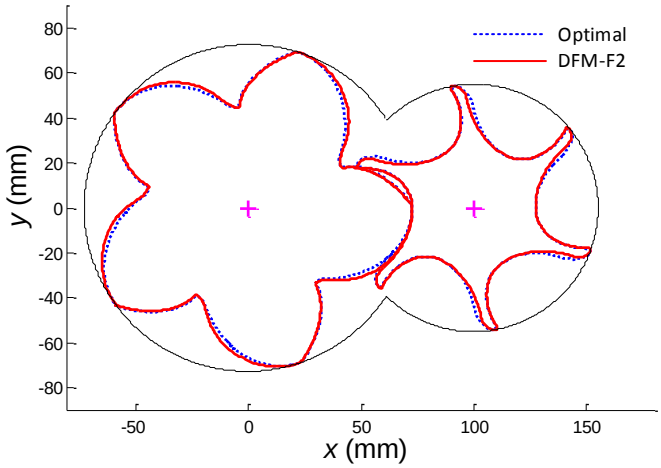

Figure 4.19: Minimized blowhole area ($\Delta l_s \leq 1\%$) for Fu Sheng profile.

Furthermore, in order to minimize the blowhole area without compromising the sealing line length, the extra constraint is set such that the sealing line length reduces by at least 1% and the results are shown in Tables 4.21, 4.23, and 4.25 followed by the new profiles in Figures 4.20 - 4.22. The sealing line lengths of the new profiles are not reduced by more than 2% and the blowhole areas decrease by at least 4% after the optimization is performed under the specified conditions.

4.5 Conclusions

This chapter consists of the complete generation procedure for the rotor profiles of twin screw compressors with minimized blowhole areas. The profiles are generated by adopting the Bezier curve-based deviation functions. To accomplish the main goal of minimizing blowhole area, the partially overlapped three-segment deviation function is proposed for better results in this study. New designs are created in order to make fair comparisons with the selected industrial applications. The sealing line lengths and the blowhole areas are calculated and compared between the new profiles and three existing ones. The results of new designs show that the designs by using the deviation function method can have smaller blowhole areas with possibly shortened sealing line lengths. It is accomplished by letting the blowhole area be the objective function and the sealing line length be an additional constraint. The proposed design method is a systematic way to optimize the rotor profiles for the twin screw compressors and gives the user a variety of options for new designs.

Table 4.20: Parameters for DFM-H3

e_{bot} (mm)	e_{tip} (mm)	e_M (mm)	$\theta_{r,1}$ (rad)	θ_R (rad)	θ_M (rad)	θ_L (rad)
0	22	26.80	1.25	0.85	0.25	0.40

s_{R1} (mm)	s_{R2} (mm)	s_{L1} (mm)	s_{L2} (mm)	s_{M1} (mm)	s_{M2} (mm)	m (mm/rad)
0.34	0.25	0.0040	0.16	0.02	0.13	35.67

Table 4.21: Results for Figure 4.20

Hitachi	Original	DFM-H3	Difference
Sealing Line Length (mm)	113.86	112.05	-1.59%
Blowhole Area (mm^2)	12.94	11.18	-13.60%

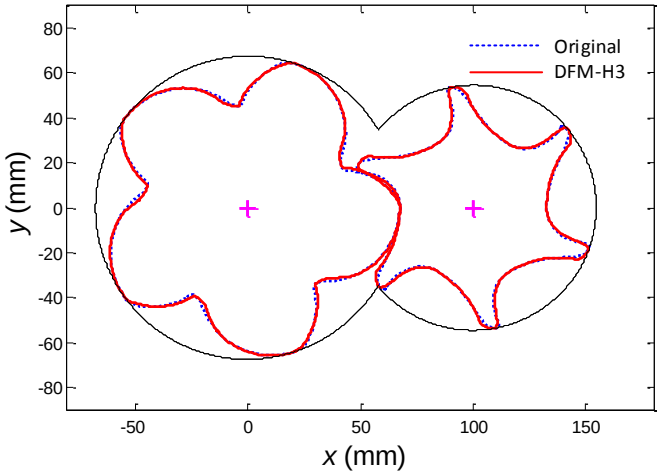

Figure 4.20: Minimized blowhole area ($\Delta l_s \leq -1\%$) for Hitachi profile.

Table 4.22: Parameters for DFM-G3

e_{bot} (mm)	e_{tip} (mm)	e_M (mm)	$\theta_{r,1}$ (rad)	θ_R (rad)	θ_M (rad)	θ_L (rad)
1.00	25.00	39.66	1.25	0.84	0.49	0.41

s_{R1} (mm)	s_{R2} (mm)	s_{L1} (mm)	s_{L2} (mm)	s_{M1} (mm)	s_{M2} (mm)	m (mm/rad)
0.24	0.12	0.0043	0.49	0.04	0.33	42.29

Table 4.23: Results for Figure 4.21

GHH	Original	DFM-G3	Difference
Sealing Line Length (mm)	139.47	137.06	-1.73%
Blowhole Area (mm^2)	1.39	1.33	-4.32%

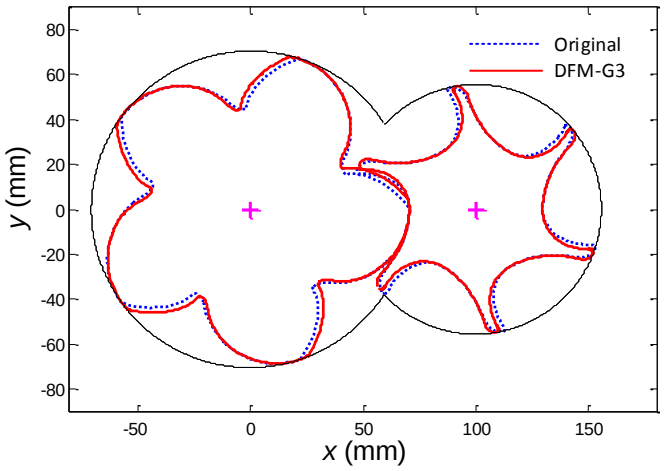

Figure 4.21: Minimized blowhole area ($\Delta l_s \leq -1\%$) for GHH profile.

Table 4.24: Parameters for DFM-F3

e_{bot} (mm)	e_{tip} (mm)	e_M (mm)	$\theta_{r,1}$ (rad)	θ_R (rad)	θ_M (rad)	θ_L (rad)
0.48675	27.255	41.05	1.25	0.86	0.51	0.39

s_{R1} (mm)	s_{R2} (mm)	s_{L1} (mm)	s_{L2} (mm)	s_{M1} (mm)	s_{M2} (mm)	m (mm/rad)
0.08	0.08	0.0016	0.25	0.14	0.25	41.93

Table 4.25: Results for Figure 4.22

Fu Sheng	Original	Optimal	DFM-F3	Difference
Sealing Line Length (mm)	139.63	146.84	144.91	-1.31%
Blowhole Area (mm^2)	6.64	2.63	2.49	-5.32%

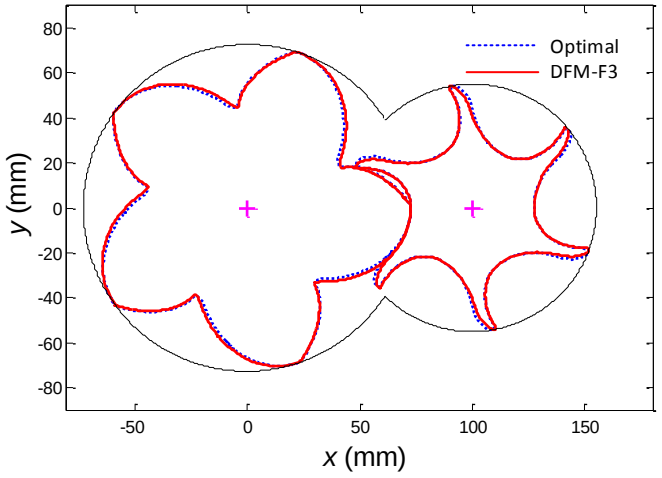

Figure 4.22: Minimized blowhole area ($\Delta l_s \leq -1\%$) for Fu Sheng profile

Chapter 5

Twin Screw Compressor with Non-Constant Lead

The twin screw compressors described previously are helical lobes with constant lead. The lead, defined the same as for a screw, is the axial distance covered by a complete revolution of the screw compressor. While the constant lead screw compressors are prevailing, varying the lead of a screw compressor to a non-uniform value results in modifying the surface properties. Therefore, the geometric characteristics of the screw compressor with non-constant lead are distinctly different than those of the compressor with constant lead. Figure 5.1 shows rotors of twin screw compressors with non-constant lead. In Figure 5.1a, the lead increases as the grooves twist from the suction plane to the discharge plane; while in Figure 5.1b, the lead decreases instead. The idea of the twin screw compressor with variable lead was patented by Gardner [74] in 1969. However, due to the manufacturing constraints, the use of the twin screw compressors with non-constant lead is limited so far. Gardner suggested fabricating the rotors with non-uniform lead by stacking metal plates with different leads. He also presumed that the non-constant lead screw compressor can increase internal pressure rapidly, and thus it has a larger discharge port area and less throttling loss when the same pressure ratio is kept constant. In order to analyze the performance of such machines, the simu-

lation model for the screw compressor with non-constant lead is developed based on that of the constant lead screw compressor in this chapter. The analytical results are compared between the screw compressors, which have the same rotor profiles, but with constant and non-constant leads, respectively.

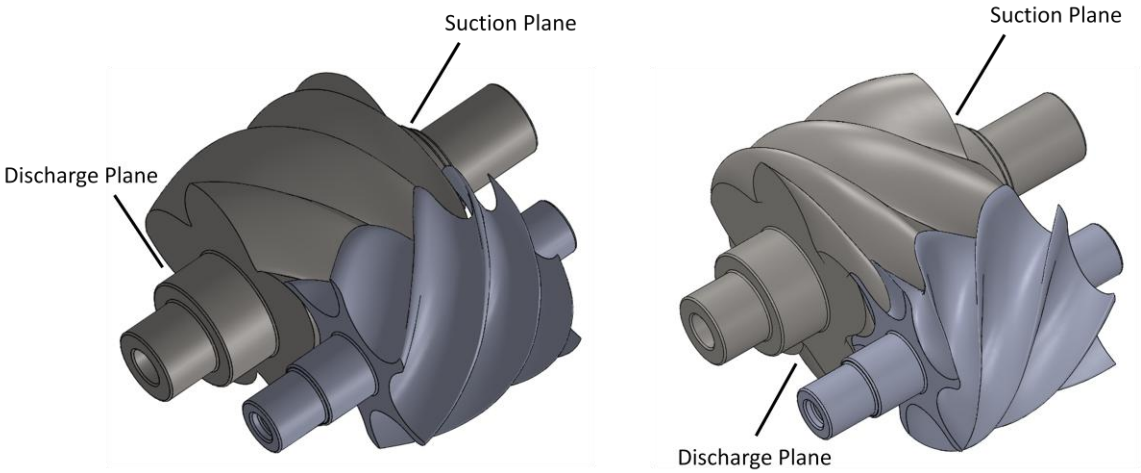

(a) Increasing lead (b) Decreasing lead

Figure 5.1: Rotors of twin screw compressors with non-constant lead.

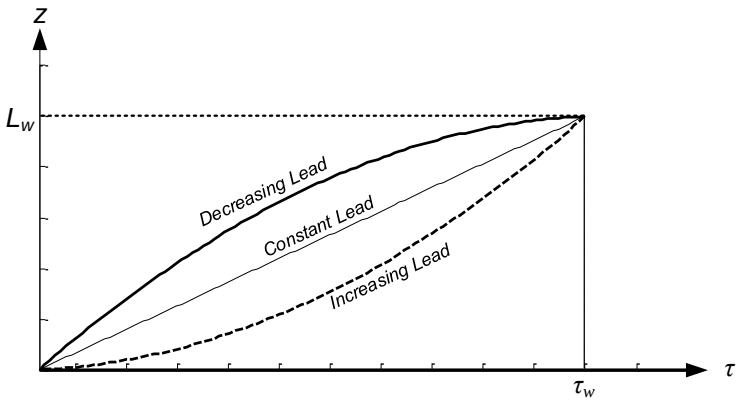

Figure 5.2: Relationship between axial translation and twist angle for rotors with different types of leads.

5.1 Variation of Lead

In this chapter, the effects of varying the lead on the screw compressor are investigated. All other design parameters, such as the profile of rotors, the combination of male and female rotors, the rotor length and diameter, the wrap angle, and so forth, are kept the same for fair comparisons. The definition of lead is the axial distance covered by a complete revolution of the screw compressor. Figure 5.2 shows the relation between the axial translation and the twist angle. The slope illustrates the variation of lead. The possible variants discussed in this study are constant, linear, quadratic, cubic, and Bezier curve leads. The screw parameter function is defined to depict the change of the lead as

$$p(\tau) = \frac{dz}{d\tau} \tag{5.1}$$

where z is the axial position of the rotor and τ is the twist angle of the rotor. It represents the variation of lead at each axial position on the helical rotor. As the lead varies, two tendencies are discussed in this research; that is, as the rotor twists, it is either increasing, shown as the curve below the constant lead in Figure 5.2, or decreasing, shown as curves above the constant lead in Figure 5.2. The corresponding shapes of the rotor surfaces of increasing lead and decreasing lead are illustrated in Figure 5.1.

5.2 Effects of Non-Constant Lead on Variation of Chamber Volume and Pressure Rise

The volumetric displacement of the non-constant lead compressors is obviously different than that of the constant lead compressors. Figure 5.3a shows the volumetric displacement of compressors with constant, linearly increasing, and linearly decreasing leads, respectively. As it can be seen, the volumetric displacement during the compression process for the linearly decreasing lead compressor is faster than that of the constant lead, while that of the linearly increasing lead compressor is usually slower. As seen in Figure 5.3b, the pressure rises more rapidly inside the compression chamber for the linearly decreasing lead compressor, but slower for the linearly increasing lead one.

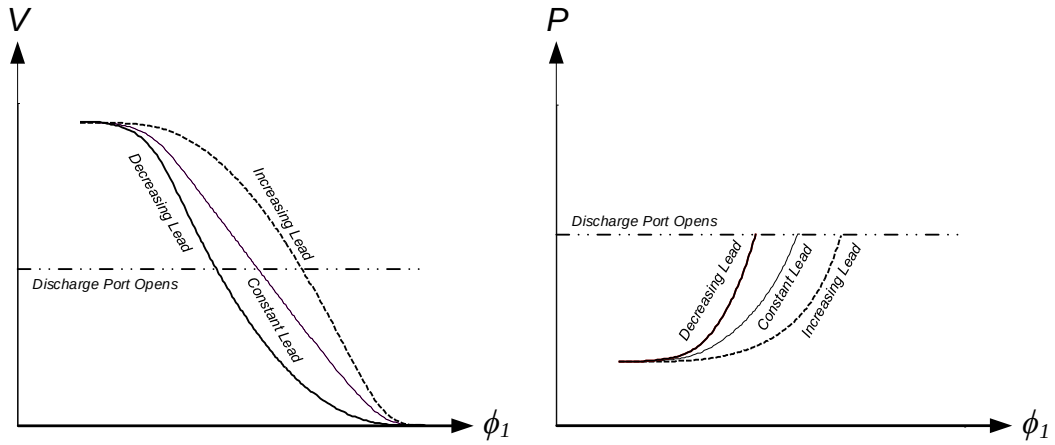

Figure 5.3: Volumetric displacement and pressure rise during compression process.

For a compressor, the built-in volume index is the ratio between the suction porting closure volume and the discharge porting open volume. The suction porting closure volume is the maximum volume of the chamber at the instant when the suction port is

closed and the compression process just begins. The discharge porting open volume is the volume of the compression cavity at the moment when the chamber opens to the discharge port and the compression process ends. According to the volumetric displacement diagram shown in Figure 5.3a, for twin screw compressors with the same built-in volume index, the compressor with constant lead achieves its built-in volume ratio faster than the compressor with linearly increasing lead, but slower than the compressor with linearly decreasing lead. Achieving the same built-in volume index earlier implies that the discharge port area is larger and thus the compression chamber reaches the discharge porting earlier and opens to outlet. This mitigates the throttling losses. If the discharge port area is intended to be the same for compressors with constant lead and variable lead, the compression ratio of the constant lead compressor is lower than the compressor with the linearly decreasing lead one, but it is higher than that of the linearly increasing lead compressor.

5.3 Leakage Reduction of Twin Screw Compressors with Non-Constant Lead

Given that all design parameters of the twin screw compressor with constant lead and non-constant lead are the same, the geometrical properties, inclusive of the interlobe sealing line and the blowhole, are different between these two kinds of twin screw compressors. Since the leakage loss is proportional to the interlobe sealing line length as well as the blowhole area, the reduction of leakage can be achieved by adapting the

lead of the twin screw compressor to a non-constant lead. The design and analysis procedure are discussed in this section.

5.3.1 Leakage Model

Leakage is an inevitable phenomenon for a twin screw compressor. It is a vital factor that affects the compressor's performance. The interlobe sealing line and the blowhole area are the major leakage paths in the twin screw compressor. Generally, it is very difficult to accurately measure the amount of those leaks from experiments. Therefore, the convergent nozzle model is adopted to evaluate the leakage [75, 76]. The leakage flow rate is

$$\dot{m} = AP_h \sqrt{\frac{2k}{(k-1)RT_h}} \sqrt{\left(\frac{P_l}{P_h}\right)^{2/k} - \left(\frac{P_l}{P_h}\right)^{(k+1)/k}} \tag{5.2}$$

When

$$\left(\frac{2}{k+1}\right)^{k/(k-1)} < \frac{P_l}{P_h} < 1$$

and

$$\dot{m} = AP_h \sqrt{\frac{k}{RT_h}} \left(\frac{2}{k+1}\right)^{0.5(k+1)/(k-1)} \tag{5.3}$$

When

$$0 < \frac{P_l}{P_h} < \left(\frac{2}{k+1}\right)^{k/(k-1)}$$

where A is the area of the leakage path, P_l and P_h are the lower pressure and high pressure of the adjacent chambers, T_h is the temperature of the high pressure chamber, R is the gas constant, and k is the specific heat ratio. An example leakage flow rate is calculated and the result is illustrated in Figure 5.4.

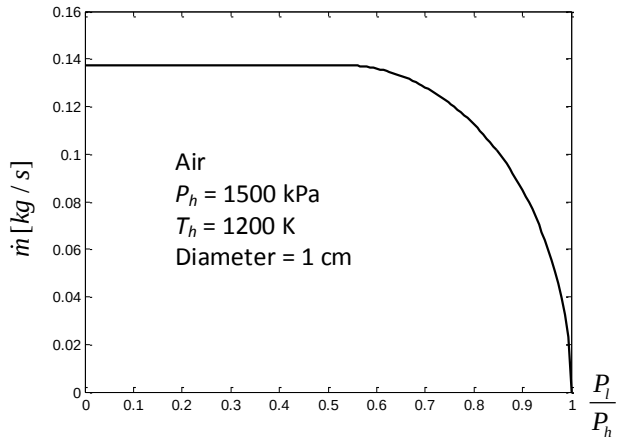

Figure 5.4: Leakage flowrate.

5.3.2 Interlobe sealing line and blowhole area as the lead is varying

It is obvious that making the lead a non-constant value influences the evolution of interlobe sealing line and blowhole. In this section, the differences of interlobe sealing lines and blowholes between the variants of the non-constant lead and constant lead compressors are revealed. First of all, the constant and linear lead cases are examined. When the lead is non-constant, it can be either monotonically increasing or decreasing. Figure 5.2 shows the relation between the axial translation and the twist angle for those

three cases. The evolution of interlobe sealing lines and the blowholes are plotted in Figure 5.5.

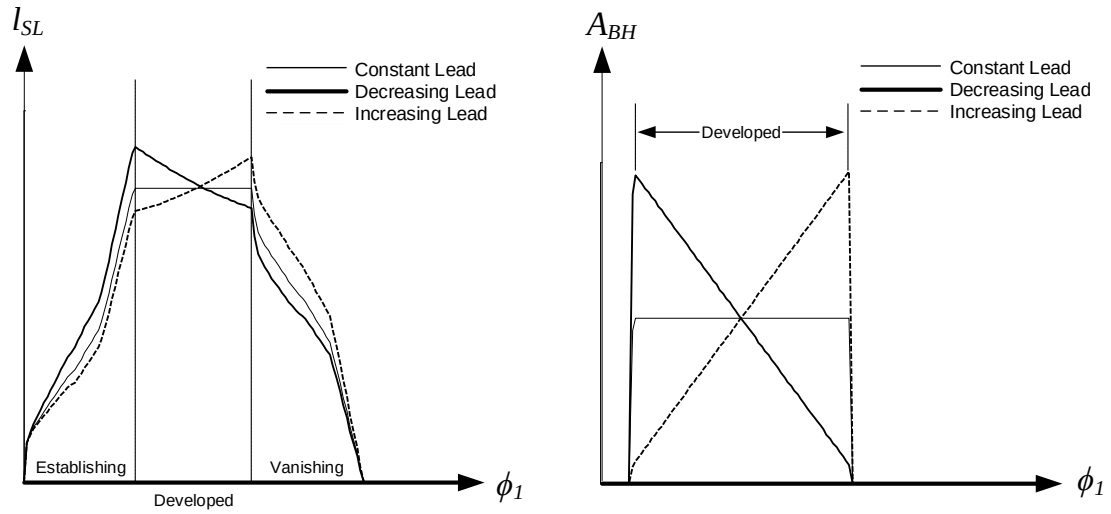

Figure 5.5: Evolution of interlobe sealing line length and blowhole area.

As can be seen in Figure 5.5a, each curve is basically divided into three portions. In the left portion, the interlobe sealing line is establishing and incomplete, and thus, its length is increasing. In the middle portion, the interlobe sealing line is completely developed. During this segment, the length may remain constant, increase, or decrease. The tendency depends on the type of lead. In the right portion, the interlobe sealing line is vanishing after it starts reaching the discharge end plane and hence, the length is decreasing for each case. The area of the leakage through the interlobe sealing line can be calculated as

$$A_s = l_s \delta \tag{5.4}$$

where l_s is the length of interlobe sealing line and δ is the clearance height between rotors.

By observing Figure 5.5b, the blowhole area has the similar trend. However, the establishing and vanishing portion is not obvious since the blowhole is so tiny that it builds up and disappears rapidly at the end plane.

5.3.3 Effects on leakage reduction as the lead is non-constant

With the data of the pressure rise in a chamber and that of the evolution of interlobe sealing line and blowhole, the leakage of a chamber can be evaluated by applying modeling equations in Section 5.3.1. The leakage through the interlobe sealing line and the blowhole are depicted in Figure 5.6. It shows that the screw compressor with increasing lead tends to have less leakage. With those curves for leakage flowrate through interlobe sealing line and the blowhole, the amount of leakage can be integrated as

$$m = \int_t \dot{m}\, dt = \int_\phi \frac{\dot{m}}{\omega}\, d\phi \tag{5.5}$$

And the total leakage mass is

$$m_{TOT} = m_{SL} + m_{BH} \tag{5.6}$$

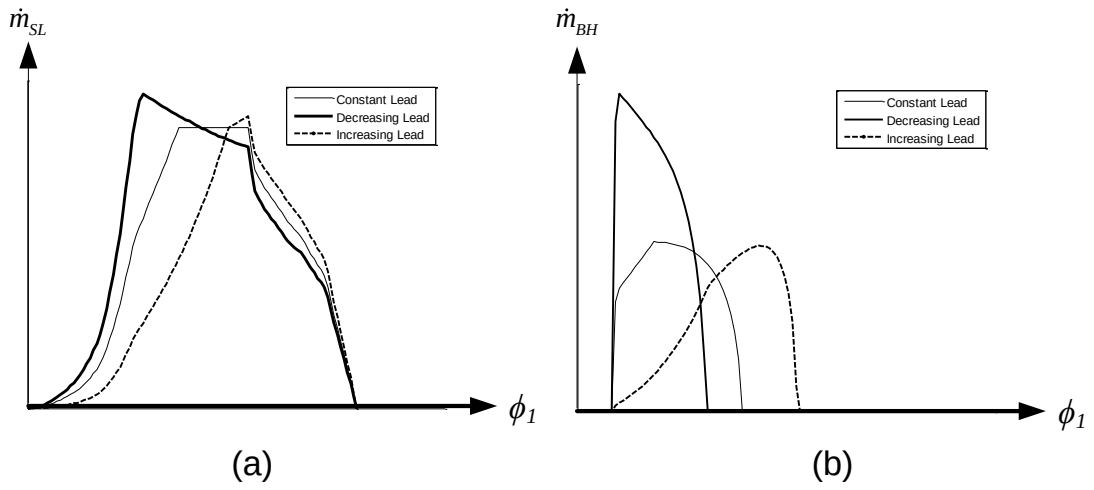

Figure 5.6: Variation of leakage flowrate through the interlobe sealing and blowhole.

5.4 Results for Volumetric Efficiency of Screw Compressors with Non-Constant Lead

In order to seek for the non-constant lead compressor with higher leakage reduction, several variants, including linear, quadratic, cubic, and Bezier-curve leads are investigated and the curves are shown in Figure 5.7. The Bezier curve is adopted here to increase the adjustability of the lead. The formulas and control points for those leads are tabulated in Table 5.1.

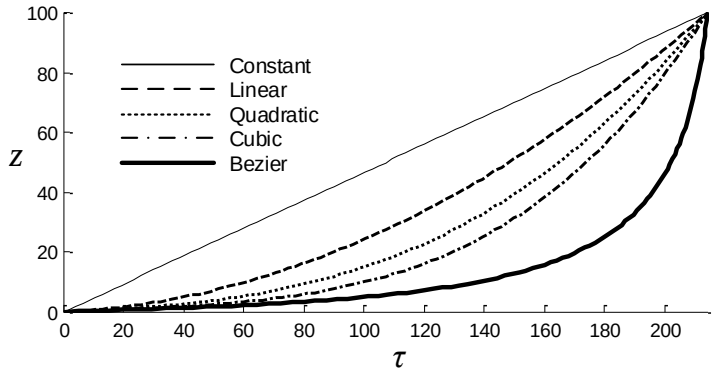

Figure 5.7 Variants of lead curve

Table 5.1: Formulation of different screw parameter functions for non-constant lead

Type of Lead	Formula or control points of the curve
Constant	$z = \frac{L_w}{\tau_w}\tau$
Linear curve	$z = 0.9\frac{L_w}{\tau_w^2}\tau^2 + 0.1\frac{L_w}{\tau_w}\tau$
Quadratic curve	$z = 0.8\frac{L_w}{\tau_w^3}\tau^3 + 0.1\frac{L_w}{\tau_w^2}\tau^2 + 0.1\frac{L_w}{\tau_w}\tau$
Cubic curve	$z = 0.5\frac{L_w}{\tau_w^4}\tau^4 + 0.5\frac{L_w}{\tau_w^3}\tau^3 - 0.1\frac{L_w}{\tau_w^2}\tau^2 + 0.1\frac{L_w}{\tau_w}\tau$
Bezier curve	$\mathbf{P}_0 = (0,0)\ \ \mathbf{P}_1 = (0.802, 0.053)\ \ \mathbf{P}_2 = (0.957, 0.117)\ \ \mathbf{P}_3 = (\tau_w, L_w)$

To make those twin screw compressors with non-constant lead more applicable to the practice, several combinations of operation conditions in practice have to be considered. The objective of the following investigation is to study the possible effects of operational parameters on performance of the twin screw compressor with non-constant lead. Those parameters include the clearance height between the lobes of rotors, the com-

pression ratio, the rotor speed, and the different working gases. Usually, the range clearance height between rotors can be 10 *μm* to 150 *μm* due to manufacturing tolerance. The smaller the clearance, the less fluid leaks out from the compression chamber. As for the compression ratio, it is between 2 and 15 for a single-stage twin screw compressor. When the compression ratio is low, the driving force of fluid leakage is low. Meanwhile, if the rotational speed of the rotor is high, the working media in the chamber is less likely to leak out and tends to be kept in the chamber. The rotor speeds taken into account in this research are low at 1910 rpm, moderate at 4350 rpm, and high at 6000 rpm. Lastly, air, helium, and nitrogen are the selected working gases in this study. Air is a mixture of oxygen, nitrogen, and traces of other gases. Its molecular weight is around 29. The thermodynamic properties of nitrogen are similar to those of air. Helium is chosen as an example of monatomic gases.

When the working gas leaks from a chamber through leakage paths, it goes directly back into the suction chamber and the trailing cavity, and as a result, the volumetric efficiency is affected. The variation of volumetric efficiency with pressure ratio at fixed interlobe clearance between rotors and at different rotational speeds of male rotor working on different gases is shown in Figures 5.8 - 5.10 for the compressor with constant lead. The variation of volumetric efficiency of helium is more significant due to a higher leakage rate. Variation of volumetric efficiency with pressure ratio for different gases at fixed male rotor speed and interlobe clearance is illustrated in Figure 5.11. The influence of pressure ratio on volumetric efficiency is more significant for helium than that for the other two gases.

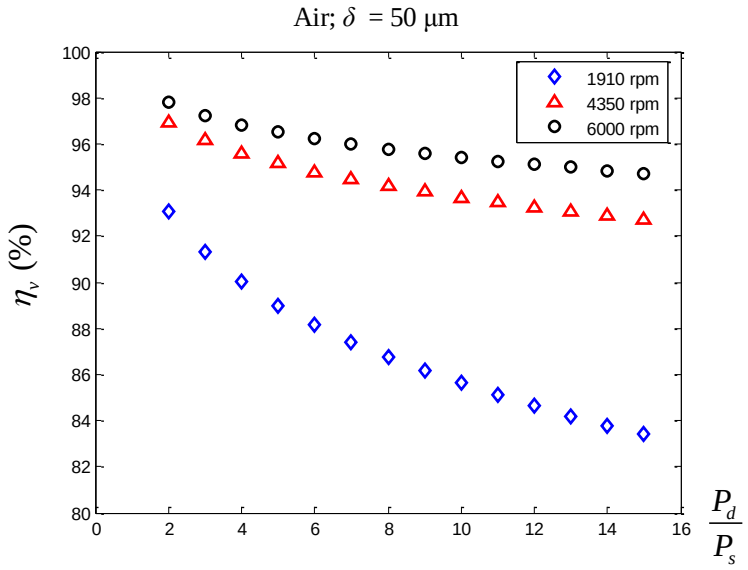

Figure 5.8: Influence of pressure ratio and rotational speed on volumetric efficiency at fixed interlobe clearance with air for the compressor with constant lead.

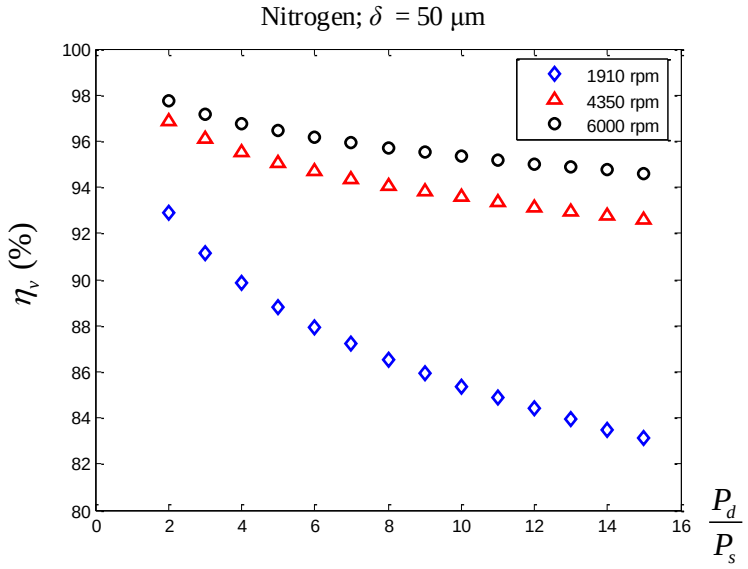

Figure 5.9: Influence of pressure ratio and rotational speed on volumetric efficiency at fixed interlobe clearance with nitrogen for the compressor with constant lead.

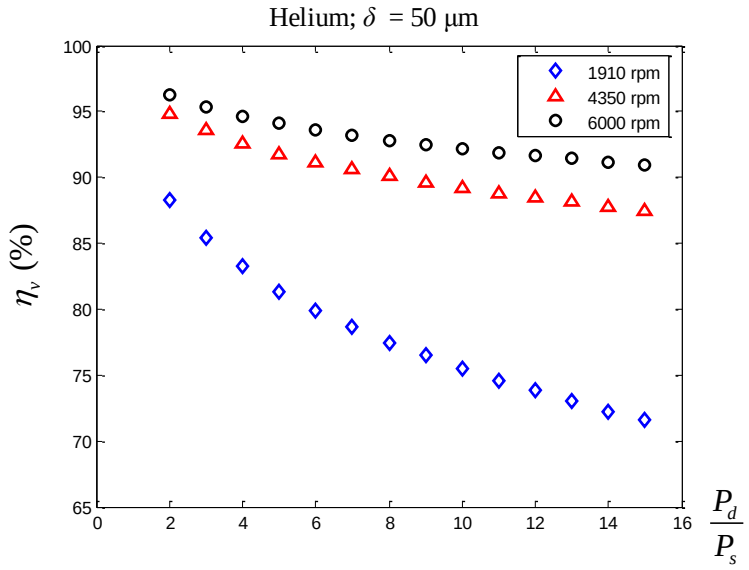

Figure 5.10: Influence of pressure ratio and rotational speed on volumetric efficiency at fixed interlobe clearance with helium for the compressor with constant lead.

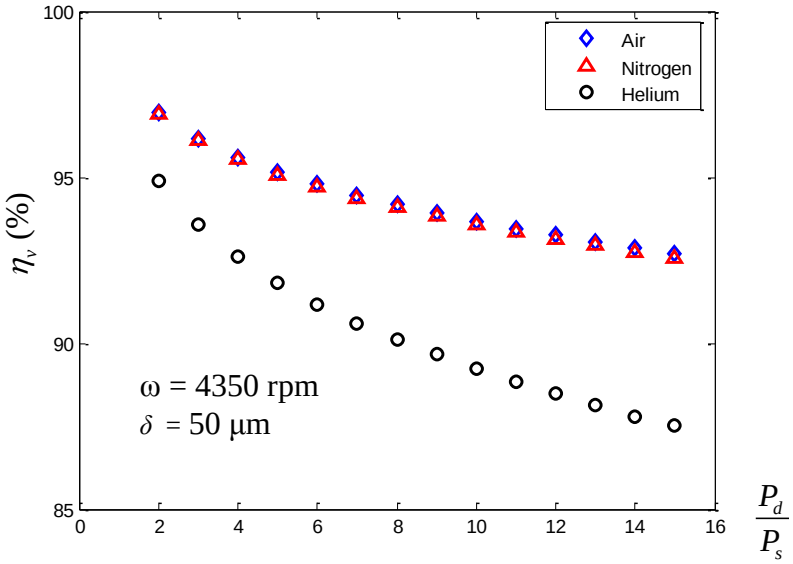

Figure 5.11: Variation of volumetric efficiency with pressure ratio at fixed interlobe clearance and at fixed rotational speed of male rotor with different gases for the compressor with constant lead.

Figure 5.12 presents the influence of rotational speed of male rotor on volumetric efficiency with different working gases at fixed moderate interlobe clearance and pressure

ratio. At low rotational speed, the volumetric efficiency of a compressor working on helium is lower than that of the other selected gases. When the speed gets higher, the efficiency difference among different working gases becomes less clear.

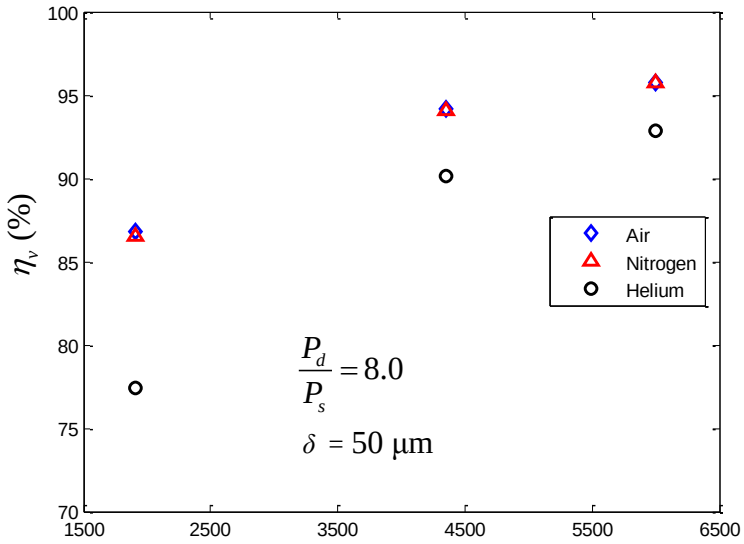

Figure 5.12: Variation of volumetric efficiency with different working gases at different rotational speed at a fixed interlobe clearance for for the compressor with constant lead.

The comparisons of volumetric efficiency among compressors with different leads are evaluated at different conditions for selected gases, shown in Figures 5.13 - 5.18. From those figures, it can be seen that where the compression ratio is low, the rotor speed is high, and the interlobe clearance is small, the effect of the non-constant lead screw compressor on leakage mitigation and improved volumetric efficiency is subtle. Conversely, when the leakage rate is higher due to the high demand and/or worse operating conditions, the effect of varying the lead along the axis of a screw compressor is significantly helpful on the reduction of leakage, and thus improves the volumetric efficiency dramatically for all selected gases, especially helium. Among a variety of lead curves

examined in this study, the Bezier-type curve can result in the highest volumetric efficiency under all conditions.

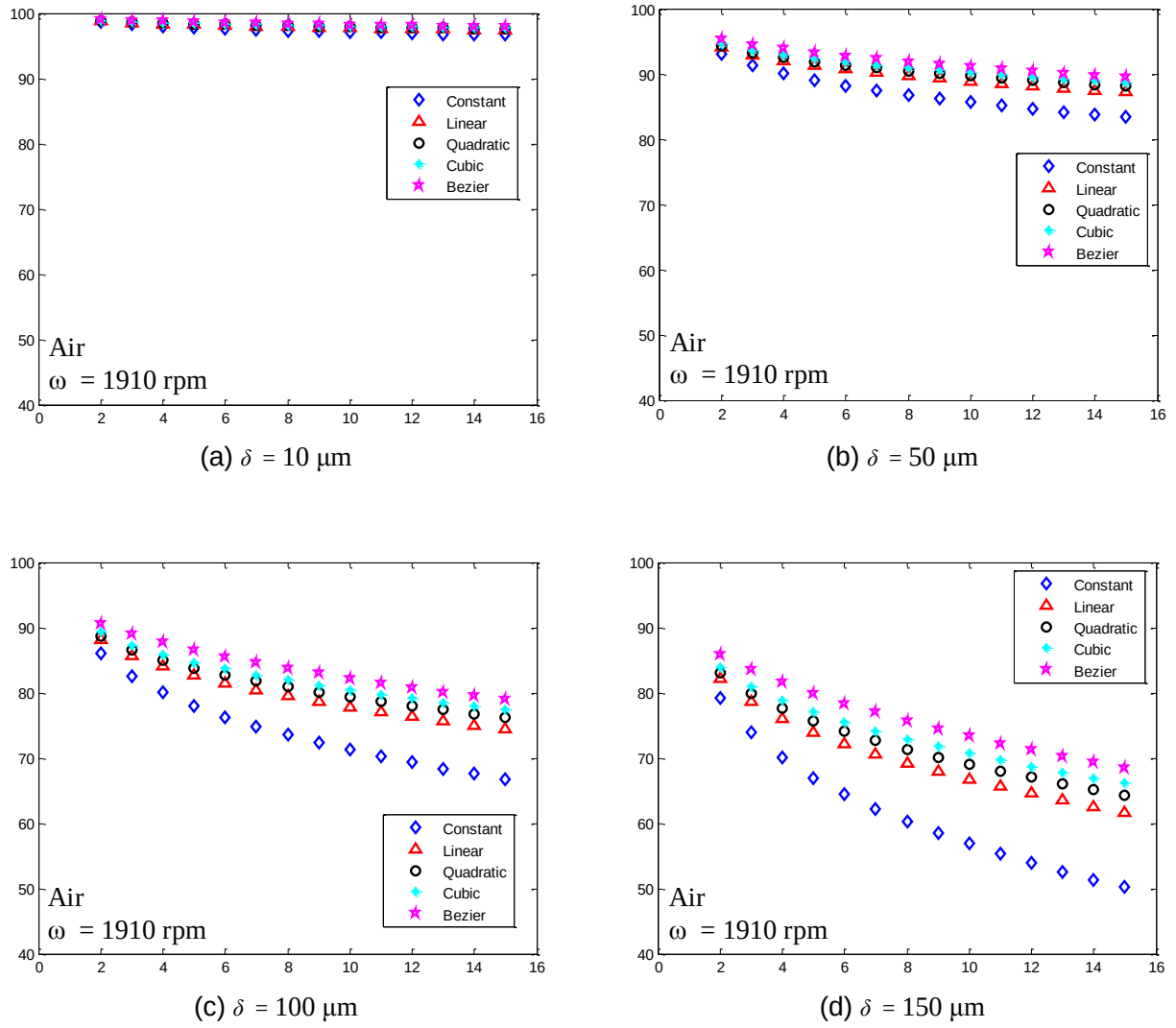

(a) δ = 10 μm

(b) δ = 50 μm

(c) δ = 100 μm

(d) δ = 150 μm

Figure 5.13: Variation of volumetric efficiency with pressure ratio at the same rotational speed at different interlobe clearance with air for compressors with different leads.

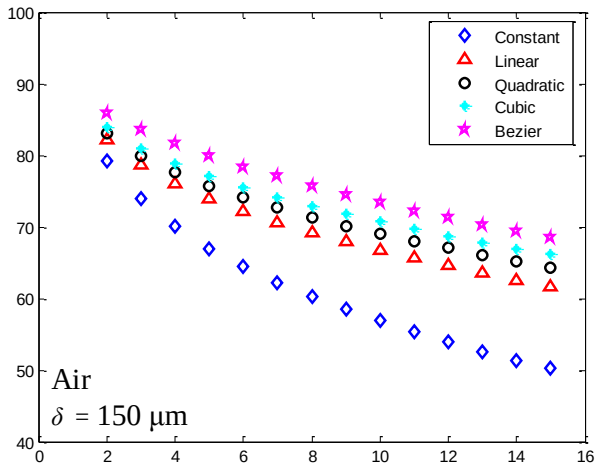

(a) ω = 1910 rpm

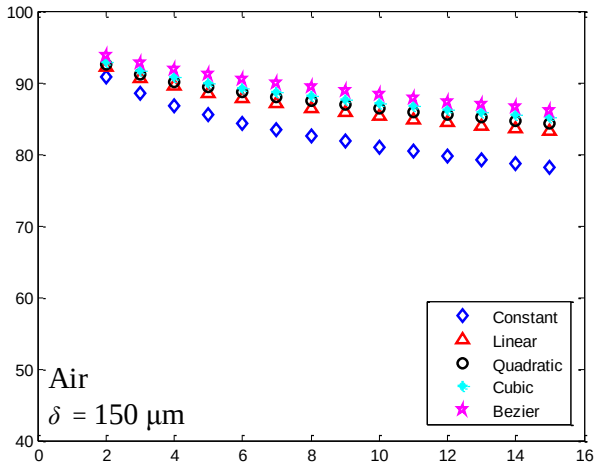

(b) ω = 4350 rpm

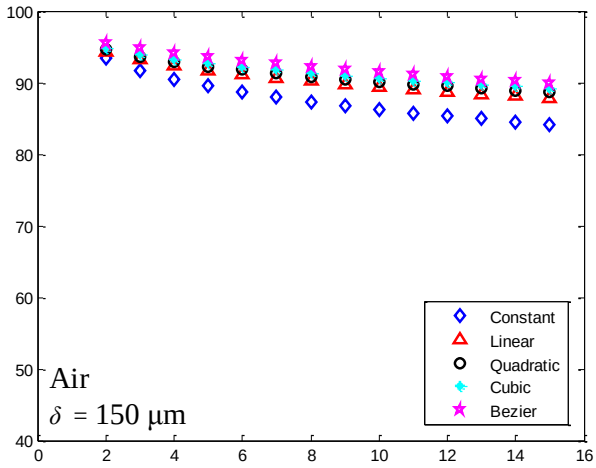

(c) ω = 6000 rpm

Figure 5.14: Variation of volumetric efficiency with pressure ratio at the same interlobe clearance at different rotational speed with air for compressors with different leads.

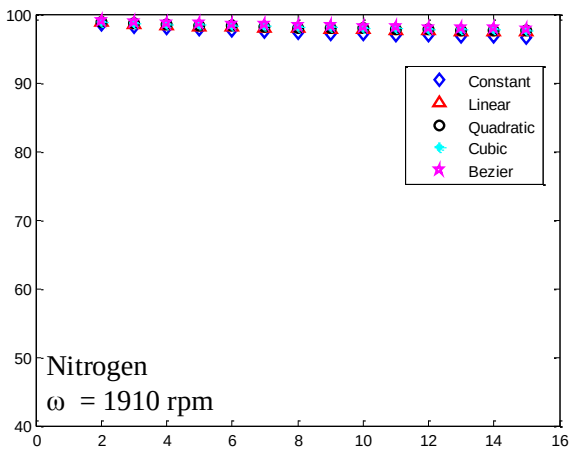

(a) δ = 10 μm

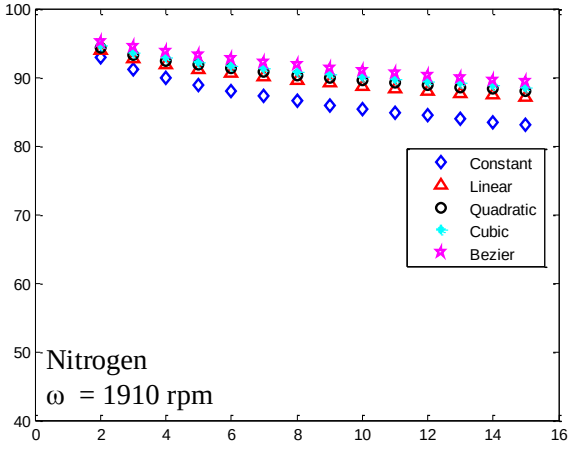

(b) δ = 50 μm

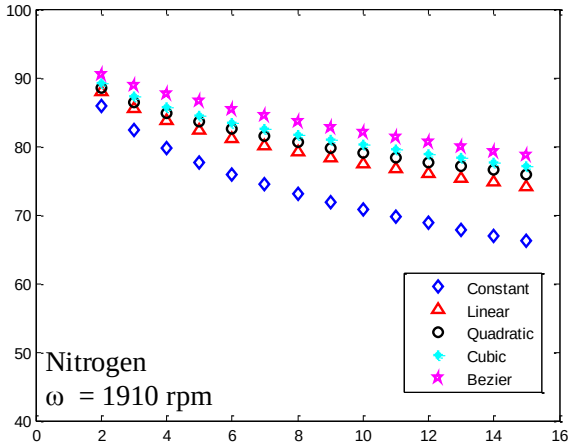

(c) δ = 100 μm

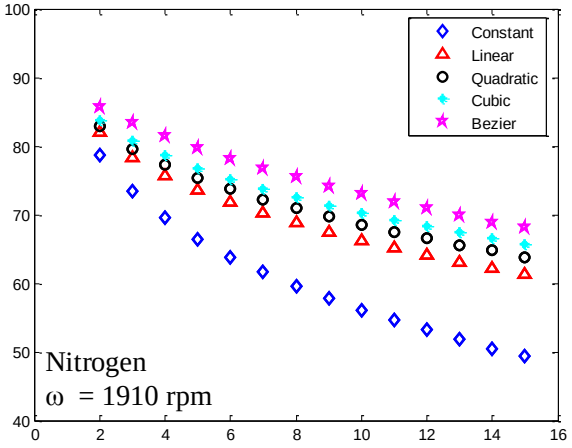

(d) δ = 150 μm

Figure 5.15: Variation of volumetric efficiency with pressure ratio at the same rotational speed at different interlobe clearance with nitrogen for compressors with different leads.

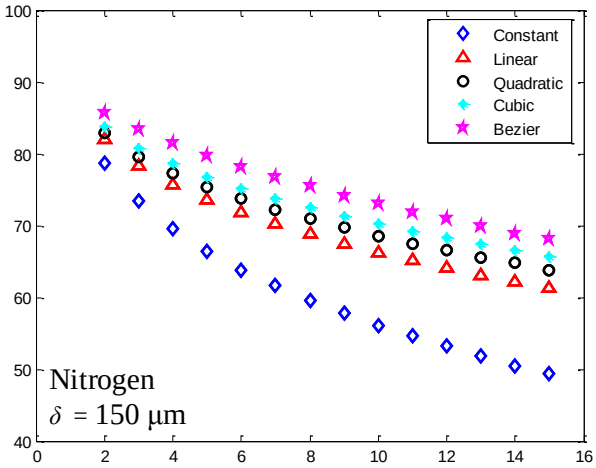

(a) ω = 1910 rpm

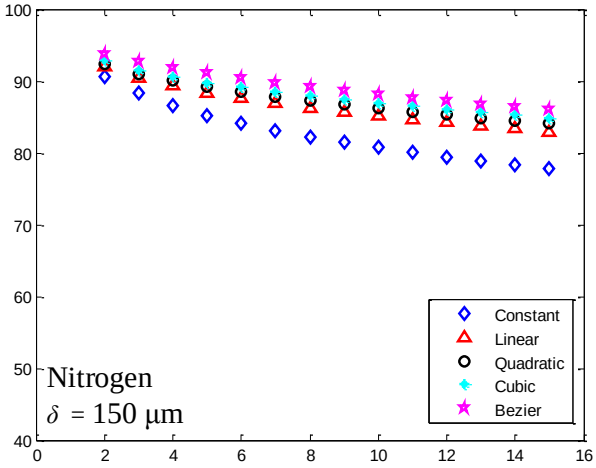

(b) ω = 4350 rpm

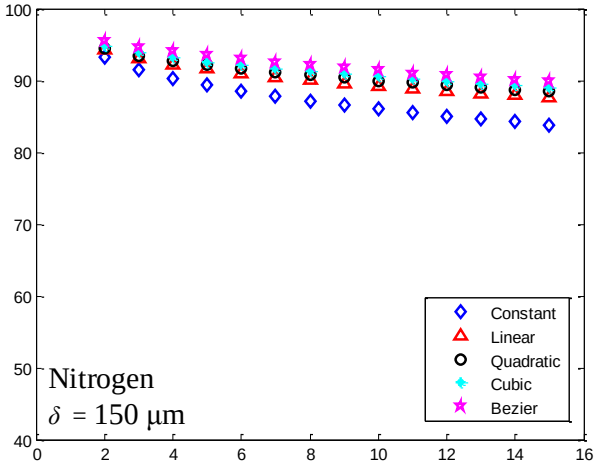

(c) ω = 6000 rpm

Figure 5.16: Variation of volumetric efficiency with pressure ratio at the same interlobe clearance at different rotational speed with nitrogen for compressors with different leads.

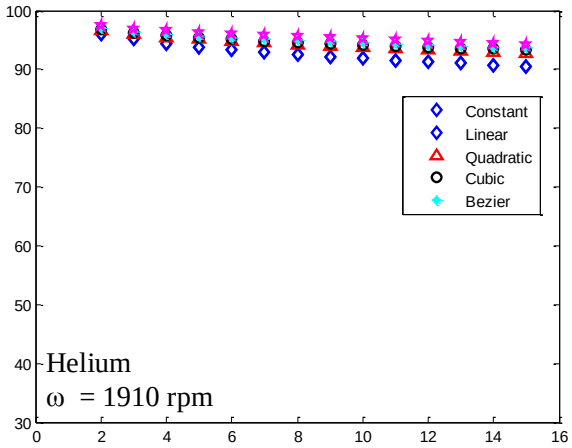

(a) δ = 10 μm

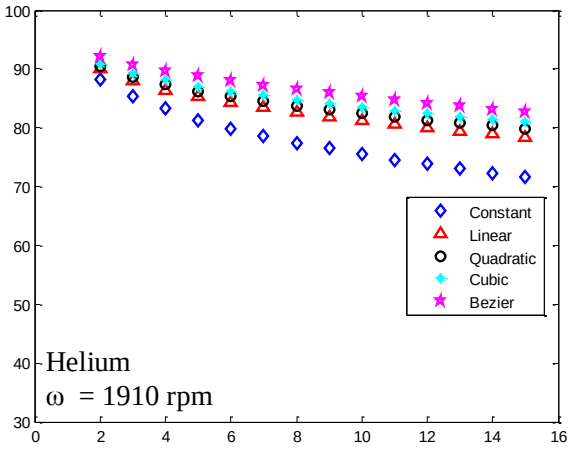

(b) δ = 50 μm

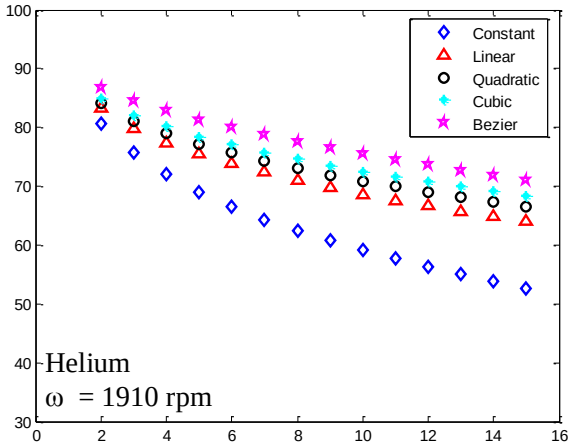

(c) δ = 100 μm

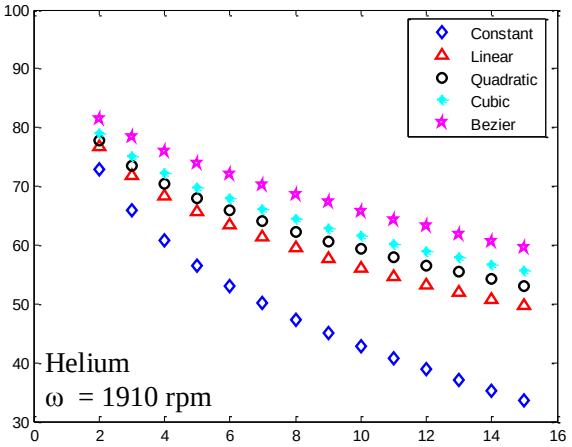

(d) δ = 150 μm

Figure 5.17: Variation of volumetric efficiency with pressure ratio at the same rotational speed at different interlobe clearance with helium for compressors with different leads.

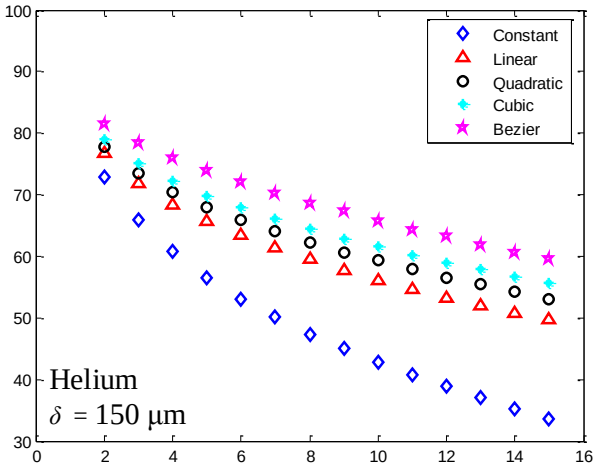

(a) ω = 1910 rpm

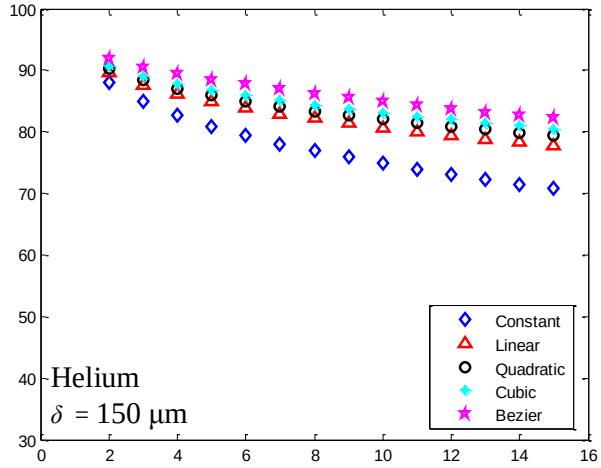

(b) ω = 4350 rpm

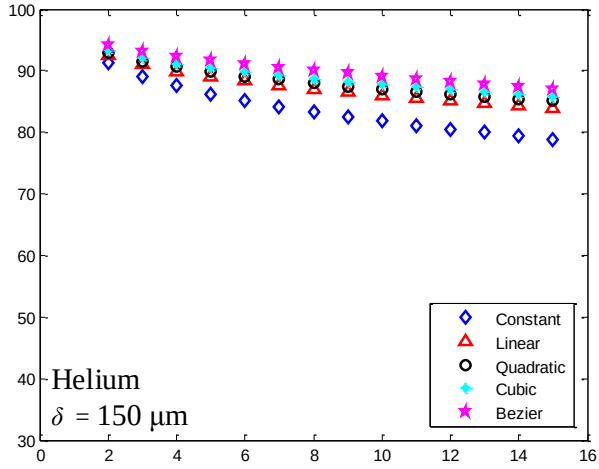

(c) ω = 6000 rpm

Figure 5.18: Variation of volumetric efficiency with pressure ratio at the same interlobe clearance at different rotational speed with helium for compressors with different leads.

5.5 Conclusions

The effects of varying the lead along the axis of the screw compressor are studied in this chapter. The screw compressor's geometric characteristic and performance are affected by the non-uniformity of the lead. The possible variants are categorized into two

groups, which are screw compressor with increasing lead and decreasing lead. The screw compressor with decreasing lead displaces the gas faster than that of constant lead and that of increasing lead. As a result, the pressure rises more rapidly inside the compression chamber of the screw compressor with decreasing lead. The leakage of the twin screw compressors with constant and non-constant leads are calculated by investigating the interlobe sealing line and blowhole area and adopting convergent nozzle leakage model. It shows that the screw compressor with increasing lead tends to retain more gas inside its compression chamber since the leakage rate is smaller. Furthermore, several different types of increasing lead curves are applied to generate the helical surface of the screw compressor. The volumetric efficiency of these screw compressors are computed under combinations of practical operating conditions. From the results, it is found that under the worse or high demand conditions where the screw compressor tends to leak more gas, varying the screw lead along the rotor axis helps mitigate the influence of those worse conditions and reduce the leakage of working gas. The twin screw compressor with Bezier curve lead has the highest leakage reduction and thus the best volumetric efficiency among other types of lead curves discussed in this study.

Chapter 6

Conclusions and Future Work

6.1 Conclusions

In Chapters 2 through 5, the design and analysis of the twin screw compressors by deviation function method was presented. The most significant contributions are summarized as follows:

1. The development of the Bezier curve-based deviation function method for the profile generation of the twin screw compressor

   By this method of twin screw compressor design, many more compressor profiles are possible than with the conventional design methods. With the adoption of the Bezier curve-based deviation function, the continuity conditions of the profiles are easier to achieve than before. In addition, the complexity of combining multiple different curves as generating curves in a profile is annihilated, and values of parameters of generating curves can be determined with less effort. Thus, the optimization process can be applied to all kinds of profiles rather than for a specific type of profile at a time with the conventional method. The partially overlapped three-segment third-order Bezier curve-based deviation function is proposed in this study and it is helpful in finding profiles with better performance. Since the proposed design approach tends to produce an even more diverse variety of possible designs, the optimization results are

more universal. Finally, rotor profiles whose performance is better than that of the existing industry profiles can be generated from this method.

2. Design of twin screw compressors with non-constant lead

The properties and performance of the twin screw compressor with non-constant lead are discussed and compared with those of the twin screw compressor with constant lead. It shows that the twin screw compressor with decreasing lead displaces the volume in a chamber faster and has more rapid pressure rise; however, it has the tendency to leak more working gas through the interlobe sealing line and blowhole area. The twin screw compressor with increasing lead, on the other hand, has better leakage reduction and thus higher volumetric efficiency. Among various lead curves discussed in this study, the Bezier curve-typed lead can produce the best result with the objective of improving volumetric efficiency. The idea of varying the lead has a more significant influence on the improvement of volumetric efficiency especially under the worse and high demand operating conditions when the leakage rate tends to be high.

6.2 Future Work

Some further research topics are listed below:

1. Rotor profile designs of the twin screw compressors can be further developed with more deviation functions. To achieve this goal, the basis splines (B-splines) or its powerful extension non-uniform rational B-splines (NURBS) can be possible alternatives for the Bezier curves. Those curves are all popular in computer-aided design (CAD), computer aided manufacturing (CAM) and computer graphics (CG) fields.

2. The deviation functions used for the rotor profile design of the twin screw compressor are divided into three main segments to fulfill the goal of minimizing the leakage triangular area with a shorter interlobe sealing line length. Further investigation can be done to find the better formation of functional segments for the deviation function when more design considerations are taken into account, such as lower pressure load, better torque transmission, higher power efficiency, and so on.
3. The use of the twin screw compressors with non-constant lead is limited and still under development. Since the non-constant lead compressor has better performance merit in many aspects, the further study should be done in order to bring this type of twin screw compressor into practice.

Bibliography

[1] N. Stosic, I. K. Smith and A. Kovacevic, Screw Compressors – Mathematical Modelling and Performance Calculation, Berlin: Springer-Verlag, 2005.

[2] J. A. O'Brien, Course outline for screw compressors, NY: Internal short course given at United Technologies Carrier in Syracuse, March 1987.

[3] R. N. Brown, Comporessors, Selection & Sizing, Houston, TX: Gulf Publishing Company, 1986.

[4] P. D. Laing, "The place the screw compressor in refrigeration," in *Symposium on an Engineering Review of Refrigeration Technology and Equipment*, London, March 1968.

[5] P. O'Neill, "Development of the screw compressor and its applications in petrochemical and related industries," in *Fluid Machinery for the oil, petrochemical and related industries: European Congress sponsored by the Power Industries Division of the Institution of Mechanical Engineers and the Division of Mechanical Engineering and Naval Architecture of the Royal Dutch*, London, 1981.

[6] S. Ernst, "Advantages of screw compressors," *Heating/Piping/Air Conditioning,* no. 104, pp. 85-86, November 1987.

[7] W. Dillenbeck, "The turn of the screw," *Australian Refrigeration, Air Conditioning and Heating,* vol. 44, no. 7, pp. 30-31, July 1990.

[8] J. W. Pillis, "Advancement in refrigeration screw compressor design," *ASHRAE Transactions,* pp. 219-224, May 1986.

[9] I. R. Klein, "Screw compressors for heat pump applications," in *Proceedings of the 1978 International Compressor Engineering Conference at Purdue*, West Lafayette, IN, 1978.

[10] Y. Fukazawa and U. Ozawa, "Small screw compressors for automobile air-conditioning systems," in *Proceedings of the 1980 International Compressor Engineering Conference at Purdue*, West Lafayette, IN, 1980.

[11] B. C. Price, "Know the range and limitations of screw compressors," *Chemical Engineering Progress,* pp. 50-56, February 1991.

[12] A. Lundberg, "A comparison of SRM and globoid type screw compressors at full load," in *Proceedings of the 1978 International Compressor Engineering Conference at Purdue*, West Lafayette, IN, 1978.

[13] Y. Tang and J. S. Fleming, "Obtaining the optimum gerometrical parameters of refrigeration helical screw compressor," in *Proceedings of the 1992 International Compressor Engineering Conference at Purdue*, West Lafayette, IN, 1992.

[14] L. Sjoholm, "Important Parameters for small twin screw refrigeration compressors," in *Proceedings of the 1986 International Compressor Engineering Conference at Purdue*, West Lafayette, IN, 1986.

[15] P. J. Singh and J. R. Schwartz, "Exact analytical representation of screw compressor rotor geometry," in *Proceedings of the 1990 International Compressor Engineering Conference at Purdue*, West Lafayette, IN, 1990.

[16] A. N. Vinogradov, S. A. Volodichev, G. A. Kanyshev, V. E. Konstantinov and N. P. Kuryshkin, "Calculation of the geometrical parameters of screw compressors," *Chemical and Petroleum Engineering,* Vols. 9-10, pp. 493-495, Sept-Oct 1986.

[17] P. J. Singh and A. D. Onuschak, "A comprehensive, computerized method for twin screw rotor profile generation and analysis," in *Proceedings of 1984 International Compressor Engineering Conference at Purdue*, West Lafayette, IN, 1984.

[18] P. J. Singh and G. C. Patel, "A generalized performance computer program for oil flooded twin screw compressors," in *Proceedings of 1984 International Compressor Engineering Conference at Purdue*, West Lafayette, IN, 1984.

[19] L. Zhang and J. F. Hamilton, "Main geometric characteristics of twin screw compressors," in *Proceedings of the 1992 International Compressor Engineering Conference at Purdue*, West Lafayette, IN, 1992.

[20] L. Zhang and J. F. Hamilton, "Development of sealing line calculation in twin screw compressors," in *Proceedings of the 3rd International Symposium on Transport Phenomena and Dynamics of Rotary Machinery*, Honolulu, Hawaii, 1990.

[21] P. J. Singh and J. L. Bowman, "Effect of design parameters on oil flooded screw compressor performance," in *Proceedings of the 1986 International Compressor Engineering Conference at Purdue*, West Lafayette, IN, 1986.

[22] W. Soedel, Introduction to the computer simulation of positive displacement compressors, West Lafayette, IN: Short Course Text at Herrick Laboratories, Purdue University, July 1972.

[23] J. F. Hamilton, Extensions of mathematical modeling of positive displacement type

compressors, West Lafayette: Short Course Text at Herrick Laboratories, Purdue University, July 1974.

[24] M. Fijiwara, H. Mori and T. Suwama, "Prediction of the oil-free screw compressors performance using digital computer," in *Proceedings of 1974 International Compressor Engineering Conference at Purdue*, West Lafayette, IN, 1974.

[25] M. Fijuwara, K. Katsuhidi, T. Matsunaga and M. Watanabe, "Computer modeling for performance analysis of rotary screw compressor," in *Proceedings of 1984 International Compressor Engineering Conference at Purdue*, West Lafayette, IN, 1984.

[26] M. A. Firnhaber and D. S. Szarkowicz, "Modeling and simulation of rotary screw compressors," in *Proceedings of 1980 International Compressor Engineering Conference*, West Lafayette, IN, 1980.

[27] J. Brablik, "Analytical model of an oil-free screw compressor," in *Proceeding of 1982 International Compressor Engineering Conference at Purdue*, West Lafayette, IN, 1982.

[28] B. Sangfors, "Analytical modeling of helical screw machine for analysis and performance prediction," in *Proceedings of 1982 International Compressor Engineering Conference at Purdue*, West Lafayette, IN, 1982.

[29] B. Sangfors, "Computer simulation of the oil injected twin screw compressor," in *Proceedings of 1984 International Compressor Engineering Conference at Purdue*, West Lafayette, IN, 1984.

[30] D. B. Dooner and A. A. Seireg, The Kinematic Geometry of Gearing, John Wiley &

Sons Ltd., 1995, pp. 56-63.

[31] F. L. Litvin, Theory of Gearing, Washington DC: NASA Publication, 1989.

[32] H. Iyoi and S. Ishimura, "x-Theory in Gear Geometry," *Transaction of ASME: Journal of Mechanical Design,* vol. 105, no. 3, pp. 286-290, 1983.

[33] R. Iyoi, M. Oka and T. Iyoi, "Determination of an Improved Gear Surface of Helical Gears for Pumping Action," *Mechanism and Machine Theory,* vol. 12, pp. 193-194, 1977.

[34] S. Togashi and H. Iyoi, "The Synthesis of Tooth Profile Shapes and Helical Gears of High Hydraulic Performance for Rotary Type Pumps," *Mechanism and Machine Theory,* vol. 8, pp. 105-123, 1973.

[35] T. Costopoulos, A. Kanarachos and E. Pantazis, "Reduction of Delivery Fluctuation and Optimum Tooth Profile of Spur Gear Rotary Pumps," *Mechanism and Machine Theory,* vol. 23, no. 2, pp. 141-146, 1988.

[36] K. Mitome and K. Seki, "A New Continuous Contact Low-Noise Gear Pump," *Trans. ASME Journal of Mechanisms, and Transmissions, and Automation in Design,* vol. 105, pp. 736-741, 1983.

[37] D. C. H. Yang, S. H. Tong and J. Lin, "Deviation-Function Based Pitch Curve Modification for Conjugate Pair Design," *Transactions of ASME - Journal of Mechanical Design,* vol. 121, no. 4, pp. 579-586, 1999.

[38] Z. Xing, H. Wu and P. Shu, "The Design of a New Generation of Twin-Screw Refrigeration Compressors," *16th International Compressor Engineering Conference Purdue,* pp. C21-5, C21-5 2002.

[39] N. Stosic and K. Hanjalic, "Development and Optimization of Screw Engine Rotor Pairs on the Basis of Computer Modelling," in *Proceedings of the 1994 International Compressor Engineering Conference at Purdue*, West Lafayette, IN, 1994.

[40] N. Stosic, I. K. Smith, A. Kovacevic and C. A. Aldis, "The Design of a Twin Screw Compressor Based on a New Rotor Profile," *Journal of Engineering Design,* vol. 8, no. 4, pp. 389-399, 1997.

[41] K. Venu Madhav, N. Stosic, I. K. Smith and A. Kovacevic, "The Design of a family of Screw Compressors for Oil Flooded Operation," in *International Conference Compressors and Their Systems*, London, 2001.

[42] N. Stosic, I. K. Smith and A. Kovacevic, "Optimization of Screw Compressors,," *Applied Thermal Engineering,* vol. 23, pp. 1177-1195, 2003.

[43] J. Sauls, "Development of a Comprehensive Thermodynamic Modelling System for Refrigerant Screw Compressors," in *Proceedings of the 1996 International Compressor Engineering Conference at Purdue*, West Lafayette, IN, 1996.

[44] K. M. Ignatiev, Y. Tang and J. S. Fleming, "Thermal Interaction in a Refrigeration Twin Screw Compressor during Compression Process," in *Proceedings of 1994 International Compressor Engineering Conference at Purdue*, West Lafayette, IN, 1994.

[45] K. Hanjalic and N. Stosic, "Development and Optimization of Screw Machines With a Simulation Model-Part II: Thermodynamic Performance Simulation and Design Optimization," *ASME Transactions: Journal of Fluids Engineering,* vol. 119, no. 3, pp. 664-670, 1997.

[46] N. Stosic, I. K. Smith and A. Kovacevic, "Numerical Simulation of Fluid Flow and Solid Structure in Screw Compressors," in *ASME International Mechanical Engineering Congress*, New Orleans, 2002.

[47] N. Stosic, I. K. Smith and S. Zagorac, "C.F.D. Studies of Flow in Screw and Scroll Compressor," in *Proceedings of 1996 International Compressor Engineering Conference at Purdue*, West Lafayette, IN, 1996.

[48] I. I. Artobolevsky, Mechanism in Modern Engineering Design, Moscow: Mir Publishers, 1977, pp. 21-31.

[49] P. J. Singh and J. L. Bowman, "Calculation of blow-hole area for screw compressors," in *Proceedings of 1990 International Compressor Engineering Conference at Purdue*, West Lafayette, IN, 1990.

[50] C. X. You, *A theoretical study of rotor forces and torques in helical twin screw compressors,* Glagow: Thesis, University of Strathclyde, 1994.

[51] S.-H. Tong, New Conjugate Pair Design - Theory and Application, Los Angeles: University of California, Los Angeles, 1998.

[52] S.-H. Tong and D. C. Yang, "On the generation of new lobe pumps for higher pumping flowrate," *Mechanism and Machine Theory,* vol. 35, pp. 997-1012, 2009.

[53] D. C. Yang and S.-H. Tong, "The specific flowrate of deviation function based lobe pumps - derivation and analysis," *Mechanism and Machine Theory,* vol. 37, pp. 1025-1042, 2002.

[54] H.-C. Liu, S.-H. Tong and D. C. Yang, "Trapping-free rotors for high-sealing lobe pumps," *Transactions of ASME - Journal of Mechanical Design,* vol. 122, pp. 536-

542, 2000.

[55] J. Yan, On the Design of Deviation-Function Based Gerotors - Theory and Algorithm, Los Angeles: University of California, Los Angeles, 2007.

[56] J. Yan, D. C. Yang and S.-H. Tong, "On the generation of analytical non-circular multilob e internal pitch curves," *Transaction of ASME - Journal of Mechanical Design,* vol. 130, p. 092601–1 –092601–8, 2008.

[57] J. Yan, D. C. Yang and S.-H. Tong, "A new gerotor design method with switch angle assignability," *Transaction of ASME - Journal of Mechanical Design,* vol. 131, pp. 011006-1 – 011006-8, 2008.

[58] S.-H. Tong, J. Yan and D. C. Yang, "Design of deviation-function based gerotors," *Mechanism and Machine Theory,* vol. 44, p. 1595 – 1606, 2009.

[59] J. L. Bowman, "Rotary, positive-displacement machine, of the helical-rotor type, and rotors therefor". US Patent No. 4,508,496, Patented 1985.

[60] S. Edstrom, "Rotor profiles for helical screw rotor machines". US Patent No. 3,787,154, Patented 1974.

[61] P. J. Edvard, "Screw rotor machines and profiles". US Patent No. 3,414,189, Patented 1968.

[62] I. A. Sakun, Vintovie kompresorii (Screw Compressors), Mashinostroenie Leningrad 41, 1960.

[63] P. E. Amosov and a. et, Vintovie kompresornie mashinii – Spravochnik(Screw Compression Mach ines-Handb o ok), Mashinstroienie, Leningrad, 1977.

[64] L. Rinder, Schraubenverdichter (Screw Compressors), New York: Springer Verlag,

1979.

[65] K. H. Konka, Schraub enkompressoren (ScrewCompressors), Duesseldorf: VDI-Verlag, 1988.

[66] P. A. O'Neill, Industrial Compressors, Theory and Equipment, Oxford: Butterworth-Heinemann, 1993.

[67] I. M. Arbon, The D esign and A pplication of Rotary Twin-shaft Compressors in the Oil and Gas Pro cess Industry, London: MEP, 1994.

[68] Z. Xing, Screw Compressors: Theory, Design and Application (in Chinese), Beijing, China: China Machine Press, 2000.

[69] K. Bammert, "Intermeshing screw rotor machine with specific thread profile". US Patent No. 4,350,480, Patented 1982.

[70] H. Kameya, S. Nozawa, M. Urashin, T. Hida and M. Aoki, "Screw fluid machine". US Patent No. 6,257,855, Patented 2001.

[71] H. T. Lee, "Screw-Rotor Machine with an Ellipse as a Part of its Male Rotor". US Patent No. 4,890,992, Patented 1990.

[72] J. L. Bowman, "Helical screw rotor profiles". US Patent No. 4,412,796, Patented 1983.

[73] S. S. Rao, Engineering Optimization– Theory and Practice, USA: John Wiley & Sons, Inc., 1996.

[74] J. W. Gardner, "Variable Lead Compressor". US Patent No 3,424,373, Patented 1969.

[75] Y. Tang, Computer Aided Design of Twin Screw Compressors, Glasgow: University

of Strathclyde, 1995.

[76] D. Xiao, Z. Xiong, Y. Yu and J. Hamilton, "The computer simulation of oil-flooded refrigeration twin-screw compressors," in *Proceedings of the 1986 International Compressor Engineering Conference at Purdue*, West Lafayette, Indiana, 1986.

[77] S. Yoshimura, "Screw Rotor Assembly for Screw Compressor". US Patent No. 4,890,991, Patented 1990.

[78] S. Yoshimura.Patent US Patent 4890991, 1990.

[79] L. Rinder.US Patent No. 4,643,654, Patented 1987.

[80] W. Lee, R. Ma, S. Chen, W. Wu and H. Hsia, "Numerical Simulation and Performance Analysis of Twin Screw Air Compressors," *International Journal of Rotating Machinery,* vol. 7, no. 1, pp. 65-78, 2001.